COMPOSITE STRUCTURES

EDITOR: I.H. MARSHALL

Special Issue
International Workshop on Experimental Techniques in the Analysis of Composite Structures

19990324 042

ELSEVIER

AQ F99-04-1205

COMPOSITE STRUCTURES

The past few decades have seen outstanding advances in the use of composite materials in structural applications. There can be little doubt that, within engineering circles, composites have revolutionised traditional design concepts and made possible an unparalleled range of new exciting possibilities as viable materials of construction. *Composite Structures*, an International Journal, disseminates knowledge between users, manufacturers, designers and researchers involved in structures or structural components manufactured using composite materials.

The journal publishes papers which contribute to knowledge in the use of composite materials in engineering structures. Papers may be on design, research and development studies, experimental investigations, theoretical analyses and fabrication techniques relevant to the application of composites in load-bearing components for assemblies. These could range from individual components such as plates and shells to complete composite structures.

REPORT DOCUMENTATION PAGE

Form Approved OMB No. 0704-0188

1. AGENCY USE ONLY (Leave blank)	2. REPORT DATE 30 January 1999	3. REPORT TYPE AND DATES COVERED Conference Proceedings

4. TITLE AND SUBTITLE

Internat'l Workshop on Experimental Techniques for Composite Structures

5. FUNDING NUMBERS

F6170897W0029

6. AUTHOR(S)

Conference Committee

7. PERFORMING ORGANIZATION NAME(S) AND ADDRESS(ES)

University of Paisley
High Street
Paisley, Renfrewshire PA1 2BE
Paisley PA1 2BE
United Kingdom

8. PERFORMING ORGANIZATION REPORT NUMBER

N/A

9. SPONSORING/MONITORING AGENCY NAME(S) AND ADDRESS(ES)

EOARD
PSC 802 BOX 14
FPO 09499-0200

10. SPONSORING/MONITORING AGENCY REPORT NUMBER

CSP 97-1005

11. SUPPLEMENTARY NOTES

12a. DISTRIBUTION/AVAILABILITY STATEMENT

Approved for public release; distribution is unlimited.

12b. DISTRIBUTION CODE

A

13. ABSTRACT (Maximum 200 words)

The Final Proceedings for Internat'l Workshop on Experimental Techniques for Composite Structures, 11 September 1997 - 11 September 1997

Analysis techniques for composite structures and structural materials.

14. SUBJECT TERMS

EOARD, Materials, Structural Materials

15. NUMBER OF PAGES

81

16. PRICE CODE

N/A

17. SECURITY CLASSIFICATION OF REPORT UNCLASSIFIED	18. SECURITY CLASSIFICATION OF THIS PAGE UNCLASSIFIED	19. SECURITY CLASSIFICATION OF ABSTRACT UNCLASSIFIED	20. LIMITATION OF ABSTRACT UL

NSN 7540-01-280-5500

Standard Form 298 (Rev. 2-89)
Prescribed by ANSI Std. 239-18
298-102

DTIC QUALITY INSPECTED 4

Foreword

These proceedings are a record of the International Workshop on Experimental Techniques in the Analysis of Composite Structures held at the University of Paisley, Scotland in September 1997. This workshop was jointly sponsored by the University of Paisley and the US Air Force European Office of Aerospace Research & Development (EOARD).

The development of future military and civilian aerospace systems depends on new breakthroughs in advanced materials. Composite structures have become indispensable to aerospace designers who continually seek lighter weight, better heat resistance and lower cost alternatives to conventional materials. EOARD is proud to sponsor cutting-edge workshops such as this one that directly contribute to fundamental understanding of this vital material.

Composite structures research has greatly benefited from recent advances in computer modeling techniques. However, no matter how good the computer simulation, it can never fully substitute for more traditional experimental techniques. The topics presented in this workshop span a wide range of research centered on perfecting experimental methods to validate computer models and better understand critical performance properties. These results advance our understanding of composite behavior and directly benefit the entire materials community.

Many thanks to all the participants who helped make this workshop a success. Special thanks to Dr Ian Marshall who deserves the credit for putting together a very useful and productive workshop

Major Jerry Jon Sellers
Chief, Aeronautics
US Air Force European Office of
Aerospace Research & Development

Moiré interferometry as a detailed validator for computational modelling of composites

J. McKelvie*, K. E. Perry

Department of Mechanical Engineering, University of Strathclyde, 16 Richmond Street, Glasgow G1 1XG, UK

Abstract

The computational modelling of multi-layered multidirectional composite materials presents particular difficulties, and therefore an experimental tool is required that is able to validate any proposed models at a level of detail appropriate to the complexity of the laminate. Such a tool requires, of course, that it in its turn be duly validated. This paper proposes the measurement of energy release rate for a delamination intersecting the edge as a suitably demanding and relevant criterion and the method of moiré interferometry as the experimental tool. The validation of the method is carried out against standard geometries and protocols. © 1998 Published by Elsevier Science Ltd. All rights reserved.

1. Introduction

The complexity of multi-layered multidirectional composite structures makes full-volume 3-D computational analysis a comparatively expensive business. Moreover, there are particular problems in the application of finite element methods to multi-layered solids, — especially at the edges and in the presence of thermal effects, — when FEA results may not satisfy equilibrium and the interlaminar stresses are therefore wrongly predicted, — see for example Ref. [1]. This difficulty is all the more disconcerting in view of the fact that mechanisms that originate from interlaminar stresses at free edges (e.g. delamination around holes) are common causes of structural degradation.

In consequence, there is continuing development of computational methods for application to this class of problem, and of course, it is essential that such methods be properly validated. It is however something of a problem in itself as to how to devise experimental procedures to accomplish the validation, and this paper describes the development of the moiré interferometry technique to that end.

2. Delamination

Because the occurrence and growth of delamination between plies in a multi-layered composite is of such

significance in structural integrity, it has been the subject of much study — for example Refs [2–6]. In brief, if one knows from experiment the critical energy release rate G_c that will cause the extension of a debond between any two adjacent layers, and if one has an analysis tool that can accurately predict G, then one has a tool that can describe safe and unsafe loading conditions — at least with respect to delamination extension. (In general, G_c will consist of components from G_{IC}, G_{IIC} and G_{IIIC} although any G_{III} effect is generally recognized to be of little significance in comparison to the other two.) Similarly, if the da/dN vs ΔG fatigue characteristics are known from experiment, then one would be able to describe the rate of delamination growth in fatigue.

An acceptable analysis tool, therefore, should be capable of good prediction of G_I and G_{II} on the edge of a multi-directional composite. This is a demanding specification, and forms the reasoning behind development of the experimental validation processes that will now be described.

3. Moiré interferometry

The technique now known as moiré interferometry dates essentially from 1978 [7]. Since then, it has become a widely adopted technique for measuring displacement and strain. A very fine text on the method is Ref. [8]. Essentially, a crossed diffraction grating is formed in, or is bonded to, the surface, and

*Corresponding author. Tel.: 44-141-548-2643; Fax: +44-141-552-5105; E-mail: JMcKelvie@mecheng.strath.ac.uk
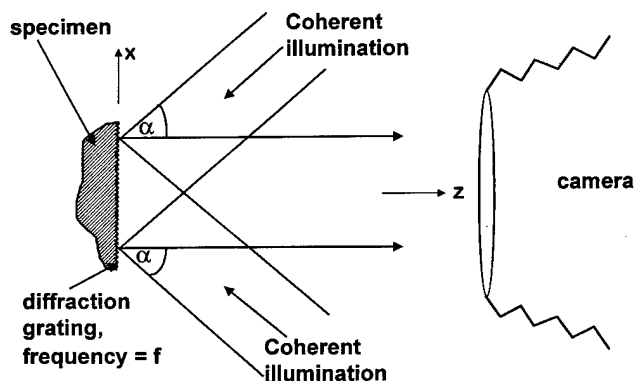
Fig. 1. General optical arrangement for moiré interferometry.

is interrogated by two coherent and beams of light symmetrically disposed, and arranged to be incident in different planes, by turns, according to the directions of interest. Figure 1 illustrates the arrangement for interrogation in the x-direction, which yields the u-displacement field. (It is also possible to use multiple beams to interrogate different directions simultaneously).

The features that have made moiré interferometry attractive are that it combines a good sensitivity (typically 0.2 micron in-plane displacement from black to white) with a very 'clean' fringe pattern. The latter property arises from the fact that the beams producing the interference fringes are derived from regular gratings, and thus are specular in nature (as opposed to the diffuse diffraction that occurs from random surfaces) so that the level of coherent speckle can be very low.

The importance of the freedom from speckle is that it permits investigation in a level of detail that is not possible with other techniques that use visible optics. (For example the fringes can be very close together — 50 fringes/mm is not difficult to achieve). Post and Han [8] have developed a technique employing fringe-shifting with which they have composed a fringe pattern in which the displacement interval is 8.5 nm black-to-white, with fringes only 2 or 3 microns apart.

4. Measuring G

The measurement of the J-integral using moiré interferometry in homogeneous material was described originally in Ref. [9], and has subsequently been applied by a number of workers. Under linear elastic constitutive conditions, J and G are identical, and this forms the basis of the procedure to be described, namely the measurement of G is to be done by evaluating the J-integral in a contour around the tip of the delamination on a free edge of the specimen.

In the case of interest here, which is a multi-directional composite, the material is non-homogeneous and non-isotropic. For the purpose of the validation procedure the following approximations are made: the material consists of a number of layers each of which is homogeneous, orthotropic, and elastic in the two principal directions. These approximations are in common use for analytical purposes with such materials.

The formulation of J for a generally non-homogeneous material is not available. However, a formulation is available [10] for a crack lying on the interface between two different materials. Using the notation of Fig. 2, J is given by

$$J = \oint_\Gamma \left(W n_x - T_x \frac{\partial u}{\partial x} - T_y \frac{\partial v}{\partial x} \right) ds$$

where W is the strain energy density, n_x is the x-component of the local unit normal to the contour Γ, and T_x and T_y are the components of the outward Traction Vector normal to the contour, and u and v are the x- and y-components respectively of the local displacement vector

There are two important considerations: firstly, the measuring process must be able to provide all of the data required to compute J, including the rather unusual $\partial v/\partial x$ term — i.e. the horizontal rate of change of the vertical displacement, — and secondly, the measurement must be capable of being done for a contour that is contained within one layer on either
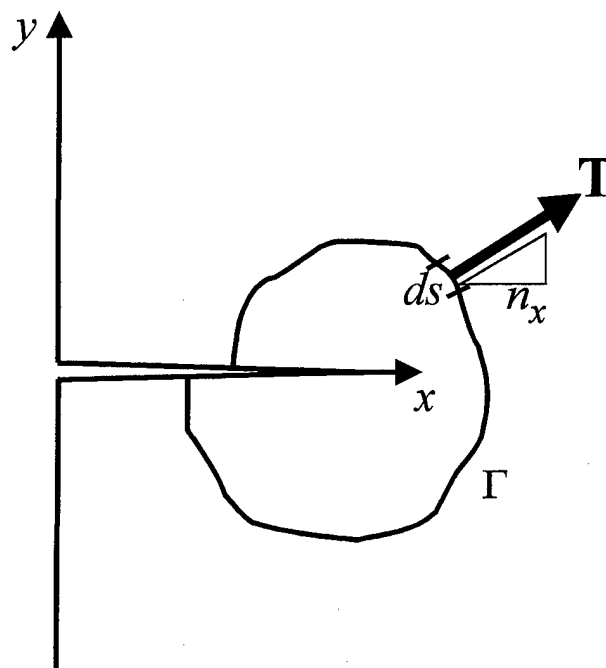
Fig. 2. Definitions for the J-integral.
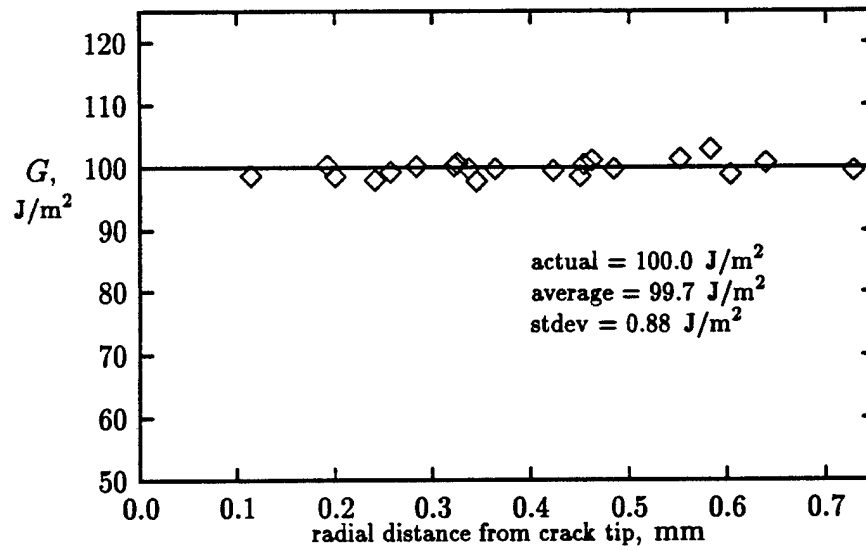
Fig. 3. J values for contours of different radii for 'ideal' data (with added noise).
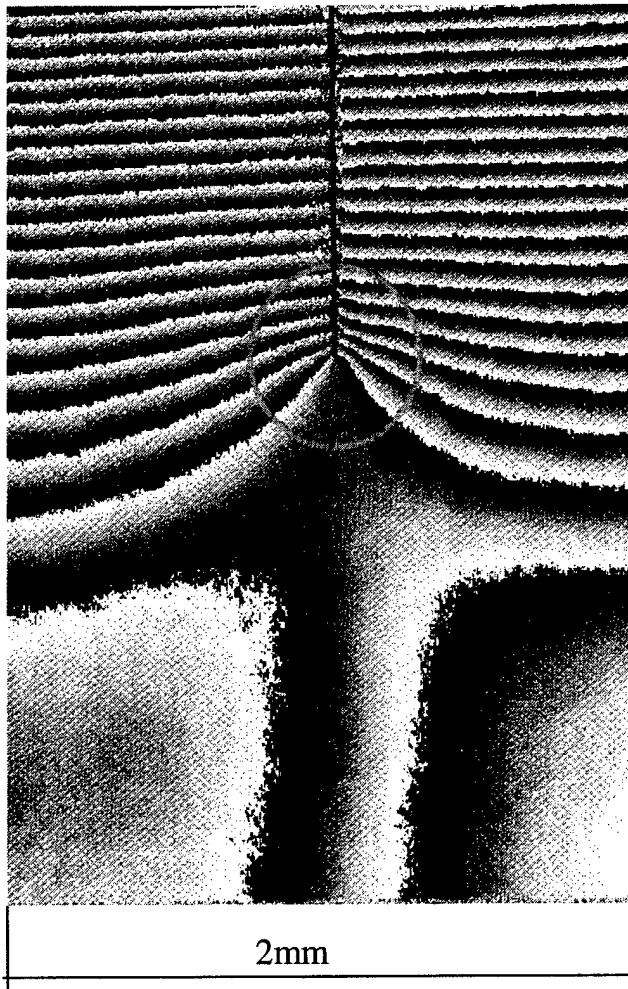
Fig. 4. Typical wrapped *v*-field interferogram for a DCB experiment.
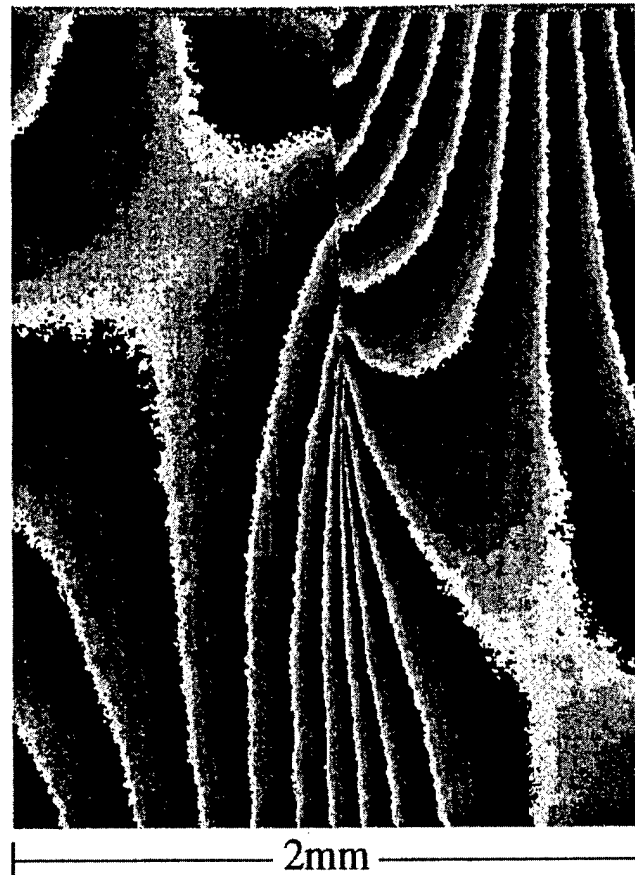
Fig. 5. Typical wrapped *u*-field interferogram for an ENF experiment.
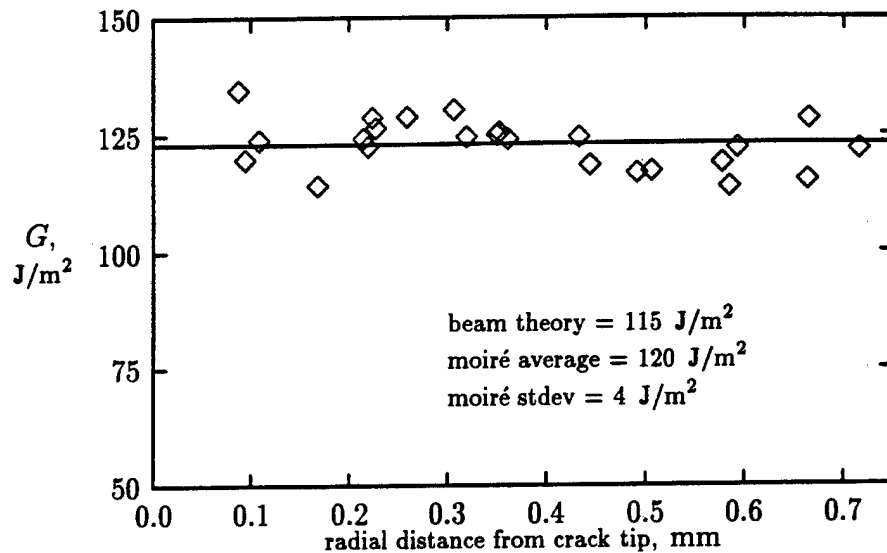
Fig. 6. J values for contours of different radii for a typical DCB specimen.

side of the crack, so that we are dealing with, at most, two different materials.

It has been the purpose of the work reported here to demonstrate that moiré interferometry is capable of making such measurements within this constraint.

5. Phase-shifting moiré interferometry

Because of the demanding nature of the task, in terms of the detail required, the use of a simple relationship such as '0.2 microns displacement from black to white' was inadequate. Interpolation of the fringe pattern was necessary. The particular embodiment of moiré interferometry that was used involved

the use of 'phase-shifting' [11] in which the fringes are made to move in a controlled systematic manner in a number of steps, (phase shift known between each step), and the resulting fringe patterns are recorded using a CCD array camera.

Since the pattern is formed by two-beam interference, one can in general describe the intensity by

$$I(x,y) = a(x,y) + b(x,y)\cos[\phi(x,y) + \delta] \qquad (1)$$

where $a(x,y)$ represents a mean light level that may be locally variable, $b(x,y)$ represents the strength of modulation of the intensity, (the peak-to-peak variation), $\phi(x,y)$ is proportional to the distribution of the particular displacement component concerned and δ is an initial indeterminate phase single.
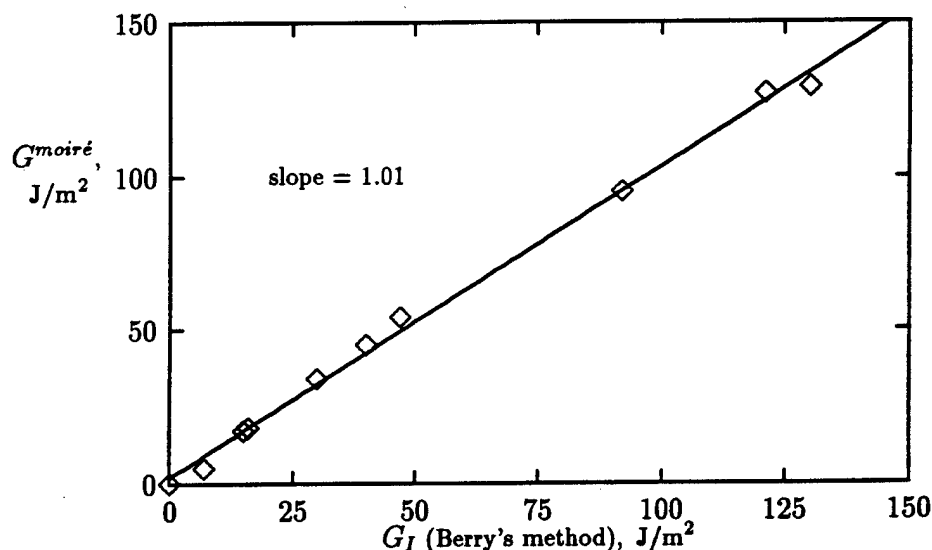
Fig. 7. Correlation of $G^{\text{moiré}}$ with global values for the DCB validation experiment.
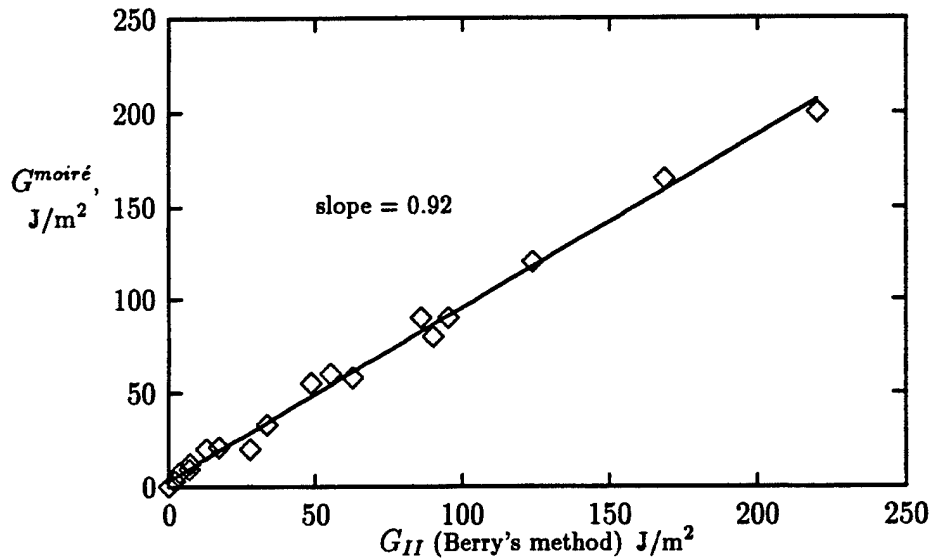
Fig. 8. Correlation of $G^{moiré}$ with global values for the ENF validation experiment.

If now, δ is deliberately altered by known amounts i times then we have, at the jth pixel,

$$I_{ij} = a_j + b_j\cos[\phi_j + \delta_i]$$ (2)

which contains four unknowns — a,b,ϕ and the initial δ. Therefore four different images will allow us to determine the value of ϕ — and therefore the displacement — at every pixel. In practice it is convenient to use $\pi/2$ phase-steps, when the four resulting images can be shown to yield the relatively simple equation for ϕ_j

$$\phi_j = \tan^{-1}\left[\frac{I_{3j} - I_{1j}}{I_{0j} - I_{2j}}\right]$$ (3)

Since $\phi = 2\pi f$ (u_x or u_y), the whole displacement field is known on a pixel-by-pixel basis and one can therefore in principle measure strain on any gauge-length down to the limit of resolution of the imaging/camera system. (Of course, eqn (3) yields values of ϕ only between π and $-\pi$, and a process known as 'unwrapping' has to be performed on the values thus obtained, adding or subtracting 2π where appropriate to yield the proper continuous function).

In practice, despite the good noise rejection of the phase-stepping process, there is some remnant disturbance (e.g. due to quantization error on the intensity, which is recorded to only 8 bits) and so a gauge-length of several pixels is more realistic. Further noise-rejection systems were developed to optimize the process;
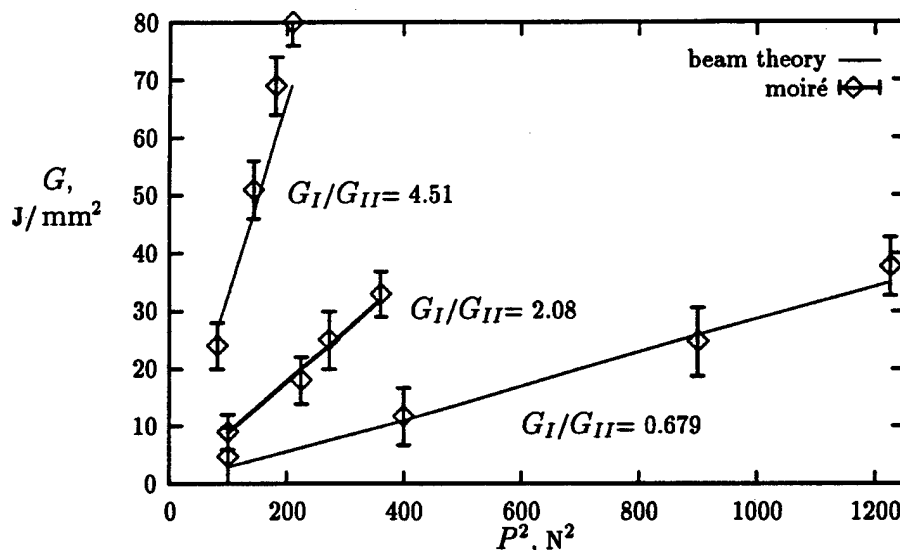
Fig. 9. $G^{moiré}$ vs P^2 for the MMB validation experiment.

details are contained in [12] and [13]. Typically in the work reported here, the field of view was 2 mm or less, so that a pixel dimension corresponded to 4 microns or smaller. It is the availability of data in this level of detail that enables the computation of the J-integral on contours that remain within one layer on either side of the delamination — that is, approximately ± 120 microns.

6. Computation of J

If we have the fields of the displacement components in the x and y directions — the u and v displacements — and the elastic constants, then we can calculate J, since

$$\varepsilon_x = \frac{\partial u}{\partial x}, \ \varepsilon_y = \frac{\partial v}{\partial y} \ \text{and} \ \gamma_{xy} = \frac{\partial u}{\partial y} + \frac{\partial v}{\partial x}$$

From the strains the stresses follow, for linear elastic material, and thus the energy and tractions can be calculated. With this data, together with the values of $\partial u/\partial x$ and $\partial v/\partial x$, the integral may be computed on a small-step basis around any convenient contour, — typically rectangular, or circular, for convenience. The method is incorporated in software that takes in eight images (four for each for x and y), the elastic constants, and a contour (either circular or rectangular, as defined by the operator). From these it outputs a value of J. Particular refinements are built into the calculations, such as ensuring that the appropriate free surface stresses are put to zero; details are given in Ref. [13].

The computation is very rapid and, to minimize noise effects, a number of closely packed contours can be used, and the results averaged.

7. Validation of the G-calculation

7.1. By simulation

The process was checked by creating artificial fringe patterns (including appropriate phase-shifted cases) for the known stress-field around a centre-crack in an orthotropic plate. Artificial noise was added and the routine was applied for this 'ideal' data for a variety of contours. The results are shown in Fig. 3 which illustrates the path-independence of the integral.

7.2. By experiment

In order to validate the whole G-measuring process experimentally, use was made of the standard delamination toughness testing procedures [14].

Specimens of standard geometry for DCB determination of G_{IC}, and for ENF determination of G_{IIC}, were manufactured in unidirectional CFRP (Ciba-Gegy T300/914C). Crossed diffraction grating was applied along the edge in the normal manner for moiré interferometry, by 'casting' the profile into a thin layer of epoxy using silicone rubber moulds. The grating frequency was 1200 lines/mm, and one grating direction coincided with the fibre direction. A thin layer of aluminium was applied by vacuum evaporation to give good reflectivity. Figures 4 and 5 show typical phase-maps for the two specimen geometries as obtained by moiré interferometry.

Experimental values for sub-critical G can be calculated for various loads using Berry's (experimental compliance) method for DCB and the analogous process for ENF. They require that the crack be grown, so that the compliance as a function of crack length may be determined. G-values determined in this way were compared with the values obtained from moiré interferograms taken simultaneously at the same load, and the results are shown in Figs 6–8. Figures 7 and 8 show that the moiré procedure and the standard agree within about $\pm 1/2\%$ for G_I and $\pm 4\%$ for G_{II}. In the current context, the importance of Fig. 6 cannot be overstated. It shows that valid measurement can be made within the required 120 micron restriction on either side of the delamination.

8. Mixed-mode work

A similar set of experiments were done for mixed-mode cases using the Reeder and Crews rig modified as recommended [15]. The comparison between moiré and the beam-theory results are shown in Fig. 9. (With MMB, a beam theory derivation of G is used, because of the complexities involved in compliance testing.)

The plot as the linear variation with P^2 is a convenience to show the comparison for all mixity ratios together. Good agreement is seen again, with the exception of the high G_I case. (The reason for that disparity is being investigated; it may lie in the rig geometry or the beam theory analysis).

9. Modelling validation proposal

In order to validate a computational model, it is simply proposed that specimens be constructed of any appropriate lay-up, but including an edge-piercing delamination. An experimental loading is then applied, arranged so as to tend to cause the delamination to extend at the edge. Values of G ($G_I + G_{II}$) can be predicted by the model and compared to the values obtained by the (now validated) moiré procedure.

10. Conclusion

A moiré procedure for measuring G for any edge-piercing delamination has been developed and validated against recognized standard tests for simple fracture modes. Calibration against the commonly used MMB test also shows generally good agreement except for the case of high G_I. The reason for that disparity is suspected to be in the geometry or analysis of the MMB rig. With that reservation, the moiré procedure represents a rigorous validation method for computational models with regard to their ability to predict free-edge energy release rates — which in turn is a highly relevant, and suitably demanding, test.

References

[1] Icardi U., Manuello A. Some considerations regarding the edge stress problem of laminates by finite elements. Computers and Structures 1991;40:581–597.

[2] Davies P., Moulin C., Kausch H.H., Fischer M. Measurement of G_{IC} and G_{IIC} in carbon epoxy composites. Compos Sci Technol 1990;38:211–227.

[3] Pavier M.J., Chester W.T. Compression failure of carbon fibre — reinforces coupons containing central delaminations. Composites 1990;21:23–31.

[4] Greenhalgh E.S. Delamination growth in carbon-fibre composite structures. Composite Structures 1993;23:165–175.

[5] Dost EF, Ilcewicz LB, Avery WB, Coxon BR. Effects of stacking sequence on impact damage resistance and residual strength of quasi-isotropic laminates. In: O'Brien TK, editor. Composite materials: fatigue and fracture, 3rd ASTM 1110, 1996:476–500.

[6] Ilcewicz LB, Dost EF, Coggeshall RL. A model for compression after impact strength evaluation. Proceedings of the 21st International SAMPE Conference, Altantic City, ch. 97 1996:130–40.

[7] McKelvie J., Walker C.A. A practical multiplied moiré system. Exp Mech 1978;18(8):316–320.

[8] Post D, Han B, Ifju P. High sensitivity moiré. Berlin: Springer Verlag, 1994.

[9] Gray T.G.F., McKelvie J., MacKenzie P.M., Walker C.A. Interferometric measurement of J for arbitrary geometry and loading. Int Jnl Frac 1984;24(R):109–114.

[10] Smelser R.E., Gurtin M.E. On the J-integral for bi-material bodies. Int Jnl Frac 1977;13(R):382–384.

[11] Creath K. Phase-measurement interferometry techniques. In: Wolf E, editor. Progress in optics. Amsterdam: Elsevier Science Publishers, 1986;XXVI:349–93.

[12] Perry K.E. Jr., McKelvie J. Reference phase-shift determination in phase-shifting moiré interferometry. Opt Las Eng 1995;22:(2):77–90.

[13] Perry KE Jr. Calculation of energy release rates for delaminations in composite materials using phase-shifting moiré interferometry. PhD thesis, University of Strathclyde, 1993.

[14] Davies P. Interlaminar fracture testing of composites. Technical report, European Group on Fracture: Polymers and Composites Task Group. Protocol for joint round robin, EGF, ASTM, JIS. April 1990.

[15] Reeder J.R., Crews J.H. Redesign of the mixed-mode bending delamination test to reduce non-linear effects. J Comp Tech Res 1992;14(1):12–19.

Variable twist torsion tests on carbon fibre composite beams

J. Loughlan*, M. Ata

Structures and Materials Technology Group, College of Aeronautics, Cranfield University, Cranfield MK43 0AL, UK

Abstract

A detailed experimental programme of work is presented which examines the constrained torsional response of carbon fibre composite beams for the cantilevered configuration with torque applied at the free end. The behaviour of open-section beams and that of single-cell closed-section box beams is reported and discussed and the experimental findings are shown to corroborate simple engineering theoretical approaches. Tests have been carried out on zed and angle-section beams and thus the effects of primary and secondary warping restraint respectively on the torsional response of open-section beams are examined. The behaviour of zed-section beams is governed, in the main, by primary effects and that of angle-section beams is associated solely with secondary effects. The stress distributions along the beams and around the cross-sections are determined from the measured strains during test obtained from surface bonded strain gauges and comparison of these with theory is shown to be in good agreement. The essential differences in response to constrained torsion between open and closed-section beams are detailed in the paper and the importance of experimental tests in the analysis of composite structures is highlighted. © 1998 Published by Elsevier Science Ltd. All rights reserved.

1. Introduction

Structural components manufactured from fibrous polymer composite materials, respond quite differently, through the very nature of their make-up, to that of metallic materials when subjected to mechanical or environmental loading. The failure mechanisms associated with composite construction are, indeed, quite different to those of similar conventional metal structures. Internal fibre or matrix failure in a ply of a composite laminate will lead to a loss of stiffness of the laminate and a redistribution of the applied loading to the intact plies. This process of events can propagate fairly rapidly, leading to successive ply failures and sudden failure of the laminate. This type of response has to be contrasted with the well understood yielding type failures associated with metallic construction.

Their are many aspects pertaining to composite materials and construction which give rise to complications in the analysis and design of such structures. Due to the anisotropic nature of typical laminated fibre polymer composites it is possible, for example, depending on lay-up configuration, to experience the effects of mechanical couplings. Subjecting a thin laminated plate with generalized lay-up configuration to in-plane loading will therefore result in a non-linear response and thus out-of-plane bending and twisting of the laminate will occur from the onset of in-plane loading. Again, this type of behaviour has to be viewed in relation to the linear response which would be experienced in the case of a thin isotropic plate.

Since composite materials behave in an anisotropic manner and, in addition, are associated with numerous unique characteristics, the need for the experimental testing of composite construction is, to say the least, of paramount importance. Such aspects as non-visible damage, moisture induced degradation, the tendency to delaminate at free edges and the very low interlaminar shear and transverse tension strengths of laminates relative to their in-plane strengths are just some of the unique characteristics which serve to complicate the analysis procedures of composite structures and to promote the need for structural testing.

It is clear from the aforementioned comments that, in comparison with the isotropic response of structures to loading, more elaborate and detailed analytical and solution procedures are necessary to account for the complexities associated with the anisotropic nature of typical composite construction. It is also clear that, due to the many unique characteristics associated with composites, particularly those pertaining to failure

*Corresponding author. Tel.: 01234 754613; E-mail: Joe.Loughlan@cranfield.ac.uk

mechanisms, the need for structural testing as an aid to the development of sound theoretical practice and to give a clear understanding of actual response, is of paramount importance.

Our present day knowledge and understanding of the mechanical response to loading of composite materials and structures is due to the vast amount of research that has been carried out over the years and published in the open literature. It is clearly evident from the literature that a large proportion of the research to date on composite structures is, as expected, of an experimental nature with consideration being given to a great many aspects. The wide spectrum of experimental work reported in the literature includes such aspects as buckling and post-buckling, elastic couplings, delamination, impact damage, smart structures, cut-outs, creep and creep rupture, moisture and thermal effects and the performance of stitched composite structures to name just some.

An indication of the breadth and quality of the research which has been undertaken is given here. Mention is made of only some of the many studies carried out and these have been chosen in order to reflect the very wide range of design aspects which have to be given consideration in the case of composite structures.

Much of the research pertaining to composite structural sections, open or closed in nature, has been associated with the effect of the various elastic stiffness couplings on structural response [1–3].

The complexities associated with composite box beam construction typical of that used in aerospace applications are addressed in the work of Bauchau et al. [1]. Their experimental work clearly indicates that warping constraint causes a drastic redistribution of the shearing strains in box beams and this is noted to be particularly true for those beams whose laminate walls are associated with in-plane shear-extension elastic coupling. The test specimens used in the experimental programme were purposely designed to enhance non-classical effects and thus standard beam theory is shown to give erroneous predictions of the torsional response of the composite beams.

Tests on graphite–epoxy thin-walled box beams have been carried out by Chandra et al. [2] whereby the use of symmetric and antisymmetric lay-up configurations for the box beams permit the examination of bending–torsion coupling and extension–torsion coupling respectively. The behaviour of composite I-beams with elastic couplings has been studied both theoretically and experimentally by Chandra and Chopra [3] and in this work it is shown that the local extension–twist coupling of the individual flange elements of the sections significantly influences the overall bending–torsion coupling of the I-beams.

Buckling studies have featured strongly in previous work pertaining to composite structures [4–7]. Having a good understanding of the many different types of buckling and of the mechanics of buckling and post-buckling behaviour is a prerequisite for one to be able to design adequate and reliable composite structures. The importance of buckling is clearly reflected in the great many technical papers published on the subject in the open literature. Snell and Greaves [4] have studied the buckling and strength characteristics of CFRP cylindrically curved stiffened panels with plain flat outstands. In this work it was found that geometrical imperfections caused a minimal scatter in the experimental compressive failure loads despite the presence of impact damage in some of the panels. The cylindrically curved composite panel with plain flat outstands has also been studied by Kim et al. [5] for the case of compressive loading. In this work the predictions from a non-linear finite element analysis are shown to compare favourably with the actual behaviour of a four bladed test panel. A progressive failure analysis is implemented in order to determine the failure characteristics and the post-buckling ultimate loads of the curved stiffened panels and thus the maximum stress failure criterion is applied to all of the finite elements of the structural model on a ply by ply basis as loading progresses. It is clear that, for such complex non-linear analysis procedures involving the down-grading of failed plies in the composite structural model, experimental testing must take place in parallel, essentially for corroboration and to inspire confidence in the final structural design.

The effect of cut-outs on the buckling response of composite construction has been given some consideration by Eiblmeier and Loughlan [6]. The influence of centrally located circular cut-outs on the buckling performance of thin carbon fibre composite panels loaded in pure shear or in compression has been studied and the effect of reinforcement rings bonded to one or both sides of the panel at the hole edge is examined in some detail. The investigation uses finite element analysis extensively and this, coupled with a fairly detailed experimental programme, is shown to provide a good understanding of the post-buckling mechanics of the ring stiffened panels.

The lateral stability of pultruded GRP I-section beams was investigated in the work of Brooks and Turvey [7]. A series of lateral buckling tests have been carried out by these researchers for the cantilever configuration with the applied point load located at the free end of the beam and at the section centroid. The lateral buckling predictions determined from their finite element eigenvalue analyses were found to be somewhat different to the critical buckling loads obtained from test and it was concluded that perhaps the inclusion of initial deformations and pre-buckling

deformations in a non-linear incremental finite element analysis would lead to closer correlation with the test results.

Laminated composite materials can be associated with various forms of damage. One type of damage is that of delamination or the disbond of two adjacent plies in the laminated stack. Delamination may be caused by impact or indeed may occur during the manufacturing process. Since delaminations are cracks between plies within the laminate thickness, visible evidence of their existence may not be present. The final outcome of the presence of delamination is a loss of strength and stiffness leading, invariably, to failure at load levels which may well be far below the un-damaged strength of the structure. A great many researchers have given consideration to the effect of delamination damage on composite structural response and some of these works [8,9] are made mention of here.

The growth of delaminations embedded in laminated carbon fibre reinforced epoxy test specimens has been investigated by Kruger *et al.* [8]. The specimens were subjected to tension–compression fatigue loading and had artificial circular delamination regions in-built during the manufacturing process. The out-of-plane buckling deformations of the delaminated region, occurring during the compression phase of loading, were measured using the moire technique and the delamination front contours thus determined. These contours were then used in conjunction with two and three dimensional finite element models to compute the post-buckling state of the test specimens. This combined experimental–numerical approach is shown to give reasonably good agreement with the measured deformations.

A fairly realistic model of damage has been considered by Cairns *et al.* [9]. In this work an investigation is made of circular delamination regions with the study involving both experimental and analytical inputs. Laminated plates were manufactured for testing in a compression after impact configuration. The plates were made with in-built delaminations caused by implanting thin teflon films. Using an assumed deformation field the Rayleigh–Ritz minimum potential energy procedure is employed to determine sublaminate behaviour. Good agreement was found to exist between the analytical model and the experimental findings. One notable observation from this work is the fact that, delamination growth is quite unstable for the smaller diameter delaminations. Initial propagation is thus shown to hasten the occurrence of large delamination growth.

In very recent years the progress and developments made in the area of smart structures technology have been formidable. Laminated composite construction lends itself readily to the concepts and ideas associated with smart structures technology. The concepts and ideas are basically quite simple in nature and yet their application involves numerous exciting possibilities which could revolutionize engineering design as we know it today. It is expected that this new emerging technology will have a significant impact on the engineering designs of the future. Mention is made here of a number of works [10–13] covering different applications.

Damage control through the use of pre-strained shape memory alloy, SMA, wires embedded in composite material has been investigated by Rogers *et al.* [10]. When activated, the recovery stress of the SMA wires is tensile in nature and thus the host composite matrix structure, which is the restraining medium, is subjected to compressive action. This phenomenon can be used for active damage control whereby significant compressive stresses can be generated at a crack tip causing a reduction in the stress intensity factor and thus reducing the propagation rate of the crack or indeed preventing growth. The experimental work of Rogers *et al.* [10] has demonstrated a 24% reduction in the stress intensity factor associated with cracks in photoelastic epoxy test specimens.

If pre-strained SMA wires are embedded off the middle surface of a symmetrically balanced laminated plate then, when the wires are activated through resistive heating, the composite plate will bend and change its shape. This is due, of course, to the eccentricity or offset of the wires from the mid-plane of the plate. Being able to change the geometrical shape of a structure through induced strain actuation, is indeed quite exciting and has numerous possible applications. The concept of using the shape memory effect to provide active adjustable camber in aerodynamic sections to influence the airflow is considered to be one approach with considerable promise. Agnes and Silva [11] give details of some of the research and development programmes pursued in the USA at the USAF Wright Laboratory from which it is clear that a high degree of importance is given to the possible applications of shape control.

Unwanted vibrations in composite construction can be removed through the use of induced strain actuation. Both the sensing and actuation control capabilities for this application are considered to be particularly well suited to the use of piezoelectric materials. The suppression of structural vibrations can be achieved through the use of piezopolymer, PVDF, sensors and piezoceramic, PZT, actuators. These can be surface bonded to the structure and appropriately located on the structure to deal with any particular mode of vibration. In vibration control, it is possible to reduce the amplitudes of the vibrations or indeed to suppress completely any particular mode of vibration. The experimental work of Roberts *et al.* [12] demon-

strates the active structural damping of a cantilevered carbon fibre composite beam using PVDF sensors and PZT actuators.

Buckling control in composite structures can be implemented through the use of induced strain actuation. The shape memory effect or the piezoelectric effect can be employed for this purpose. Buckling manifests itself by the structure losing its geometrical shape at the critical load levels. Buckling control is, in a way, similar in nature to that of shape control. In the case of smart wings, the aim is to alter the geometry of the aerodynamic cross-sections in order to improve performance. In the case of buckling control however, the aim is to maintain the original structural shape in order to avoid buckling and the adverse affects of post-buckling behaviour. In doing this, we are able to improve the load carrying capability of the structure. The overall flexural buckling control of composite column strips has been investigated both theoretically and experimentally by Thompson and Loughlan [13]. Induced strain actuation associated with the piezoelectric effect is employed in this work and this is used in conjunction with a closed loop control system. For the range of tests carried out it is shown that increases in carrying capacity of the order of 30% can be achieved when the test strips are subjected to closed loop active control.

Stitched reinforced composite materials are considered as having a high degree of structural potential and thus, in recent years, these have been looked at more closely for a variety of applications [14–16]. Acoustic emission and image analysis have been used by Caneva et al. [14] as a means of evaluating the impact damage of advanced stitched E-glass/epoxy laminates. The effect of an impact is first characterized through an image analysis technique and post-impact compressional behaviour is then monitored by acoustic emission. It is shown in this work that the cross-grid stitching mesh has an important role to play with regard to the laminate performance in general and in particular with reference to the damaged area after impact and the inter-laminar delaminating process. Indeed, it is to be noted that laminates with a fine cross-stitching mesh can be more seriously damaged by the impact process than unstitched laminates.

The residual compressive strength of stitched graphite–epoxy laminates with simulated impact damage has been the subject of study in the work of Sharma and Sankar [15] with the delaminations simulating the impact damage being created through the insertion of teflon film strips at various ply interfaces prior to stitching. The stitching in this case is not cross-grid in nature but is unidirectional and in line with the applied compressive loading direction. The simulated damage is not circular in nature but is a parallel band of damage which exists across the full width of the test specimen at right angles to the loading direction and at the specimen mid-height. The through the thickness damage at the ply interfaces is also symmetrically disposed about the laminate mid-plane. Clearly, this type of damage is not truly representative of actual damage, nevertheless, it is shown in this work that the process of unidirectional stitching is able to eliminate sublaminate buckling and to improve the residual strength of some laminates by a fairly large margin.

Yeh and Chen [16] have reported their findings from an experimental study of the behaviour of two stitched composite stiffened shear panels, these being manufactured by the resin transfer moulding process. For the analysis part of this work a finite element model was employed to determine buckling and post-buckling behaviour. The panels were of post-buckled design and failure during test was noted to be of the order of 3.5 times the initial buckling load. Of particular interest was the fact that the stiffened shear panels did not fail as a result of the stiffeners detaching themselves from the composite skin as this is generally the most typical mode of failure for a post-buckled design with co-cured or bonded stiffeners. In conclusion it was thought that the reason for this was more than likely to be the result of the stiffeners being stitched to the skin.

Many other interesting studies of the unique characteristics of composite construction are to be found in the open literature. The work of Little et al. [17] examines the tensile creep behaviour of random continuous fibre mat reinforced polypropylene composites indicating the three distinct stages of creep at elevated temperatures. Controlling thermal stresses in composites through the use of prestressed fibres is the subject of study in the work of Tuttle et al. [18] and thus it has been noted that matrix cracking could be greatly reduced in some laminates as a result. Jian et al. [19] have studied the possibility of detecting damage in composite materials using piezoelectric patches in conjunction with a vibrational response approach. The natural frequencies of glass–epoxy laminated plates containing controlled levels of damage, in the form of inter-ply delaminations, are thus shown to decrease with increase in damage level and the approach is considered to be potentially promising for non-destructive evaluation.

The foregoing discussions and comments highlight just some of the many complexities associated with composite materials and structures. Clearly, the response of composites to different loading and environmental conditions is somewhat different to that of the more conventional isotropic metallic construction. In order to keep abreast of the developments in composites and to fully understand the mechanical response of composite construction to loading, it is essential that the appropriate knowledge is made avail-

able through the publication of advanced composites research in the open literature.

In this paper the authors give details of an experimental programme of work designed to give an insight into and understanding of the constrained torsional response of open-section and single-cell closed-section carbon fibre composite beams. The beams are subjected to variable twist through the cantilever configuration with torque being applied at the free end and cross-sections are chosen to demonstrate both primary and secondary warping effects. The overall elastic couplings of the test beams are eliminated through the use of constituent laminates which are symmetrically laid-up about their own mid-planes and which possess in-plane orthotropy. The analysis procedures for such beams are, of course, of a less complex nature than those associated with beams of a more generalized lay-up configuration and thus the existing theories for isotropic construction, such as those, for example, of Von Karman and Christensen [20] and Benscoter [21], can be modified in a simple manner to account for the effects of layered composite material. This approach has been employed by Ata [22] with a considerable degree of success and more specific details of this work are reported by Loughlan and Ata [23–25]. The experimental findings from tests carried out on zed, angle and box-section beams are reported and these clearly illustrate the essential differences in response of open and closed-section beams to constrained torsion. In order to have confidence in any theoretical approaches or analysis procedures required to predict the complex mechanics of the restrained torsion of composite structural sections the need for mechanical testing is clearly evident.

2. Experimental investigation

Two composite Z beams and a composite angle-section beam have been tested in both the free and constrained torsion modes. The beams were manufactured in the composites laboratory at Cranfield University using CIBA-GEIGY Fibredux 913 high modulus carbon fibre pre-impregnated sheets with a ply thickness of 0.25 mm. Using standard testing procedures the ply material properties were determined as follows:

$E_1 = 140.3 \text{ kN/mm}^2$, $E_2 = 11 \text{ kN/mm}^2$

$G_{12} = 5.65 \text{ kN/mm}^2$, $v_{12} = 0.34$

The manufacturing process of open-section composite beams is depicted schematically in Fig. 1 with reference to the case of the Z-section. Aluminium was selected as the tooling material. The master tool is first sprayed with a mould release agent and the prepreg plies are then laid-up on to the tooling. Steel plates, which are first of all release sprayed, are then located
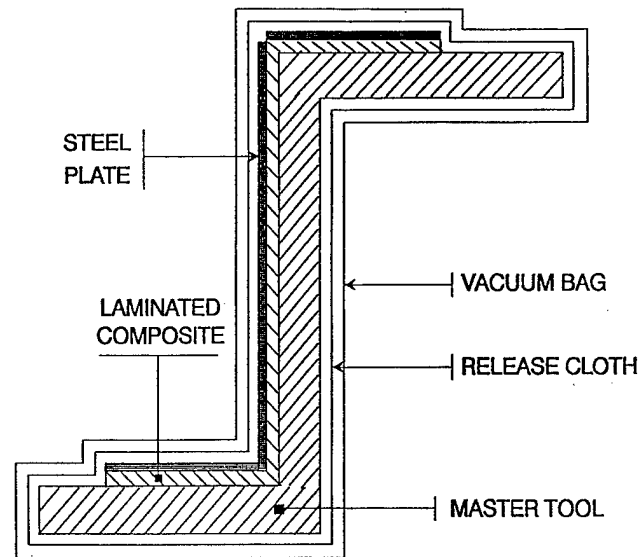
Fig. 1. The manufacturing process of open-section composite beams.

on each wall of the laid-up composite beam in order to improve the surface quality of the structural component. At this point the system is wrapped in a release cloth and this set-up is then put in a vacuum bag as indicated in Fig. 1. After applying the vacuum the complete assembly is then put in an autoclave for the curing process. It should be noted that during the laying up phase, intermediary consolidation was carried out under vacuum after every two plies laid-up. The manufacturing process described was found to yield good quality structural components with regard to both dimensional accuracy and surface finish.

The Z-beams are 525 mm long with 50 mm wide flanges and 100 mm deep webs. Two different lay-up configurations were considered for these test beams. In the first, all of the flat walls of the Z-section are 45° symmetric angle plies of the form $[(45/-45)_2]_s$ and in the second the flanges are symmetric quasi-isotropic in nature of the form $[45/-45/90/0]_s$ with the web lay-up being $[(45/-45)_2]_s$. The Z-beams therefore have a constant wall thickness of 2 mm. The angle-section test beam is 622 mm long with 50 mm wide flats of 2 mm wall thickness and a lay-up configuration of the form $[0/0/90/90]_s$. It is intended that the Z-beams will demonstrate, in the main, the effects of constrained primary warping and that the angle-section beam will indicate, solely, constrained secondary effects.

The constrained conditions at one end of the open-section beams is achieved in practice through the use of 10 mm thick steel end plates. The ends of the beams are preliminary bonded to the steel plates using super glue and making sure that the longitudinal axes of the beams are perpendicular to the steel plates. Glass fibre cloth is then built-up from the steel end plates to the beam walls by means of wet lamination and this is

done on both sides of each flat wall of the cross-section in such a way as to render the ends of the beams to be effectively built-in.

Torque is applied to the test beams using an Avery 6609 CGG Reverse Torsion Testing machine. In the case of free torsion, the test beams are mounted between the machine centres using specially designed end locating units which allow warping of the cross-section and apply the torque through the shear centre of the beams. In the case of constrained torsion, the 10 mm thick steel end plates, attached to the beams as described previously, are bolted rigidly to the rotationally fixed machine centre. Torque is then applied through the shear centre at the free end of the beams using one of the specially designed end locating units mounted on the rotationally free machine centre which is driven by a four-speed motorized gear box. In this way warping displacements are permitted and will be a maximum at the free end of the beam. They will, of course, vary at each cross-section along the beam length and will be zero at the constrained end.

Strain gauges were attached to the test beams both along their lengths and around their cross-sections. The strain gauges used were Tokyo Sokki Kenkyujo FLA-3-IL with a gauge resistance of $120 \pm 0.3\ \Omega$ and a gauge factor of 2.13. A gauge length of 3 mm was thought to be the most suitable when considering the anticipated loading range and maximum strain levels of the test specimens which were not expected to exceed three percent. The strain results were recorded in millivolts (mV) using a FLUKE 2200B data logger and these were then converted to strains by making the appropriate use of the gauge factor.

Inter-laminar stresses are normally considered to be effective within a distance of one laminate thickness from a free edge. Within this vicinity plane stress classical plate theory is not valid and measured surface strains are not easily related to subsurface lamina strains. At distances greater than one laminate thickness from a free edge the inter-laminar stresses are zero; classical plate theory is valid; and thus measured surface strains can be used to infer the subsurface lamina strains. In view of this, the limiting distance of the strain gauges attached to the test beams, relative to the flange free edges, is 2 mm.

Figures 2 and 3 show the strain gauge locations for the two Z-section test beams. The gauge number given at a particular location actually refers to a pair of gauges at that location, one attached to each surface of the laminate wall. The average of the readings from each pair of gauges thus enables the prediction of the variation in the constrained warping direct stresses σ_Γ along the length of the test beams and around their cross-sections.

With reference to Fig. 2, gauges 6 and 9 on the flanges of the test beam whose walls have the lay-up configuration of $[(45/-45)_2]_s$, are located at the position of zero warping which is 12.5 mm from the flange–web junction and thus these gauges should register a zero mid-surface strain. The force intensity distribution round this section is shown schematically in Fig. 4(a) with gauges 6 and 9 located appropriately at the zero intensity locations. For the test beam whose flat walls have different lay-up configurations the zero warping position on the flange shifts more towards the flange free edge and thus gauges 7 in Fig. 3 are located
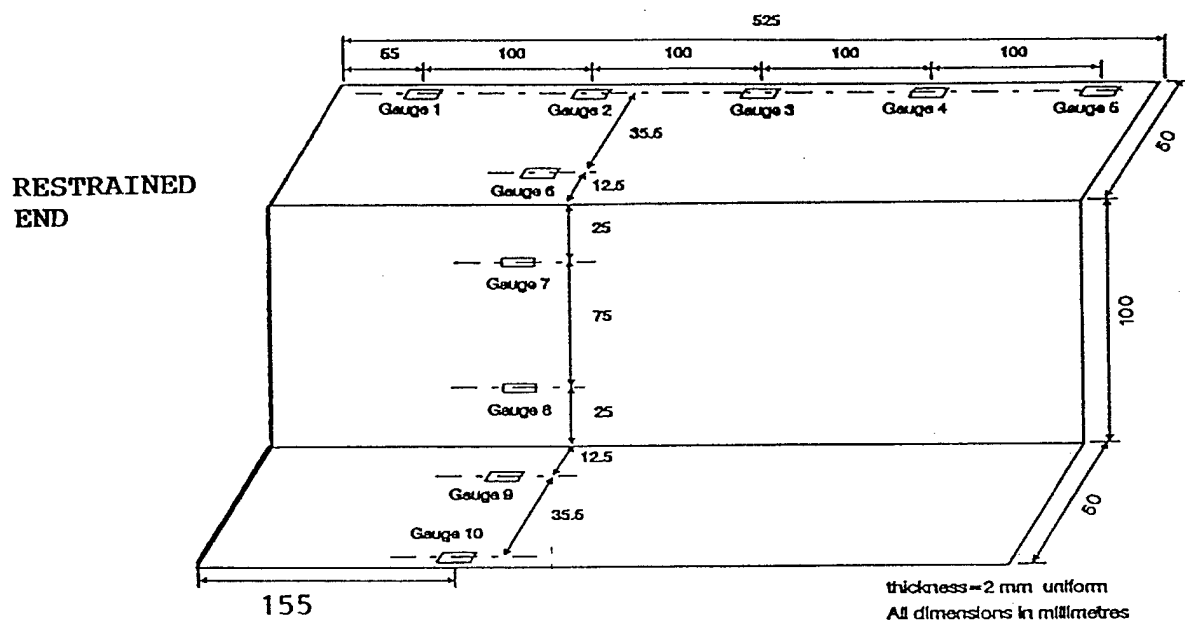
Fig. 2. Strain gauge positions on $[45/-45]_s$ test beam.
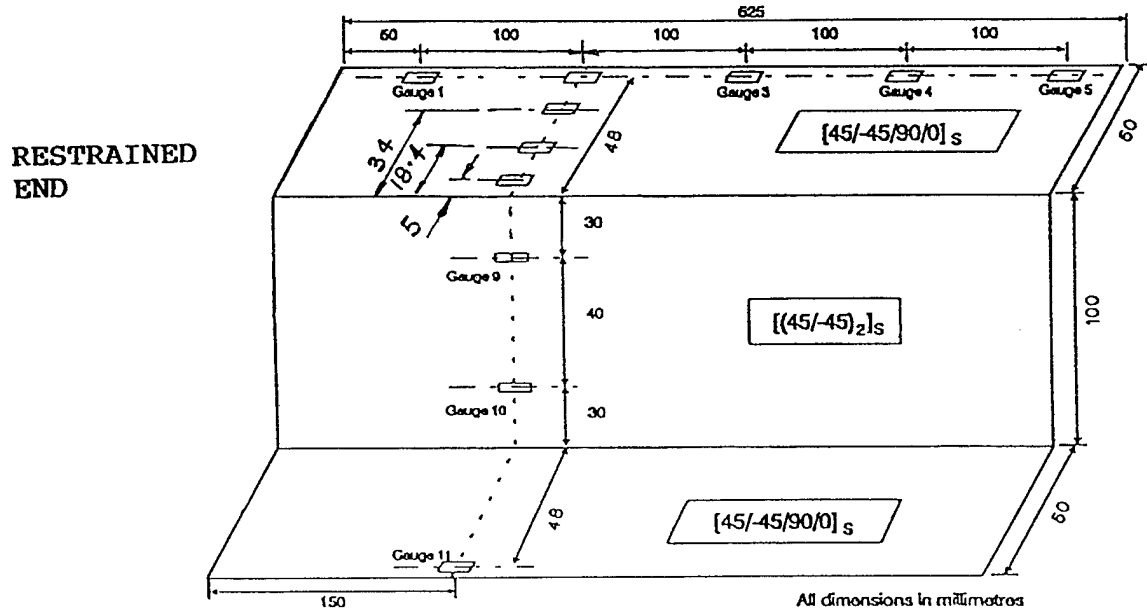
Fig. 3. Strain gauge positionson test beam with different lay-ups.

at the new position of zero warping which is now 18.4 mm from the flange–web junction and consequently these should also register a zero mid-surface strain. The force intensity distribution round this section is shown schematically in Fig. 4(b) indicating the expected step level of intensity at the flange–web junction and showing gauges 7 located appropriately at the zero intensity location on the flange.

The strain gauge locations for the cross-ply angle-section test beam are shown in Fig. 5. For this section only secondary warping is possible and thus we are specifically interested in the surface direct stress levels

along the cross-section due to warping restraint. The surface stresses will, of course, be greatest at the free edge locations of the section and thus gauges are located along the length of the beam at 2 mm from the free edge as indicated in Fig. 5. The decay in constrained warping stresses along the length of the beam in the case of angle-sections is quite severe and thus it is indicated in Fig. 5 that these are expected to be negligible within a 120 mm length from the fixed end of the beam. This is to be contrasted with the strain gauge profile for the Z-section test beams as shown in Figs 2 and 3 which clearly indicate that the
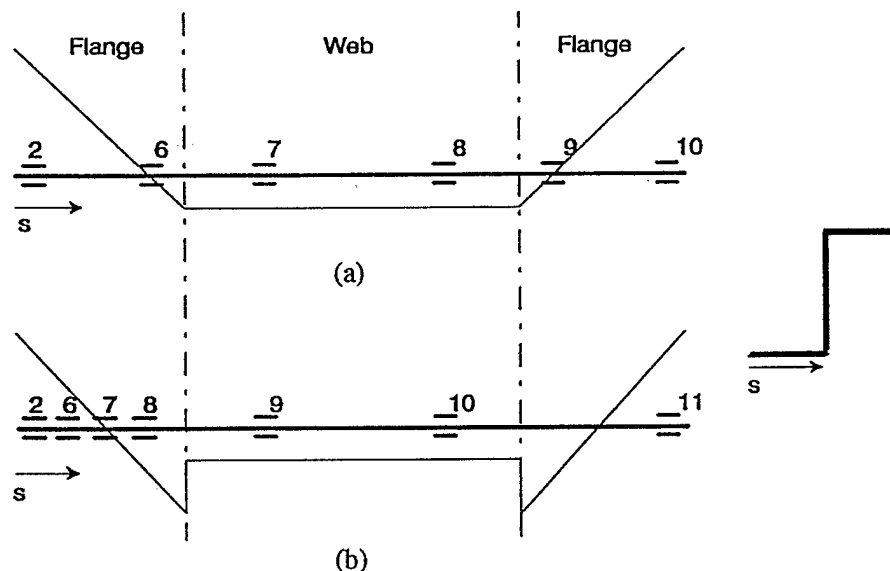
Fig. 4. Z-beam, force intensity distribution and location of strain gauges round the section. (a) Steel and $[(45/-45)_2]_s$; (b) flanges $[45/-45/90/0]_s$ web $[(45/-45)_2]_s$.
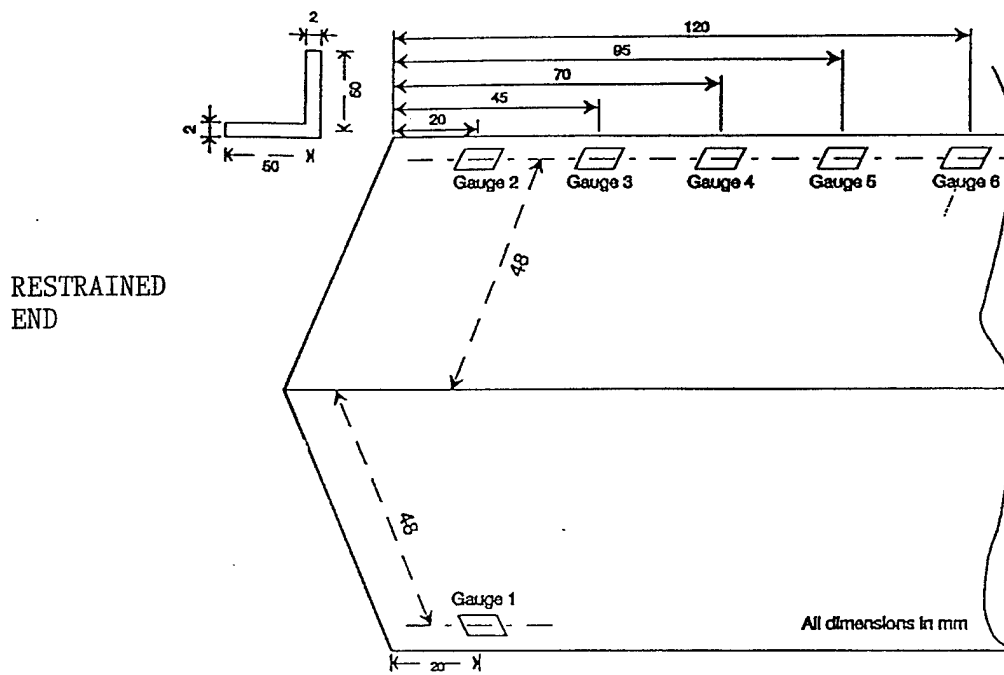
Fig. 5. Location of strain gauges on the $[0/0/90/90]_s$ test beam, L = 622 mm.

constrained membrane stresses for these beams are expected to be significant all along the beam length.

The testing procedure is essentially the same for both the free and restrained torsion cases. Torque is applied to the Z-section beams in approx. 2.25 kN-mm increments and to the angle-section beam in approx. 0.56 kN-mm increments and strain and rotation readings noted at each interval during both the loading and unloading stages. This process is repeated two more times. The applied torque is then reversed and the rotation and strain readings recorded a further three times. The average of the six cycles is then taken as the test data.

An experimental study has also been made of the constrained torsional behaviour of three specific carbon fibre composite box beams and the appropriate details are reported here. The composite box sections were manufactured from CIBA-GEIGY Fibredux 913 high modulus carbon fibre pre-impregnated ply sheets with a ply thickness of 0.125 mm and from standard tensile tests carried out in the Cranfield University structures laboratory the ply material properties were determined as follows:

$E_1 = 141.8$ kN/mm^2, $E_2 = 8.94$ kN/mm^2,

$G_{12} = 5.295$ kN/mm^2, $v_{12} = 0.36$

The beams are 530 mm long and the outside dimensions of the box cross-sections are 100 mm wide for the flanges with 50 mm deep webs. Three different lay-up configurations were considered for the composite test beams. In all configurations a total of eight plies were

utilized and thus the test beams have a constant wall thickness of 1 mm. The beams were manufactured in the composites laboratory at Cranfield University and the three lay-up configurations considered are detailed as follows:

(a) Flanges and Webs $[(45/-45)_2]_s$
(b) Flanges and Webs $[45/0/-45/90]_s$
(c) Flanges $[45/0/90/-45]_s$ and Webs $[(45/-45)_2]_s$

The basic manufacturing process for the composite beams employed the vacuum bag technique and an autoclave for curing. The physical process of laying-up the pre-impregnated ply sheets to form the box section geometry of the composite test beams was that associated with the mandrel wrapping technique. This approach is, essentially, similar in principle to that of the filament winding process used, for example, in the manufacture of composite cylinders whereby fibres are wound, under tension, onto a mandrel and in a synchronous fashion which controls fibre angle.

The prepreg ply sheets were laid-up on a male tool supported between centres on a lathe. Aluminium was selected as the tooling material and to facilitate easy withdrawal of the cured beam from the rectangular cross-section tool, this was manufactured in two halves with a 5° taper as shown in Fig. 6. The two halves of the tooling are bolted together through locating pins and in addition an end plate forms part of the tooling assembly as indicated. The end plate enables a mounting flange to be laid-up integrally with the composite box beam thus facilitating the mounting of
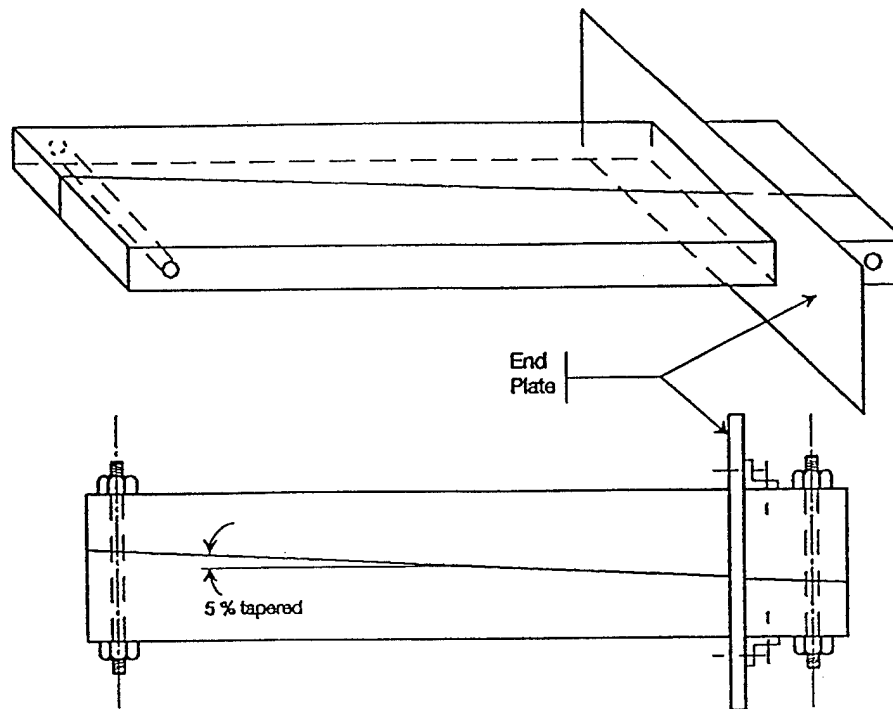
Fig. 6. Box beam tooling.

the beam in the torsion testing machine to represent the cantilever configuration with its associated axial constraint conditions at the supported end.

Before commencing manufacture of a composite beam, the tooling assembly is release sprayed and bolt heads and sharp edges taped to avoid puncturing the vacuum bag. The tooling is then rotated slowly between the lathe centres whilst simultaneously wrapping the prepreg plies, with differing ply angles, around the tooling and under hand tension. The ends of each ply wrap were taped to the tooling and vacuum consolidation was carried out after every two plies. The edge fixing tape included in the build up of the plies was then removed in the cutting-to-size process after cure completion in the autoclave.

The appropriate end constraint conditions of the composite beams were effectively achieved in practice through the use of 10 mm thick steel end plates. The composite integral mounting flange of the box beams, which is, in itself, of the order of 2 mm thick, is bonded to the steel plates using super glue with due care being taken to ensure that the longitudinal axes of the beams were perpendicular to the steel plates. In this way the steel/composite combination formed a sufficiently rigid support base to render the ends of the beams to be effectively built-in.

Figure 7 gives the general dimensions of the test box beams and indicates the surface numbers allocated to the individual walls of the sections for the purpose of clarification when discussing strain gauge location. The

outside surfaces of the upper and lower flanges of the composite box specimens are designated 1 and 3 respectively whilst 2 and 4 are associated with the outside surfaces of the right and left hand webs of the beams respectively when viewed from the free end. Strain gauges were placed along two diagonally opposite corners of the beams as shown in Figs 8 and 9 which relate to beam (c) the test beam with different lay-up configurations in its flanges and webs.

Thirty strain gauges in total were mounted on the flange and web outside surfaces of this beam and the locations of these on each wall of the section are shown in the surface development diagram of Fig. 8. The strain gauge locations around the beam cross-section at a distance of 30 mm from the restrained end are further illustrated, for clarity, in Fig. 9 and the dotted lines in this indicate the typical force intensity distribution around a box section with f and w being the maximum force intensity values in the flange and web respectively at the flange–web junction. The force intensity variation indicated in Fig. 9 is, of course, schematic. Clearly, the f and w magnitudes can be significantly different and will depend on the actual laminate lay-up configurations of the flange and web components of the composite beams.

It is of note that the strain gauges are all mounted within the first and third quadrants of the box cross-section and that for each gauge in the first quadrant there is one correspondingly positioned in the third. The strain gauge locations were chosen purposefully as
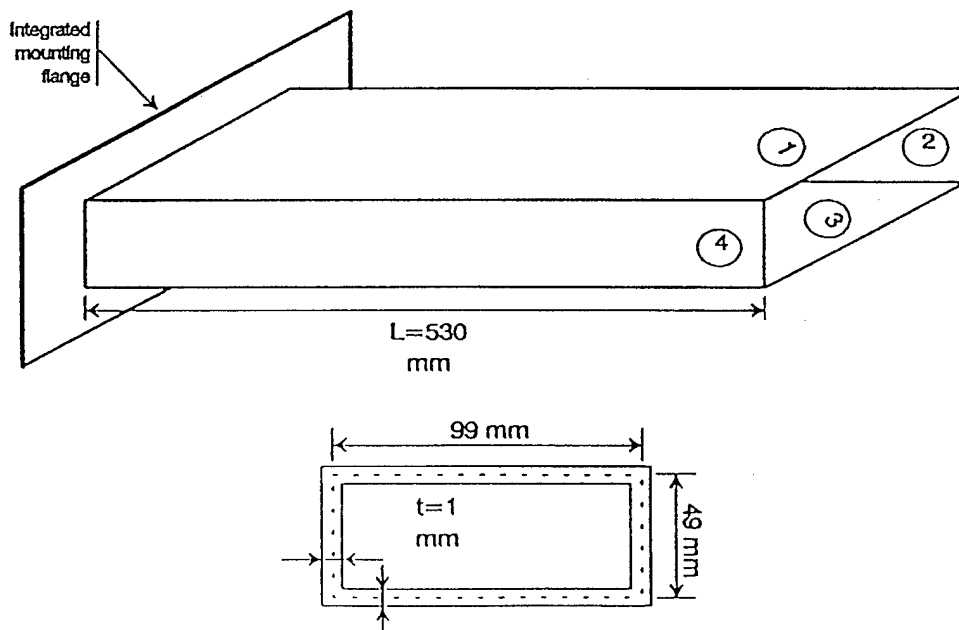
Fig. 7. General dimensions of the test box beams.

a means of checking that pure torsional loading was being applied during test since diagonally opposite quadrants of a structural box subjected to restrained torsional loading will experience the same strain levels. When comparing theory with experiment the average reading from each pair of corresponding gauges was used to provide the experimental data points. Similar strain gauge lay-out configurations were employed for

composite test beams (a) and (b) with slight variations in the number of gauges and/or gauge positions.

The simple engineering analysis procedure detailed in references [24,25] pertaining to the constrained torsional response of single-cell composite box beams precludes the effects on torsional behaviour of cross-sectional distortion and thus membranes or diaphragms were placed inside the test box specimens at seven
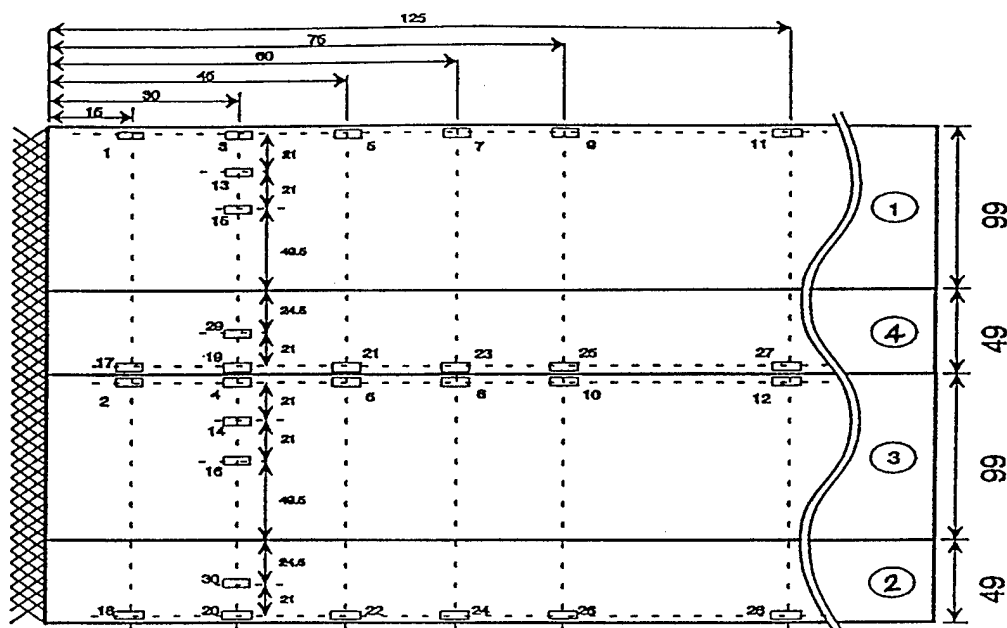
All dimensions in millimeters

Fig. 8. Development of test box-beam showing strain gauge locations.

equally spaced locations along the length of the beams. The diaphragms were 10 mm thick and were made from the same material as the test beams. They were a snug slide fit within the beam cross-sections and thus longitudinal warping displacements were permitted whilst distortion of the cross-sections at the diaphragm locations was prevented.

The testing of the composite box beams was for the constrained condition only with the test procedure being exactly the same as that described for the open-section beams. The torque applied to the composite box-sections was in approx. 22.5 kN-mm increments. Comparisons are given in the paper between the experimental results obtained from the test programme and those determined using the simple engineering analyses procedures outlined in references [23–25] for

open and closed-section beams and these are shown to provide reasonably close agreement.

3. Discussion of results

Comparisons are given in Figs 10–12 between the theoretical predictions and the experimental results associated with the composite angle-section test beam. The angle test beam dimensions and ply material properties are as detailed in Section 2 of the paper and the test data were recorded, as described in that section, at 0.56 kN-mm intervals of applied torque. The lay-up configuration of the angle-section test beam is a symmetric cross-ply of the form [0/0/90/90]$_s$ and the test results have been determined through the use of strain gauges located, as shown in Fig. 5, along the length of the beam on the wall surface at 48 mm from the section shear centre.

The torsional stiffness of the angle-section test beam when associated with constrained warping will, of course, be different to that of the unconstrained beam being subjected to free torsion. Warping restraint will increase the torsional stiffness of a structural section and clearly the degree to which this is so will depend to a very large extent on cross-sectional geometry. In the case of an angle-section, which is associated solely with secondary warping under torsional loading, the increase in stiffness due to warping restraint is quite small. This is noted in Fig. 10 for the angle-section test beam where it is seen that the constrained beam is approx. 1.12 times stiffer than the unconstrained beam.
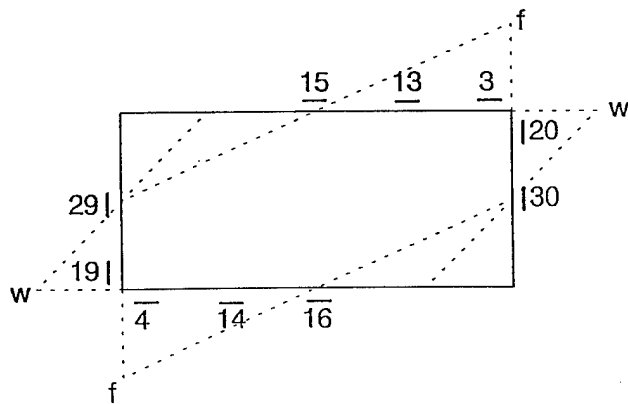
Fig. 9. Location of strain gauges round the test box beam.

Angle Beam Testing Restrained Torsion
Angle of Twist vs Applied Torque
[0/0/90/90]S

Free,Prop'd Th	0	13.35	26.73	40.1
Free,Test	0	13	26	38
Res'd,Prop'd Th	0	11.91	23.82	35.73
Res'd,Test	0	11	23	34

torque (N mm)

– – – Free, Theory   ✳ Free,Test — Res'd, Theory △ Res'd,Test
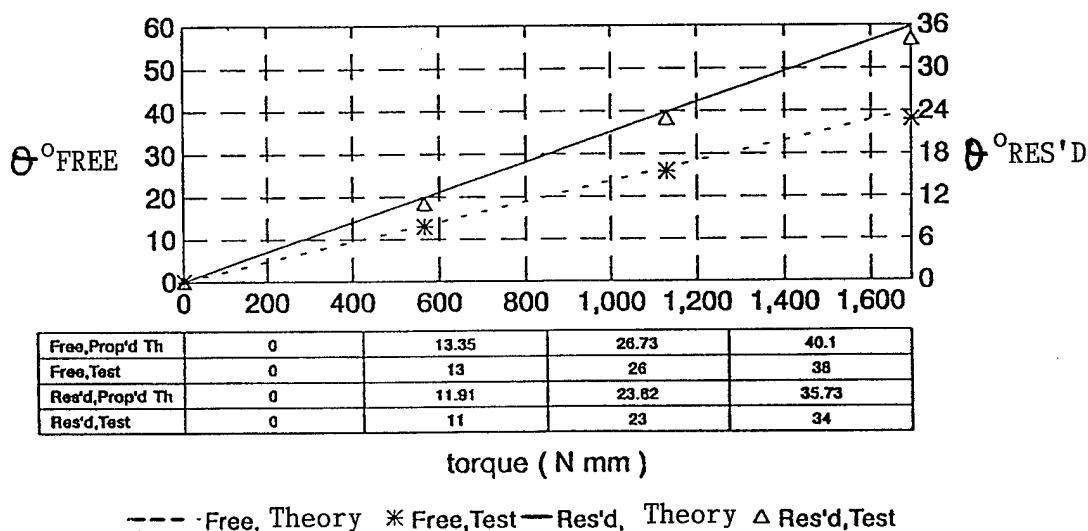
Fig. 10. Angle-beam testing, retstrained torsion. Angle of twist vs applied torque [0/0/90/90]$_s$.

Angle Beam Testing Restrained Torsion
Force Intensity Distribution Along the Length
[0/0/90/90]$_3$

Prop'd Theory	66.220	57.139	49.305	42.547	34.108	31.68	27.340	23.587	20.361	17.568	16.32	15.158	13.084	11.289
Test			48.7		32.9			22.7			15.4			10.4

z axis (mm)

—— Theory ✳ Test
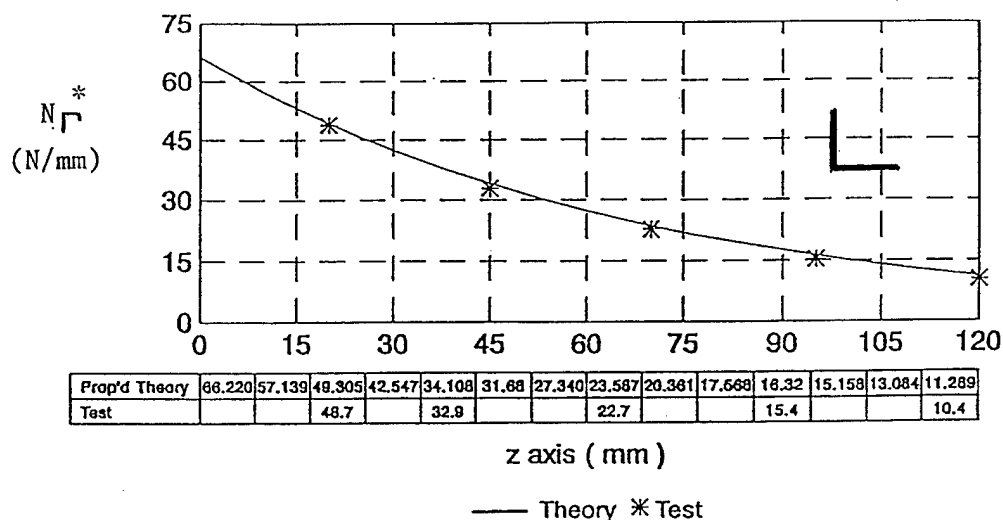
At s=48 mm and T=1130 N mm

Fig. 11. Angle-beam testing restrained torsion. Force intensity distribution along the length [0/0/90/90]$_s$.

This 12% increase is predicted by the composite theory and is shown in Fig. 10 to be closely corroborated by the experimental data.

Figure 11 shows the comparison between theory and test of the variation in force intensity N_r^* with applied torque at the first strain gauge location along the angle-section test beam. This is at a distance of 20 mm from the fixed end of the beam as indicated in Fig. 5. The axial stress system set up in an angle-section beam when subjected to constrained torsion varies linearly through the thickness of its thin walls. It is zero at the wall mid-plane and maximum at the wall surfaces. For the angle-section beam N_r^* is thus defined as the maximum through the thickness bending stress at any

Angle Beam Testing Restrained Torsion
Force Intensity vs Applied Torque
[0/0/90/90]S

Prop'd Theory	0	24.65	49.3	73.9
Test	0	23.2	48.7	73.8

torque (N mm)

—— Theory ✳ Test
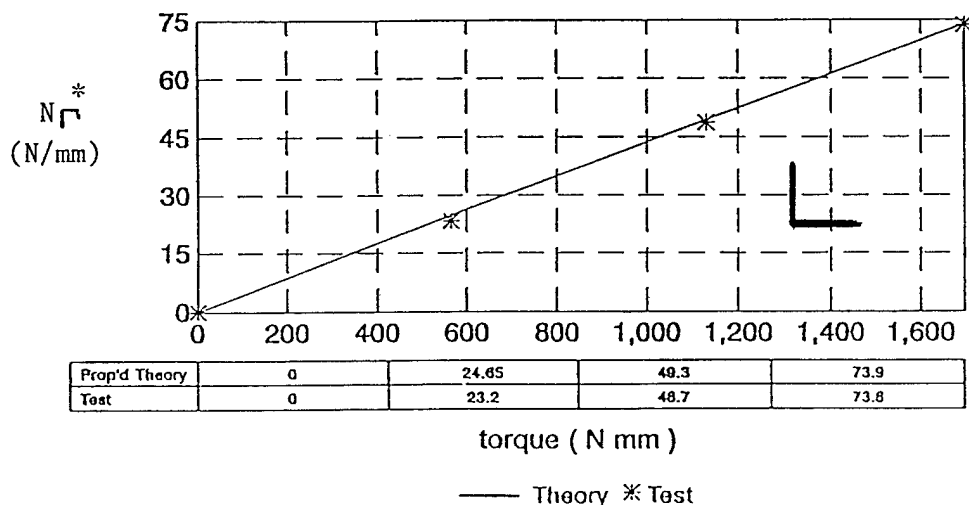
At s=48 mm and z=20 mm

Fig. 12. Angle-beam testing, restrained torsion. Force intensity vs applied torque [0/0/90/90]$_s$.

particular location multiplied by the wall thickness of the section at that location. The comparison between theory and test of the variation in force intensity N_Γ^* with applied torque is shown in Fig. 11 to give remarkably close agreement over the torque range considered.

Figure 12 shows the variation of the force intensity N_Γ^* along the length of the angle-section test beam and corresponding to the applied torque level of 1.13 kN-mm. It is of note that the force intensity diminishes rapidly along the length of the beam from its maximum level at the constrained end and both the theory and experiment are seen to illustrate the same degree of decay along the beam. Indeed, the comparison between theory and experiment is shown to be extremely close. Bearing in mind that the angle-section test beam is 622 mm long it is evident from Fig. 12 that the effects of constrained secondary warping are fairly localized in nature. The level of the force intensity N_Γ^* is noted to diminish by approx. 80% over the 120 mm of beam length covered by the strain gauges in the vicinity of the constrained end.

The experimental data from the two composite Z-section test beams are compared with theoretical predictions in Figs 13–15 for the test beam whose flat walls are all $[(45/-45)_2]_s$ and in Figs 16–18 for the test beam with quasi-isotropic flanges of the form $[45/-45/90/0]_s$ and whose web is $[(45/-45)_2]_s$. All geometric and material property data for the Z test beams are given in Section 2 of the paper and the test data were recorded, as outlined in that section, at torque intervals of approx. 2.25 kN-mm.

Figure 13 indicates the initial torsional stiffness of the Z-beam whose walls are all $[(45/-45)_2]_s$ for both

the free and constrained torsion loading cases. Numerical data are also provided in this figure corresponding to each experimental data point. The comparison between theory and test is shown to be remarkably good with the difference between the two being of the order of 1.7% for the constrained case and 2% for the free case. Of particular interest is the increased stiffness associated with constrained warping. It is noted from Fig. 13 that the constrained beam is approx. 4.4 times stiffer than the unconstrained beam. Although the Z-section beam demonstrates both primary membrane warping and secondary through the thickness bending warping when subjected to torsional loading it is the effects of constrained membrane warping which are predominantly responsible for the large increase in torsional stiffness. For open-section beams which exhibit both primary and secondary warping it is normal practice to preclude secondary effects in analysis and the comparison shown in Fig. 13 clearly corroborates this approach.

The variation in the constrained membrane force intensity N_Γ along the length of the beam, as determined from strain gauges attached to the flange of the cross-section at 2 mm from the flange free edge, is shown in Fig. 14 in comparison with the theoretical prediction. Numerical data are also provided corresponding to each experimental point. The positions of the strain gauges along the length of the beam are as indicated in Fig. 2 and the variations shown correspond to an applied torque of 13.56 kN-mm. As expected, the force intensity N_Γ is a maximum at the constrained end and diminishes along the length of the beam to zero at the free end. The comparison between theory and

Z Beam , Free and Restrained Torsion
$[(45/-45)_2]_s$ Layup
Angle of Twist vs Loading

Res'd,Test	0	0.9	1.8	2.7	3.6	4.5	5.4	6.3	7.2	8.1	9
Res'd,Prop'd Th	0	0.885	1.77	2.655	3.54	4.425	5.31	6.195	7.07899	7.965	8.84999
Free,Test	0	4	8	12	16	20					
Free,Prop'd Th	0	3.92	7.83	11.75	15.67	19.58					

torque (N mm) (thousands)
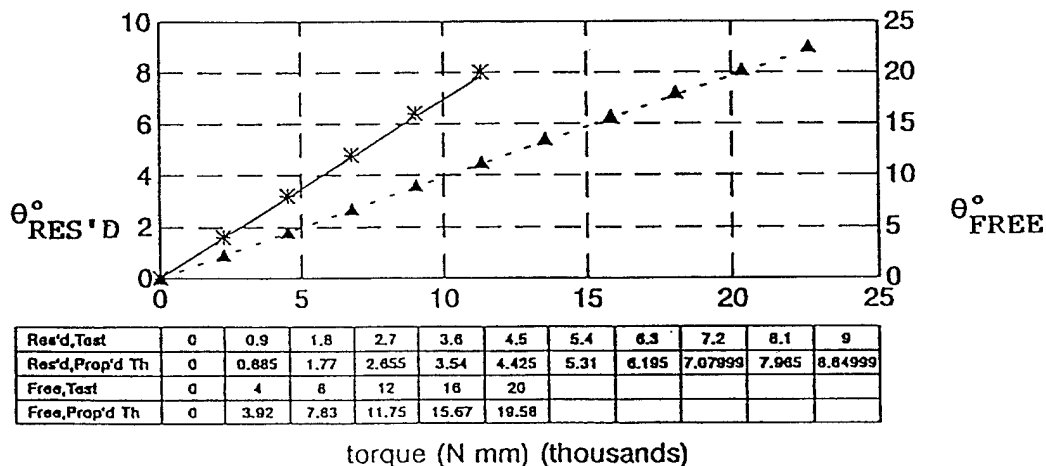
▲ Res'd,Test — Res'd, THEORY✳ Free,Test — Free, THEORY

Fig. 13. Z-beam, free and restrained torstion $[(45/-45)_2]_s$ lay-up. Angle of twist vs loading.

Z Beam , Restrained Torsion
[(45/-45)₂]₈ Layup
Force Intensity Distribution Along the Length

N_Γ
(N/mm)

Test		29.46	26.58	17.97	11.38	4.43	
Prop'd Theory	37.6	32.7	24.6	17.3	10.64	4.32	0

z axis (mm)

✳ Test ━ THEORY
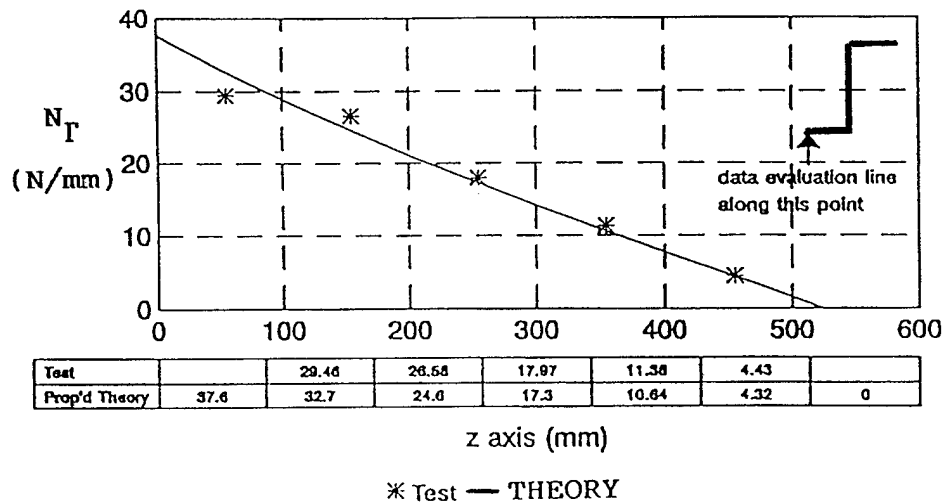
At s=2 mm and T=13560 N mm

Fig. 14. Z-beam, restrained torsion [(45/−45)₂]ₛ lay-up. Force intensity distribution along the length.

experiment is regarded, in this case, as being reasonably good with the discrepancy between the two being largest at the constrained end of the beam and of the order of 10%. Clearly, the effects of constrained primary warping in open-section beams should not be considered to be local in nature. The Z-section test beams are 525 mm long and thus it is to be noted from Fig. 14 that the level of the force intensity N_Γ half-way

along the beam is still of the order of 50% of the maximum value at the constrained end.

A comparison of the constrained force intensity N_Γ round the section, at 155 mm along the beam from the constrained end, is shown in Fig. 15 between theory and experiment. The strain gauge locations round the section are as indicated in Fig. 2 and again the comparison shown corresponds to an applied torque of

Z Beam , Restrained Torsion
[(45/-45)₂]ₛ Layup
Force Intensity Distribution Round the Section

N_Γ
(N/mm)

FLANGE   WEB   FLANGE

Test	26.58	-0.25		-9.36	-9.19		0.29	26.17
Prop'd Theory	24.6	0	-9.36	-9.36	-9.36	-9.36	0	24.6

s (mm)

✳ Test ━ THEORY

At z=155 mm and T=13560 N mm

Fig. 15. Z-beam, restrained torsion [(45/−45)₂]ₛ lay-up. Force intensity distribution round the section.

Z Beam Free and Restrained Torsion
Flanges [45/-45/90/0]$_s$ Web [(45/-45)$_2$]$_s$
Angle of Twist vs Loading

Res'd,Prop'd Th	0	0.52	1.03	1.55	2.06	2.58	3.09	3.61
Res'd,Test	0	0.575	1.1	1.625	2.125	2.675	3.2	3.75
Free,Prop'd Th	0	4.056	8.11	12.17	16.22	20.26	24.34	28.4
Free,Test	0	3.9	7.6	11.7	15.6	19.5	23.4	27.3

torque (N mm) (thousands)

—‒‒Res'd, THEORY ※ Res'd,Test —Free, THEORY △ Free,Test
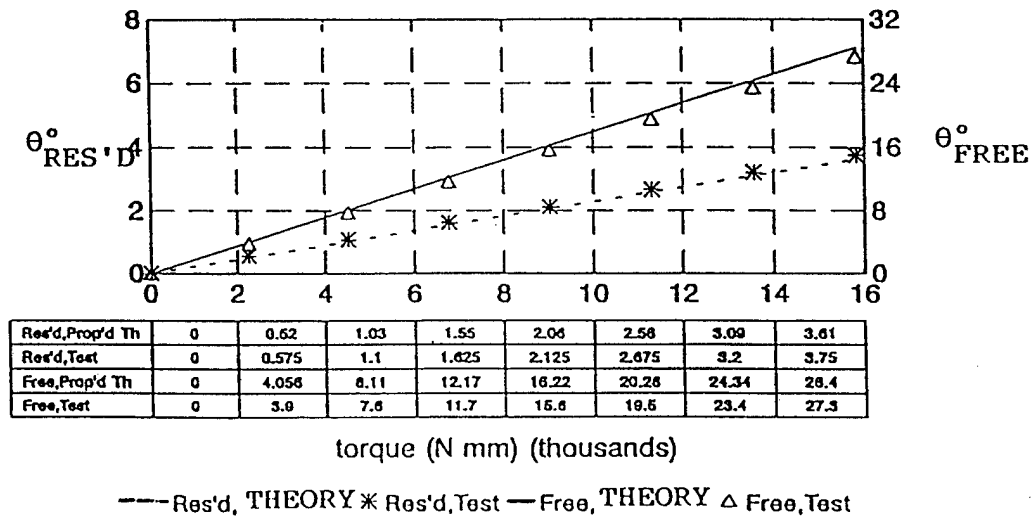
Fig. 16. Z-beam, free and restrained torsion. Flanges [45/−45/90/0]$_s$ web [(45/−45)$_2$]$_s$. Angle of twist vs loading.

13.56 kN-mm. As well as the graphical presentation, Fig. 15 also provides numerical values at the six strain gauge locations round the section. The experimental data are shown, in Fig. 15, to substantially back-up the simple composite theoretical approach. The constant compressive force intensity in the section web is validated as is the zero warping position on the flange of the section which is at a distance of 12.5 mm along the flange from the flange–web junction. The tensile

level of the force intensity at the flange free edges is also verified.

Similar comparisons are made between theory and experiment for the test beam with quasi-isotropic flanges and these are given in Figs 16–18. The strain gauge locations along the beam and around the cross-section are as indicated in Fig. 3. The experimental data are shown in Figs 16–18 to validate the theory to a fairly high degree with respect to all of the

Z Beam Restrained Torsion
Flanges [45/-45/90/0]$_s$ Web [(45/-45)$_2$]$_s$
Force Intensity Distribution Along the Length

Test		43.11	34.66	24.72	15.45	6.44	
Prop'd Theory	49.2	43.98	33.96	24.48	15.36	6.54	0

z axis (mm)

※ Test —— THEORY
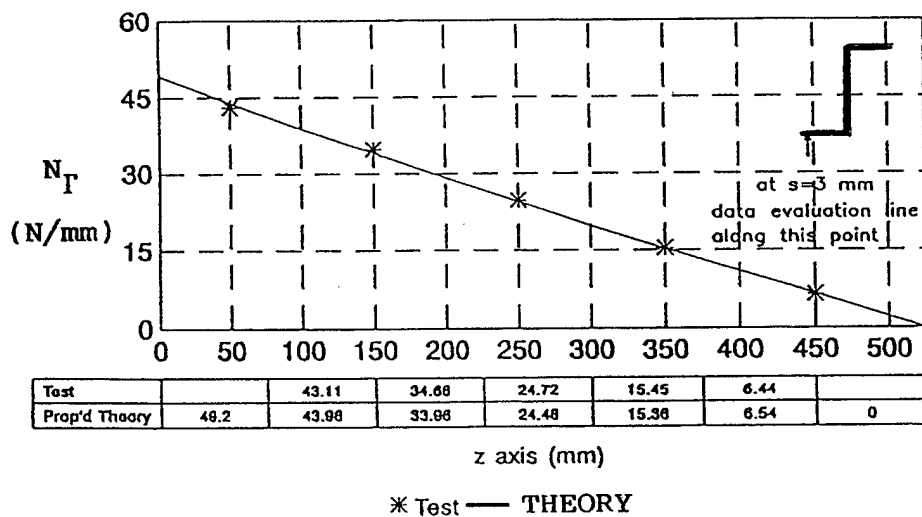
At s=3 mm and T=13560 N mm

Fig. 17. Z-beam, restrained torsion. Flanges [45/−45/90/0]$_s$ web [(45/−45)$_2$]$_s$. Force intensity distribution along the length.

Fig. 18. Z-beam, restrained torsion. Flanges $[45/-45/90/0]_s$ web $[(45/-45)_2]_s$. Force intensity distribution round the section.

Test		34.69	18.97	1.38	-13.69			-7.06	-7.21			36.37	
Prop'd Theory	36.25	33.96	17.9	0	-15.35	-21.08	-7.56	-7.56	-7.56	-7.56	-21.08	33.96	36.25

s axis (mm)

✳ Test —— THEORY
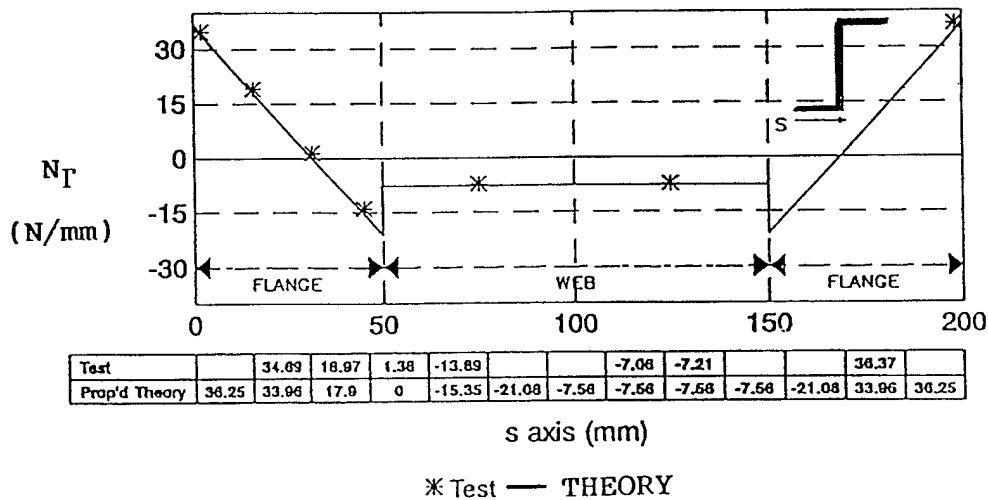
At z=150 mm and T=13560 N mm

behavioural aspects of the beam. It is of particular interest to note the effect of warping restraint on torsional stiffness and thus it can be deduced, from Fig. 16, that the constrained beam is approx. 7.87 times stiffer than the unconstrained beam. This should be compared with the value of 4.4 associated with the test beam whose walls are all $[45/-45_2]_s$ as determined from Fig. 13. Both test beams have the same dimensions and the same number of plies and are therefore of the same weight. The only difference between the two beams is the quasi-isotropic lay-up configuration in the flanges of one and this is noted to be responsible for almost an 80% increase in constrained torsional stiffness.

The comparison between theory and experiment of force intensity N_Γ along the beam is shown in Fig. 17 to be consistently good along the whole length of the beam, even in the vicinity of the constrained end. The comparison between theory and experiment of force intensity N_Γ round the section is shown in Fig. 18 to be extremely good. The constant compressive force intensity in the web is validated by the test data as is the zero warping point in the flange. Due to the different lay-ups in the component flats of the section the zero warping point in the flange is now located at a distance of 18.4 mm along the flange from the flange–web junction. The force intensity variation across the flange is verified by the test data. This is seen to vary linearly from the value of −21.08 N/mm at the flange–web junction to the tensile value of 36.25 N/mm at the flange free edge. The comparisons shown in Figs 17 and 18 are those corresponding to the applied torque

level of 13.56 kN-mm and the variation around the section, shown in Fig. 18, is that occurring at 150 mm along the beam from the constrained end.

Comparisons are given in the paper between the predictions determined from theory and those obtained from the strain analyses of the composite test box beams. These are shown in Figs 19–24 and are the response to an applied torque level of 180.8 kN mm. The experimental data from the composite test box beams whose flat walls are all of the same lay-up configuration is compared with theoretical predictions in Fig. 19 for the $[(45/-45)_2]_s$ case and in Fig. 20 for the $[45/0/-45/90]_s$ quasi-isotropic design. The comparisons given are those of the longitudinal distribution of force intensity N_Γ in the web of the test beams at s = 21 mm from the horizontal geometric centreline of the composite box cross-section as indicated. Numerical data are also provided in these figures corresponding to each experimental data point. The composite theory based on the approach of Benscoter [21] for isotropic beams is seen to be able to represent actual behaviour fairly well and with, what can be described as, an engineering accuracy. The effect of neglecting the warping shear strain in analysis is represented in Figs 19 and 20 by the composite theory based on the approach of Von Karman and Christensen [20] for isotropic beams. It is noted that this preclusion clearly results in erroneous predictions.

The experimental data from the composite test box beam with quasi-isotropic flanges of the form $[45/0/90/-45]_s$ and whose webs are $[(45/-45)_2]_s$ is compared with theoretical predictions in Fig. 21 and

Box Section Restrained Torsion
Force Intensity Distribution Along the Length
[(45/-45)₂]ₛ

Nᵣ (N/mm)

CT-VK&C			8.4	4.5	2.42	1.3	0.69	0.37	0.2	0.11	0.06	0.03	0.02	0.001	0.000	0
CT-BEN	9.74	7.91	6.43	5.243	4.246	3.435	2.62	2.278	1.847	1.464	1.211	0.994	0.831	0.343	0.144	0.108
TEST			4.59		2.31		1.32		0.71		0.18

z-axis
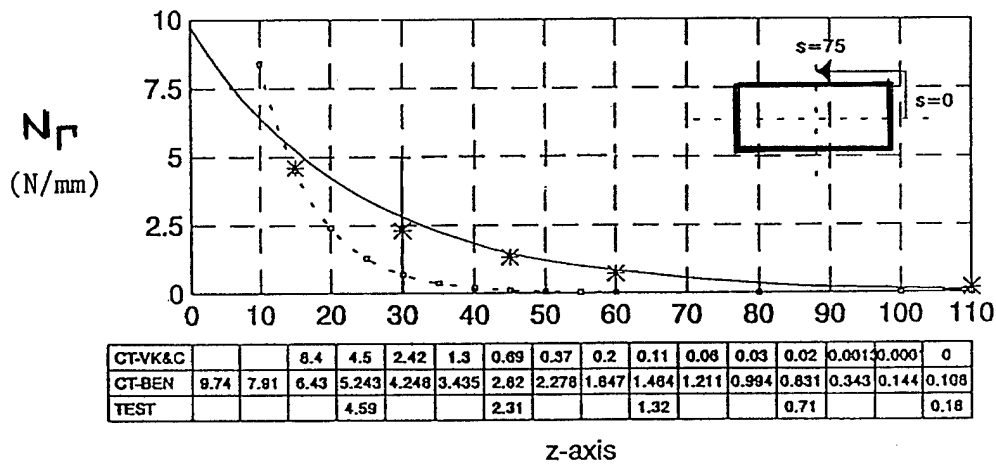
-•·CT-VK&C —CT-BEN ✳TEST

Along the line at s=21 mm, T=180800 N mm

Fig. 19. Box-section, restrained torsion. Force intensity distribution along the length [(45/−45)₂]ₛ.

Fig. 22 which describe the variation in longitudinal force intensity N_Γ in the flange and web respectively. The locations on the cross-section at which the longitudinal variations are compared are measured from the horizontal geometric centreline of the composite box. These are at s = 33 mm for the flange location as indicated in Fig. 21 and at s = 21 mm for the web location as indicated in Fig. 22. The comparisons given in Figs 21 and 22 are seen to clearly favour the composite theory based on the assumptions of Benscoter [21] and again to indicate that the assumptions proposed by Von Karman and Christensen [20] result in a theory which is less able to predict actual behaviour.

In view of the fact that the composite box test beams are 530 mm long it is clear from Figs 19–22 that the effects of constrained membrane warping in closed-cell

Box Section Restrained Torsion
Force Intensity Distribution Along the Length
[45/0/-45/90]ₐ

Nᵣ (N/mm)

CT-VK&C	19.86	13.22	8.8	5.86	3.9	2.6	1.73	1.15	0.77	0.51	0.34	0.23	0.15	0.07		0
CT-BEN	11.39	9.94	8.68	7.68	6.62	5.78	5.05	4.41	3.85	3.36	2.93	2.58	2.24	1.71	0.99	0.58
TEST	10.32			6.8			4.32			2.66			1.95			0.56

z-axis
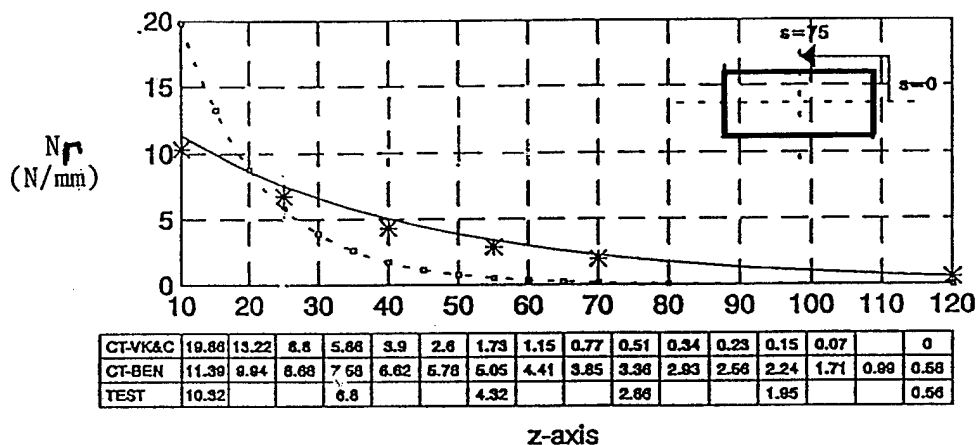
-•·CT-VK&C —CT-BEN ✳TEST

Along the line at s=21 mm, T=180800 N mm

Fig. 20. Box-section, restrained torsion. Force intensity distribution along the length [45/0/−45/90]ₛ.

Box Section Restrained Torsion
Force Intensity Distribution Along the Length
Flanges [45/0/90/-45]$_8$ Webs [(45/-45)$_2$]$_3$

CT-VK&C	18.96	14.4	10.91	8.29	6.20	4.77	3.62	2.75	2.06	1.56	0.69	0.1	0.05
CT-BEN	15.22	13.05	11.19	9.61	8.24	7.07	6.07	5.21	4.47	3.63	2.42	0.83	0.62
TEST	14			7.87			4.82			3.06	2		0.43

z-axis

——CT-VK&C ——CT-BEN ✳TEST

Along the line at s=33 mm, FLANGE, T=180800 N mm

Fig. 21. Box-section, restrained torsion. Force intensity distribution along the length. Flanges [45/0/90/—45]$_s$ web [(45/—45)$_2$]$_s$.

construction are, effectively, local in nature. The variation in force intensity N_Γ along the length of the test box beams is noted in Figs 19–22 to decay rapidly to almost zero within approx. one fifth of the beam length from the constrained end. This is to be contrasted with the effects of constrained membrane warping in open-section beams. Figures 14 and 17 show that the effects

of constrained membrane warping are considerable for composite Z-sections. They do not diminish rapidly along the beam and are, in fact, noted to be significantly evident at locations far removed from the constrained end.

The variation in force intensity N_Γ round the section for the composite test box beam whose flange and web

Box Section Restrained Torsion
Force Intensity Distribution Along the Length
Flanges [45/0/90/-45]$_3$ Webs [(45/-45)$_2$]$_3$

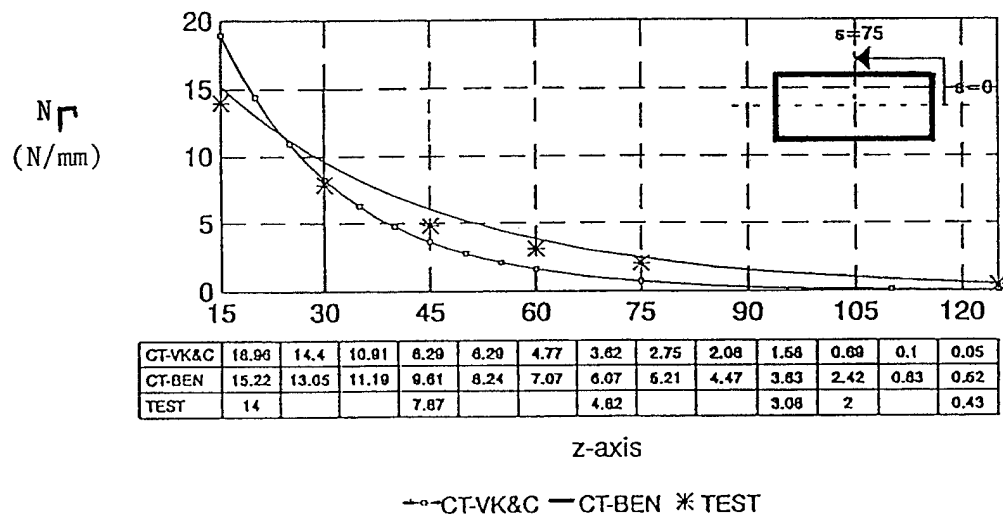| CT-VK&C | 14.09 | 10.7 | 8.11 | 6.16 | 4.67 | 3.54 | 2.69 | 2.04 | 1.55 | 1.18 | 0.51 | | 0.03 |
| CT-BEN | 11.3 | 9.7 | 8.32 | 7.14 | 6.12 | 5.26 | 4.51 | 3.87 | 3.32 | 2.85 | 1.8 | 0.62 | 0.39 |
| TEST | 10.06 | | | 5.66 | | | 3.41 | | | 2.16 | 1.4 | | 0.32 |

z-axis

-·-CT-VK&C ——CT-BEN ✳TEST
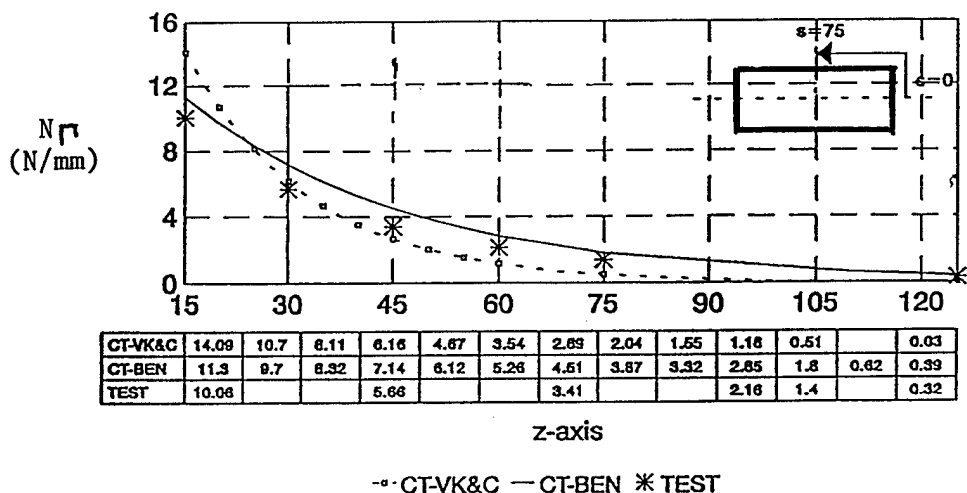
Along the line at s=21 mm, WEB, T=180800 N mm

Fig. 22. Box-section, restrained torsion. Force intensity distribution along the length. Flanges [45/0/90/—45]$_s$ web [(45/—45)$_2$]$_s$.

Box Section Restrained Torsion
Force Intensity Distribution Round the Section
[(45/-45)₂]ₛ

CT-VK&C	0	0.60	0.62	0.69	0.35	0
CT-BEN	0	2.6	3.33	2.6	1.4	0
TEST	0.27	2.2		2.38	1.24	0.16

s-axis

- - - CT-VK&C — CT-BEN X̄ TEST
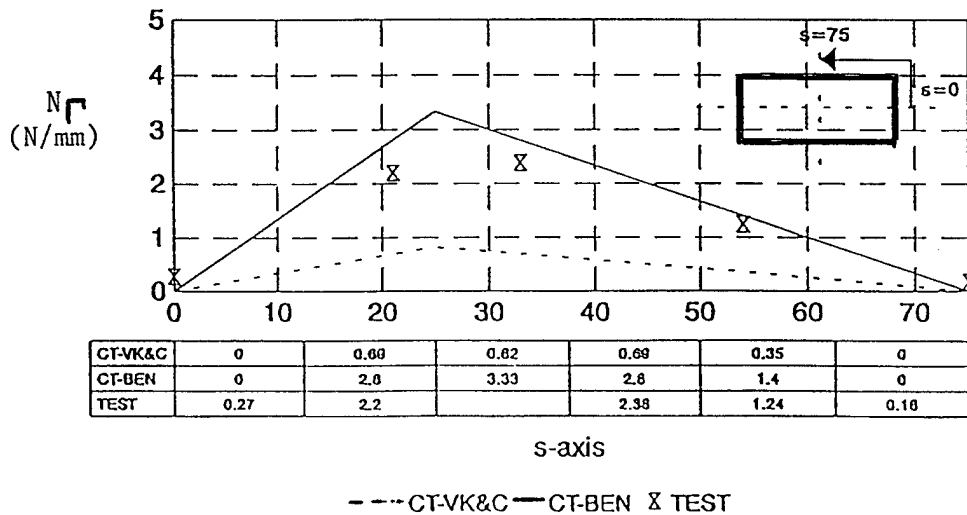
At z=30 mm , T=160000 N mm

Fig. 23. Box-section, restrained torsion. Force intensity distribution round the section [(45/−45)₂]ₛ.

elements are laid-up in the form [(45/−45)₂]ₛ are shown in Fig. 23. The variation indicated is that at the cross-section located at z = 30 mm from the fixed end of the beam. Numerical data are provided in Fig. 23 corresponding to each strain gauge location round the section and the comparison between theory and experiment is noted to clearly support the composite theory

based on the isotropic analysis approach of Benscoter [21]. It is of particular note that the strain gauges located on the geometric centrelines of the composite box cross-section, at s = 0 mm and s = 75 mm, register, as expected, almost zero strains. It is also of note that ignoring the warping shear strains in analysis is seen to result in force intensity levels which are of the order of

Box Section Restrained Torsion
Force Intensity Distribution Round the Section
[45/0/-45/90]ₛ

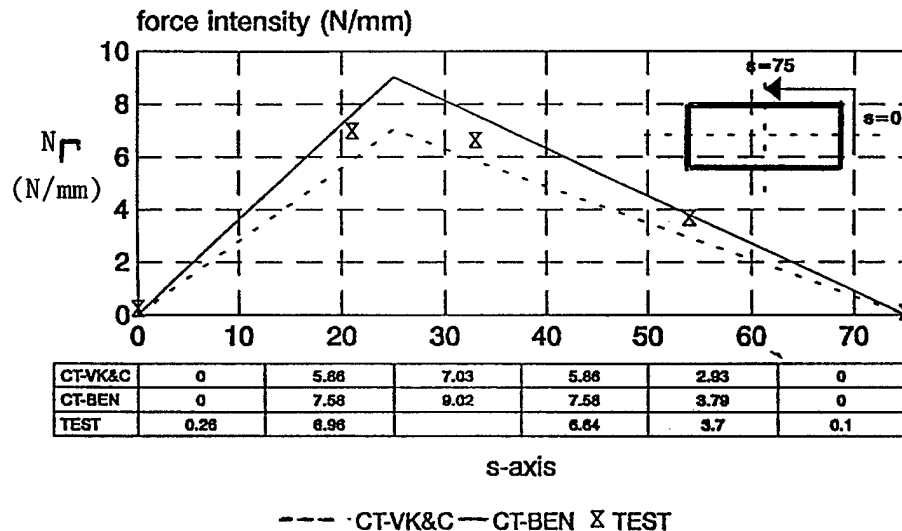| CT-VK&C	0	5.86	7.03	5.86	2.93	0
CT-BEN	0	7.58	9.02	7.58	3.79	0
TEST	0.26	6.96		6.64	3.7	0.1

s-axis

- - - · CT-VK&C — CT-BEN X̄ TEST

At z=25 mm , T=180800 N mm

Fig. 24. Box-section, restrained torsion. Force intensity distribution round the section [(45/0/−45/90)]ₛ.

one quarter of those determined when they are duly accounted for.

Figure 24 shows a similar comparison of the variation in force intensity N_{Γ} round the section for the quasi-isotropic composite test box beam. The variation indicated is that at the cross-section located at $z = 25$ mm from the fixed end of the beam. In this case it would appear that the difference between the two composite theoretical approaches, based on the isotropic works of Von Karman and Christensen [20] and Benscoter [21] respectively, is not great and this is indeed true for the $z = 25$ mm location under consideration. The experimental data are noted to lie between the two solutions with the tendency to lean slightly more towards the theory based on the Benscoter [21] assumptions. With reference to Fig. 20, however, it is clear that the difference between the two approaches is much more significant at other locations along the length of the quasi-isotropic box beam.

4. Concluding comments

Details are reported in the paper of an experimental programme of work pertaining to the restrained torsional response of thin-walled open and closed-section carbon fibre composite beams. In particular, consideration has been given to the cantilever configuration with torque applied at the free end and some detailed attention has been paid to the effects of both primary or membrane warping and secondary or through the thickness bending warping. Tests have been carried out on zed and angle section composite beams and on closed single-cell box-section beams. The stress distributions along the beams and around their cross-sections, as determined from the measured strains during test, are shown in the paper to be in favourable agreement with those determined using the simple engineering theories detailed by the authors in references [23–25].

Composite angle sections are known to exhibit secondary warping only, when subjected to torsional loading. The effects of constraining this through-the-thickness warping are noted in the paper to be local in nature and to diminish rapidly within, approximately, a one fifth length of the beam from the constrained end. Although it is normally considered that secondary warping effects can be ignored in thin-walled construction it is clear that significantly high axial stresses are possible at the constrained end of the beam for the case of the composite angle section. It is shown that the constrained secondary warping of angle sections increases the torsional stiffness of the beam only marginally, of the order of 10–15%.

Both primary and secondary warping occur when a composite Z-section is subjected to torsional loading.

The torsional response of open-sections which possess both forms of warping is governed, in the main, by primary effects and thus it is normal practice to preclude the effects of secondary warping in the analysis procedures employed for these sections. This has most certainly been proved to be the case for the composite Z-section test beams discussed in this paper. The simple engineering theoretical approach, described in some detail in references [23,25], considers constrained membrane effects only and this is shown to provide remarkably close agreement with the actual response of the composite test beams.

The effects of constraining the membrane warping of a composite Z-section beam are noted in the paper to be considerable all along the beam and not just confined to a region along its length in the vicinity of the constrained location. It is indicated in the paper that constraining the membrane warping of a Z-section increases its torsional stiffness substantially. For the composite Z-section test beams considered, the increase in torsional stiffness is noted to be more than four times that of the unconstrained beam for the angle-ply lay-up configuration and almost eight times that of the unconstrained beam for the configuration with quasi-isotropic flanges. The only difference between the two test beams is the lay-up configuration in their flanges and thus the importance of fibre orientation in composite construction is duly noted.

The effects of constraining the membrane warping of composite, single-cell, box-section beams are shown in the paper to be similar in form to those associated with the constrained secondary warping of angle section beams. The constrained axial force intensity distribution along the length of the composite box beams is noted in the paper to be local in nature and to diminish from its maximum level at the fixed end of the beam to almost zero within, approximately, a one fifth length of the beam from the fixed end. This is realized by both theory and experiment and the comparison between the two is shown to be good. The simple engineering theoretical approach for the composite box beams is set out in some detail by the authors in references [24,25]. In particular it has been shown that the composite theory based on the assumptions of Benscoter [21] for isotropic beams is able to represent the actual behaviour of the composite test box beams fairly closely and that the assumption of neglecting the warping shear strain in analysis, as proposed by Von Karman and Christensen [20], gives poor correlation with the experimental findings.

References

[1] Bauchau OA, Coffenberry BS, Rehfield LW. Composite box beam analysis: theory and experiments. Journal of Reinforced Plastics and Composites 1987;6:25–35.

[2] Chandra R, Stemple AD, Chopra I. Thin-walled composite beams under bending, torsional, and extensional loads. Journal of Aircraft 1990;27(7):619–626.

[3] Chandra R, Chopra I. Experimental and theoretical analysis of composite I-beams with elastic couplings. IAA Journal 1991;29(12):2197–2206.

[4] Snell MB, Greaves LJ. Buckling and strength characteristics of some CFRP stiffened curved panels. Thin-Walled Structures 1991;11:149–176.

[5] Kim ZG, Hong CS, Kim CG. Postbuckling analysis of stringer-stiffened composite laminated cylindrical panels. Journal of Reinforced Plastics and Composites 1995;14(8):827–846.

[6] Eiblmeier J, Loughlan J. The buckling response of carbon fibre composite panels with reinforced cut-outs. Composite Structures 1995;32:97–113.

[7] Brooks RJ, Turvey GJ. Lateral buckling of pultruded GRP I-section cantilevers. Composite Structures 1995;32:203–215.

[8] Kruger R, Konig M, Albinger J, Hansel C. Combined experimental–numerical approach for the determination of mixed-mode energy release rates at delamination growth. AIAA-94-1460-CP.

[9] Cairns DS, Minguet PJ, Abdallah MG, The influence of size and location on the response of composite structures with delaminations loaded in compression. AIAA-94-1535-CP.

[10] Rogers CA, Liang G, Li S. Active damage control of hybrid material systems using induced strain actuator. AIAA/ASME/ASCE/AHS/ASC Structures, Structural Dynamics, and Materials Conference, 1991:1190–1203.

[11] Agnes GS, Silva K. Aircraft smart structures research in the USAF Wright Laboratory. AGARD Structures and Materials Panel, 75th Meeting, Smart Structures for Aircraft and Spacecraft, Lindau, Germany, 5–7 October 1992.

[12] Roberts SSJ, Butler RJ, Davidson R. Progress towards a robust, user friendly, system for active structural damping. Second European Conference on Smart Structures and Materials, Glasgow, Scotland, 12–14 October 1994.

[13] Thompson SP, Loughlan J. The active buckling control of some composite column strips using piezoceramic actuators. Compo-site Structures 1995;32:59–67.

[14] Caneva C, Olivieri S, Santulli C, Bonifazi G. Impact damage evaluation on advanced stitched composites by means of acoustic emission and image analysis. Composite Structures 1993;25:121–128.

[15] Sharma SK, Sankar BV. Sublaminate buckling and compression strength of stitched uniweave graphite/epoxy laminates. Journal of Reinforced Plastics and Composites 1997;16(5):425–434.

[16] Yeh HY, Chen VL. Experimental study and simple failure analysis of stitched J-stiffened composite shear panels. Journal of Reinforced Plastics and Composites 1996;15(11):1070–1087.

[17] Little RE, Mitchell WJ, Mallick PK. Tensile creep and creep rupture of continuous strand mat polypropylene composites. Journal of Composite Materials 1995;29(16):2215–2227.

[18] Tuttle ME, Koehler RT, Keren D. Controlling thermal stresses in composites by means of fibre prestress. Journal of Composite Materials 1996;30(4):486–502.

[19] Jian XH, Tzou HS, Lissenden CJ, Penn LS. Damage detection by piezoelectric patches in a free vibration method. Journal of Composite Materials 1997;31(4):345–359.

[20] Von Karman T, Christensen NB. Methods of analysis for torsion with variable twist. Journal of the Aeronautical Sciences 1944;11:110–124.

[21] Benscoter SU. A theory of torsion bending for multicell beams. Journal of Applied Mechanics 1954;20:25–34.

[22] Ata M. Torsional analysis of thin-walled fibrous composite beams. PhD thesis, Cranfield University, College of Aeronautics, Cranfield, Bedford, UK, November 1992.

[23] Loughlan J, Ata M. The restrained torsional response of open section carbon fibre composite beams. Composite Structures 1995;32:13–31.

[24] Loughlan J, Ata M. The constrained torsional characteristics of some carbon fibre composite box beams. Thin Walled Structures 1997;28(34):233–252.

[25] Loughlan J, Ata M. The behaviour of open and closed-section carbon fibre composite beams subjected to constrained torsion. Composite Structures 1997;38:631–647.

Development of a metal test box configuration to test a range of skin panels of a composite horizontal stabilizer

J. C. F. N. van Rijn*, H. G. S. J. Thuis

National Aerospace laboratory, Structures Department, Voorsterweg 31, 8316 PR Marknesse, The Netherlands

Abstract

Within the framework of a national technology programme under a contract awarded by the Netherlands Agency for Aerospace Programmes (NIVR), a composite stabilizer was developed by Fokker Aircraft B.V. in close collaboration with NLR. One of the activities in this technology program for NLR was to develop a test box for testing large composite skin panels and to test the composite panels on this box. The main goals of this part of the program were:

— To develop a single test box on which a number of test panels with different configurations could be loaded to relatively high strain levels without incurring damage to the test box;
— To load the test panels in such a way that an optimum correspondence between strain distributions in the test panels and the horizontal stabilizer skins was attained;
— To validate the design concepts of the skin panels by comparison of calculated and measured strain distributions.

All objectives have been met successfully.

— Six different panels were tested on a single metal test box. The panels were loaded up to a maximum of 3.0 times Limit Load with a total of 21 different loading conditions without incurring any damage to the metal test box.
— The loading of the test panels was such that an acceptable correspondence of the measured strain distributions and the calculated strain distributions in the horizontal stabilizer skins was attained.
— The measured strain distributions compared quite well with the calculated strain distributions for the test panels.

1. Introduction

Under a contract awarded by the Netherlands Agency for Aerospace Programmes (NIVR), a national technology programme was carried out in close collaboration between Fokker Aircraft B.V. and the National Aerospace Laboratory. The goal of this technology programme was to develop the technology required to design, fabricate and certify a carbon fibre reinforced plastic (CFRP) horizontal stabilizer. To achieve this goal the building block approach was used [1].

In this building block approach all aspects were addressed starting at the material level (by testing thousands of small coupons), through a large number of small components (e.g. by testing hundreds of small skin panel and spar details), to sub-assemblies of increasing complexity, up to the level of a complete torsion box of the composite stabilizer.

Large composite skin panels were among the larger sub-assemblies to be developed. The panels were designed and manufactured by Fokker Aircraft B.V. and tested by NLR. Four different panel configurations were tested which were representative for skin panels of the upper and lower skin and encompassed the centre and root section of the stabilizer skin panels.

To test these large composite skin panels in a correct way it was deemed necessary to mount the panels on a box structure in order to get a realistic build-up of the bending and torsional moments towards the centre section of the panels.

This paper addresses the development of the metal test box and the methodology to determine the actuator input loads. In addition panel test results, obtained during the box tests, are compared to finite element calculations.

*Corresponding author.

The definition of the composite skin panels in relation to the composite horizontal stabilizer skins are briefly discussed. The test box concept and test set-up are explained in detail. The finite element modelling technique of the test box and the composite skin panels is presented. The use of finite element analysis to obtain loading conditions for the test box is presented. The test programme is briefly described. The comparison of some experimental results with finite element analysis results is given. Finally, some conclusions are drawn.

2. The development of the test box

The objectives of the test box programme were:

— To develop a single metal test box on which a number of composite skin panels with different configurations could be loaded up to failure without causing damage to the metal test box.
— To determine the actuator loads to load the test panels in the same way as the composite horizontal stabilizer.

2.1. The test panels

The main load carrying component of the horizontal stabilizer is the horizontal stabilizer torsion box. The main components of the torsion box are the upper and lower skins, the aft, rear and auxiliary spars and the ribs. The torsion box comprises composite front, rear and auxiliary spars with L-stiffeners, dimpled metal ribs, sandwich composite ribs and several metal fittings.

The skin panels were stiffened by blade stiffeners which were cobonded to the skin laminate. At the transition of the inboard and outboard parts of the panels, stiffener run-outs were used in combination with doublers.

Four different test panel configurations were tested on the metal test box which were derived from the lower and upper skins of the composite horizontal stabilizer (Lower Aft, Lower Front, Upper Aft and Upper Front). Their locations relative to the skin panels of the composite stabilizer are shown in Fig. 1.

A detailed view of one of the test panels is given in Fig. 2. The test panels were made of unidirectional carbon/epoxy prepreg tape HTA/6376. All test panels except for the Lower Front panel, were configured with an inspection hole at the root of the panel (see Fig. 2). All edges of the test panels were reinforced with tabs to allow a proper load introduction.

The Aft test panels were configured with a rearward extension, which functions as an elevator support in the composite horizontal stabilizer.

2.2. The metal test box concept

In Fig. 3 a view of the metal test box is given, in which the various parts are named. Figure 4 gives a cross sectional view of the box, with a test panel attached.

The metal test box contains steel spar simulations and steel rib simulations, which support the test panels
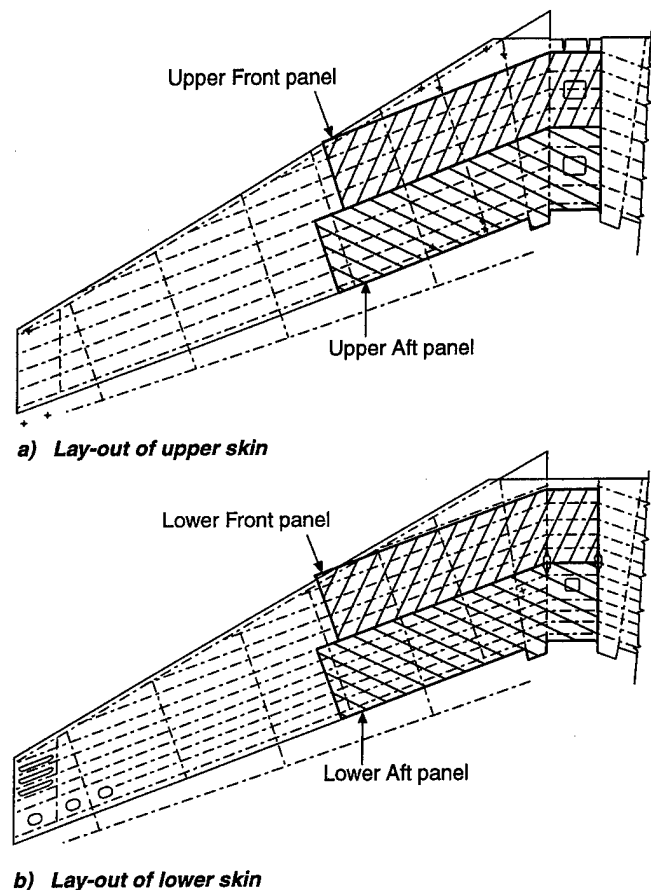

a) **Lay-out of upper skin**

b) **Lay-out of lower skin**

Fig. 1. Lay-out of skins and locations of test panels.
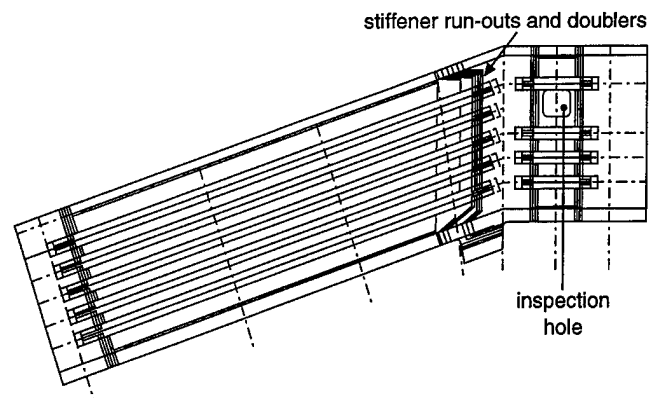
Fig. 2. Lower Aft test panel.
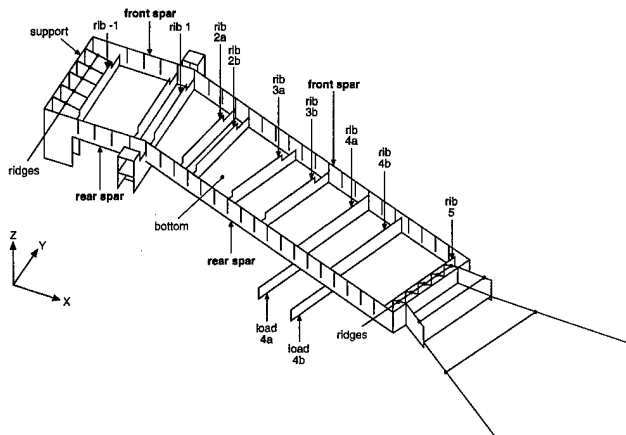
Fig. 3. Metal test box configuration and nomenclature.

Fig. 5. Side view of the metal test box showing the slits in the steel spars.

and provide for a build-up of the strains in the test panels towards the centre section, as well as a steel bottom plate (see Fig. 3).

The metal test box was configured with steel ribs for lower as well as upper skin panels. In this way four different skin panels could be loaded on the same metal test box. The rib simulations to be used with the aft-panels are indicated with 'a' in Fig. 3, the rib simulations to be used with the front-panels are indicated with 'b'.

The composite test panels were connected to the metal test box using aluminium parts. The edges of the test panels were connected to the steel spar simulation of the metal test box by angle sections. The test panels were connected to the metal rib simulations by aluminium ribs as shown in Fig. 4.

One of the problems which had to be solved was to avoid permanent deformation or even failure c⁻ he metal test box when loading the test panels up to failure. Therefore the spars of the metal test box were configured with slits (see Fig. 5), which allowed the test panel to be deformed up to relatively high strain levels, while keeping the metal test box relatively unaffected in case of a loading in bending.

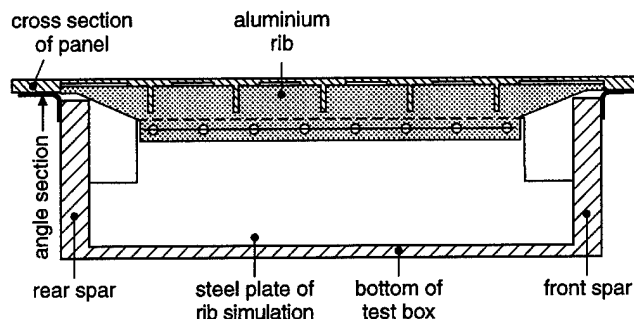However, in case of a test panel failure in tension, this spar concept might still lead to permanent damage

in the metal test box. Therefore, the spars of the metal test box were equipped with chains (see Figs 5 and 6). Each spar was equipped with two steel chains: one inside and one outside the metal test box. The chains have slotted holes. These slotted holes allow the metal test box to deform to a certain degree. If the deformation of the metal test box exceeds this level, the slotted holes of the chains will begin to pick up loads and hence the chains will limit the deformation of the metal test box.

In case of a composite panel failure in compression, the slits in the spars are configured so that they will make contact with each other and hence will limit the deformation of the metal test box. Fig. 6 shows a detail of the slit spar of the metal test box, the location of the chain at the outside of the spar and the aluminium angle sections which are used to connect the composite skin panels to the metal test box.

Figure 7 shows the top view of the complete metal test box. The figure clearly shows the locations of the chains. The different rib locations can also be seen. Two rigid steel bars are connected to the end of the metal test box. By connecting hydraulic actuators at the end of these bars the required bending moments can be applied to the composite skin panels.
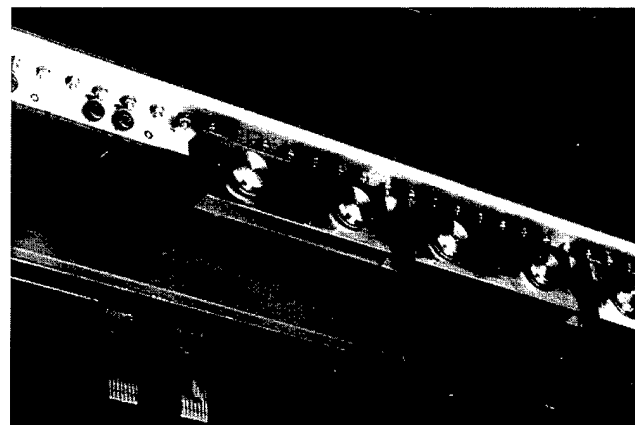

Fig. 4. Cross section of metal test box including a test panel.

Fig. 6. Detail of the slit spar equipped with the chain.

Fig. 7. Top view of the metal test box.

Fig. 9. Detail of mechanism used to apply elevator loads.
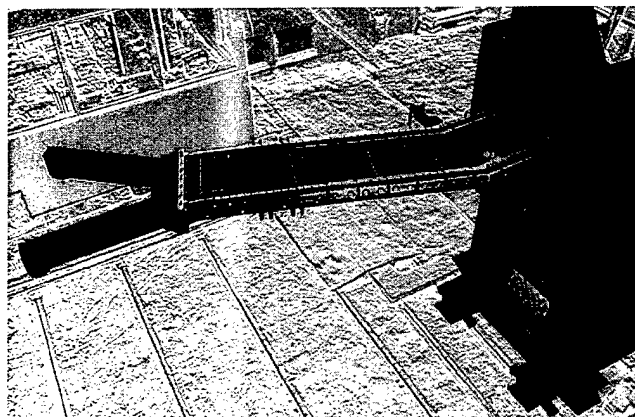
2.3. The metal test box test set-up

The metal test box was connected to a rigid frame. Loads were introduced to the metal test box by six hydraulic actuators: five positioned vertically (F_{z1}, F_{z2}, F_{z3}, F_{z5} and F_{z6} see Fig. 8) and one positioned horizontally (F_{y1} see Fig. 8). The loads of actuators F_{z1} and F_{z2} were introduced at the end of the box through two beams. Elevator loads were introduced to the aft panels by a dead weight using a mechanism (see Fig. 8 and Fig. 9).

3. Finite element models

Finite element analyses were performed using NASTRAN, of the metal test box configuration including the composite test panels, as well as of the composite horizontal stabilizer. In this section the finite element models of the composite horizontal stabilizer,
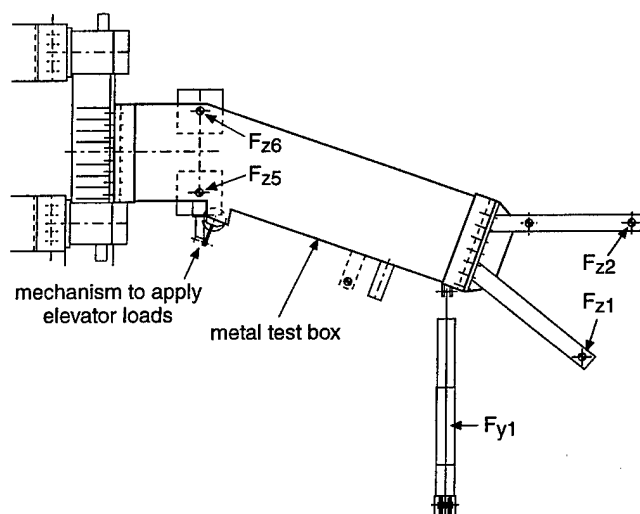
of the metal test box and of the test panels are described.
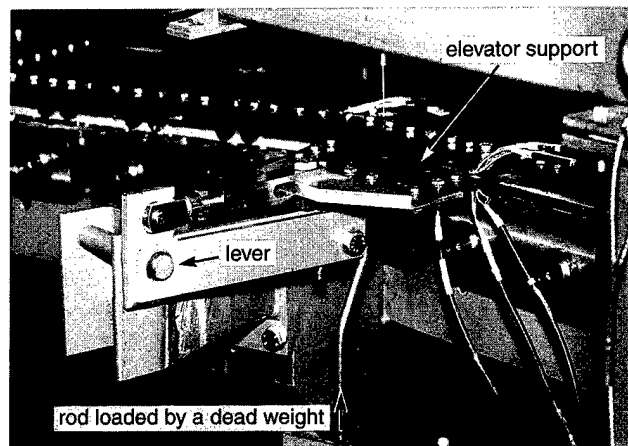
3.1. Composite horizontal stabilizer model

The finite element model of the composite horizontal stabilizer is shown in Fig. 10.

The finite element model contains 2444 nodes, 2667 4-node quadrilateral or 3-node triangular shell elements and 1262 beam elements.

3.2. Test box model

A top view of the finite element model of the test box (looking inside the box) is shown in Fig. 11. The finite element model contains 1147 nodes, 1002 4-node-quadrilateral shell elements and 14 2-node-beam elements.

The dimensions of the finite element model of the box were dictated by the dimension of the panels, since test box and panel finite element models were to be connected.

A further description of some of the parts, which are indicated in Fig. 3, are given in the next sections.
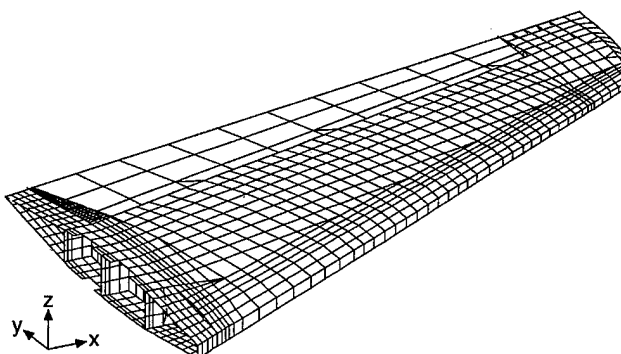

Fig. 8. Top view of the metal test box set-up.

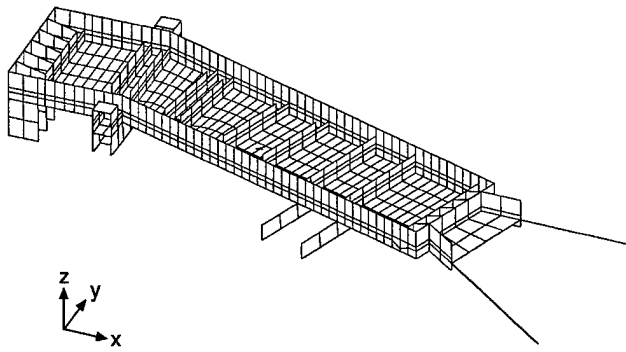Fig. 10. Composite horizontal stabilizer finite element model.

Fig. 11. Finite element model of the test box.

3.2.1. Finite element models of spar simulations

The actual spar configuration and its finite element representation are shown in Fig. 12. The actual design of the spar simulations is too complicated to be incorporated in the finite element model. Since the large slits will accommodate virtually all displacement, these are modelled with double nodes.

3.2.2. Finite element models of rib simulations

In Fig. 4 a cross section of the test box is given. It was deemed necessary to incorporate the actual height of the aluminium rib, because the stiffness of the combined rib simulations is dominated by the stiffness of the aluminium part. In the finite element model the height of the aluminium rib is the distance between the top of the spar simulation and the top of the rib simulation.

3.2.3. Applied loads and boundary conditions

The applied loads and boundary conditions for the finite element model are indicated in Fig. 13.

The nodal forces F_{z1}, F_{z2}, F_{z3}, F_{z5} and F_{z6} act in the direction of the positive z-axis. The nodal force F_{z3} acts on the location indicated by load 4a in Fig. 4 for the aft panels and on the location indicated by 4b for the forward panels.

The nodal force F_{y1} acts in the direction of the positive global y-axis.

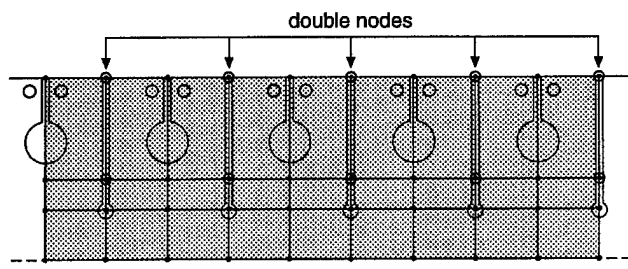All displacements are constrained for the 14 nodes at the upper and lower edge of the support plate.

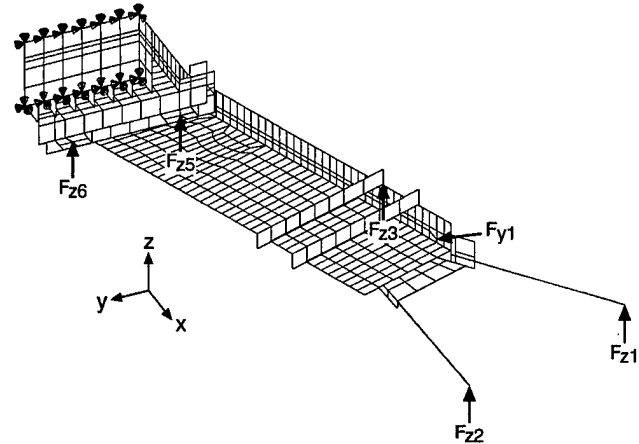Fig. 12. Actual spar configuration and its finite element representation.

Fig. 13. Boundary condition for test box element model.

3.3. Test panel models

In this section the modelling techniques which were used for the test panel shell and beam elements, and for the connection between the test panel and the test box are given.

In order to facilitate the comparison between the strain distributions of the stabilizer and the test panels, the element sizes in stringer direction for the panel finite element model were copied from the finite element model of the stabilizer.

The finite element model of the Lower-Aft panel contained 270 nodes, 226 shell elements and 99 beam elements. The finite element model for the connection between the test panel and the test box contained 54 shell elements and 92 beam elements. The finite element models for the other test panels and their connection to the box contained a similar number of nodes and elements.

3.3.1. Panel shell elements

The skin material of the panels is modelled in 4-node shell elements. The shell elements in the finite element model of the Lower-Aft panel are shown in Fig. 14. The distribution of the various material properties is indicated.

The finite element model of the panel is placed on the top plane of the finite element model of the test box. The distance between the reference plane of the panel shell elements and the actual mould surface of the panel was taken into account by using an offset for the plate elements.

As first and as last ply in the finite element model a 0.001 mm thick ply was added with a ply orientation in the direction of the stringer, to facilitate the determination of surface strains in the stringer direction and perpendicular to the stringer direction for post-processing purposes.
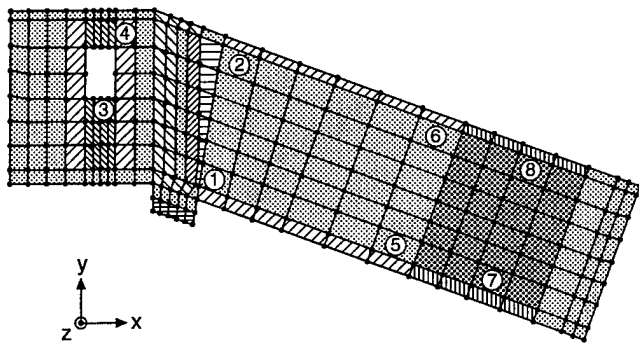
Fig. 14. Finite element model of Lower Aft panel, different fill patterns indicate different material properties, numbers indicate elements used in actuator load determination.

3.3.2. Panel beam elements

As in the composite horizontal stabilizer finite element model, the panel stringers are modelled using beam elements. The beam elements in the finite element model of the Lower-Aft panel are shown in Fig. 15.

The stringers are placed on the skin. As in the stabilizer finite element model, the shear centre of the beam elements is located at the interface between skin and stringer. The offset of the beam elements, which is given in the global coordinate system, is therefore the offset of the skin minus the local thickness of the skin.

The location of the neutral axis of the stringer is specified relative to this offset point. The stringer is furthermore characterized by its cross sectional area, and moments of inertia in two directions. A Young's modulus and a shear modulus are given for the stringer material.

3.3.3. Finite element model of the connection between the test panels and the metal test box

The panels are connected to the metal test box by aluminium angle sections.

An overview of the finite element model of the connection is given in Fig. 16. The aluminium angle sections connecting the panel and the rib simulations are modelled by 4-node shell elements. The aluminium
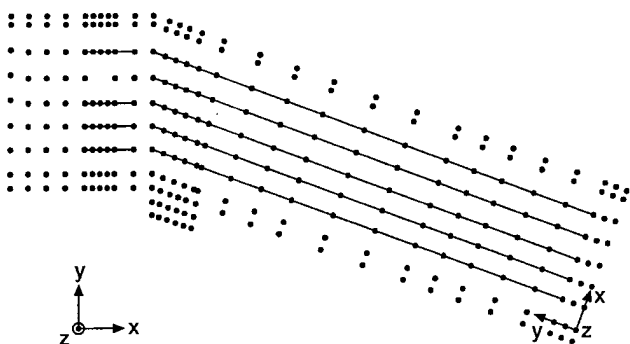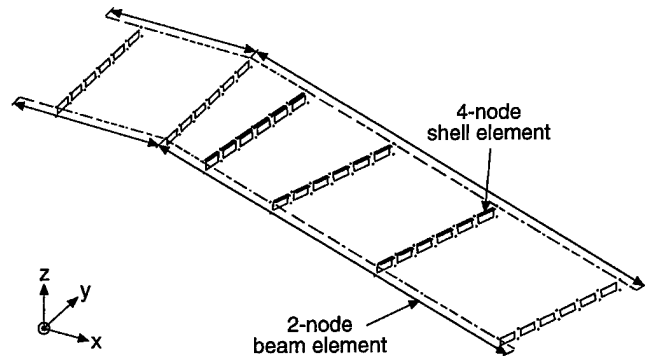

Fig. 16. Finite element model of the connection between panel and test box.

angle sections connecting the panel and the spar simulations are modelled by 2-node beam elements.

The connection between the finite element model of the panel and the finite element model of the spar simulations is shown schematically in Fig. 17. The construction of connecting beam elements was necessary because the test box and the panel finite element models are not compatible, which resulted in the finite element models having only incidentally common nodes. All nodes which are connected, are situated at the line along the top of the spar simulation. The beam elements connect all panel nodes on this line and those spar simulation nodes on this line which are located in between two slits.

4. Determination of actuator forces

The configuration of the test panels is based on the configuration upper and lower skins of the composite horizontal stabilizer. The loading conditions of the test panels should result in similar strain conditions as computed by finite element analyses for the composite horizontal stabilizer skins. To achieve this, a combination of actuator forces had to be determined which

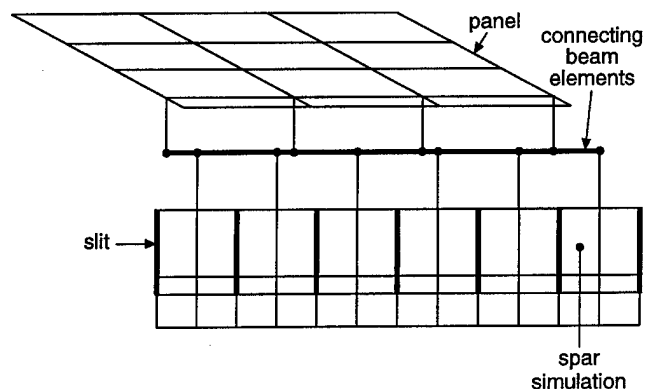Fig. 15. Beam elements for Lower Aft panel.

Fig. 17. Exploded view of connection between panel and spar simulation finite element models.

gave an optimum correspondence between strains in the stabilizer skins and strains in the test panels.

4.1. Methodology

The strain distribution in the composite horizontal stabilizer was determined for a number of critical load cases, representing extreme loading conditions, using finite element analysis. Also, a finite element analysis of the test set-up was performed, in which the contribution of the six actuators to the strain distribution in the test panels was determined individually.

The optimum combination of actuator loads was determined by least square minimization of the difference between test panel and stabilizer strains in the skin for a number of relevant elements, using the maximum load of the actuators as constraints. The selected relevant elements for the Lower-Aft panel are indicated in Fig. 14.

The correspondence of the normal strains in stringer direction was deemed more important than the correspondence of the shear strains, and the correspondence of strains at one location was considered more important than at another location. For instance, the correspondence of the strains directly outboard of rib 2 (locations 1 and 2 in Fig. 14) was deemed more important than at the centre section (locations 3 and 4 in Fig. 14).

Moreover, it should be noted that in the test set-up strains perpendicular to the stringer direction cannot be induced independently: strains in this direction occur only as a result of Poisson's contraction. In the stabilizer, the loads perpendicular to the stringer direction are found. Strains perpendicular to the stringer direction were therefore not taken into account in the determination of the actuator forces.

4.2. Results

The individual actuator load contributions to the strains in the Lower-Aft panel are given in Fig. 18. The location numbers refer to the elements as indicated in Fig. 14. The values given pertain to a load per actuator of 10 kN.

Most salient is the large difference in contribution of F_{z1}, F_{z2} and F_{z3} on the one hand and F_{y1}, F_{z5} and F_{z6} on the other. The contributions of the former are more than ten times larger than that of the latter. In this respect, it should be noted that the actuators F_{z5} and F_{z6} are positioned quite close to the support, and that most of the load of actuator F_{y1} is carried by the bottom of the metal test box.

The contributions of the various actuators to the strain distribution in the other test panels was very similar to that of the Lower-Aft panel.

The strain in stringer direction for a particular load case is shown in Fig. 19(a) for the finite element model of the lower skin as part of the composite horizontal stabilizer. The strain in stringer direction of the Lower-Aft test panel for this load case, as obtained using the optimum combination of actuator loads, is given in Fig. 19(b). As can be seen, the correspondence of composite horizontal stabilizer and test panel strains is quite good.

It was established that with the given actuator configuration it was possible to generate a wide range of normal and shear strain distributions in the test panels. Ultimately, for all panels and all load cases (21 different loading conditions in total) a satisfactory combination of actuator loads was established.

5. The test programme

Four different test panel configurations were tested (see Fig. 1): Lower Aft, Lower Front, Upper Aft and Upper Front. The test panels were tested at ambient conditions. All panels were statically tested up to at least 2.05 × Limit Load (an environmental knock down
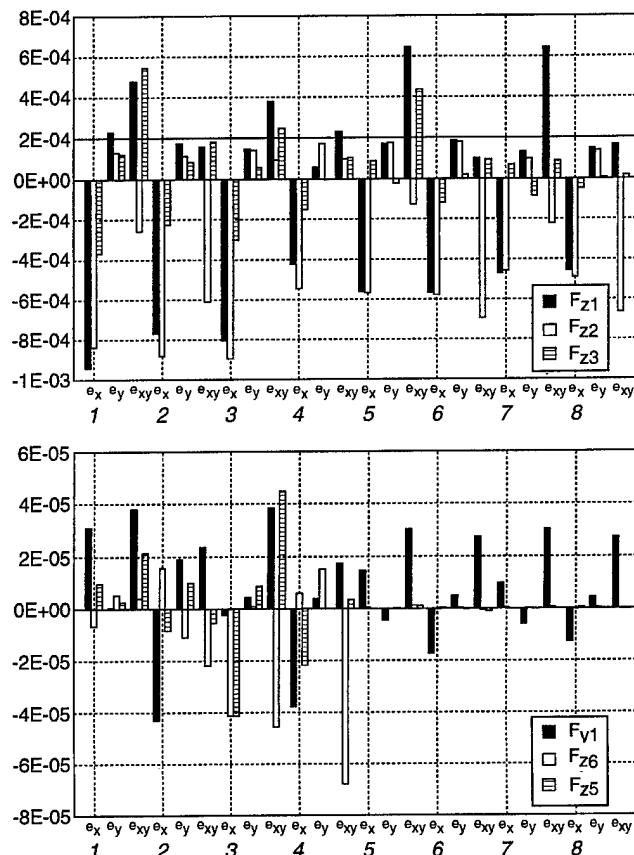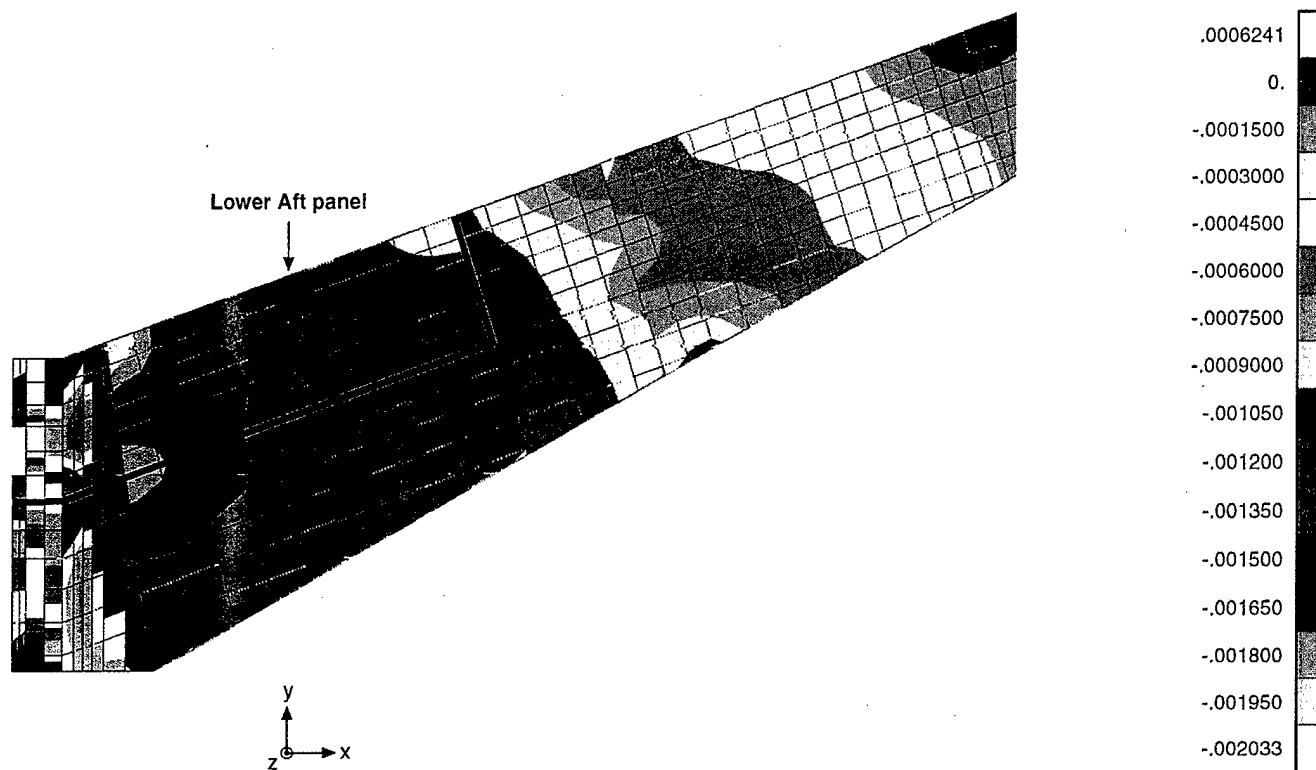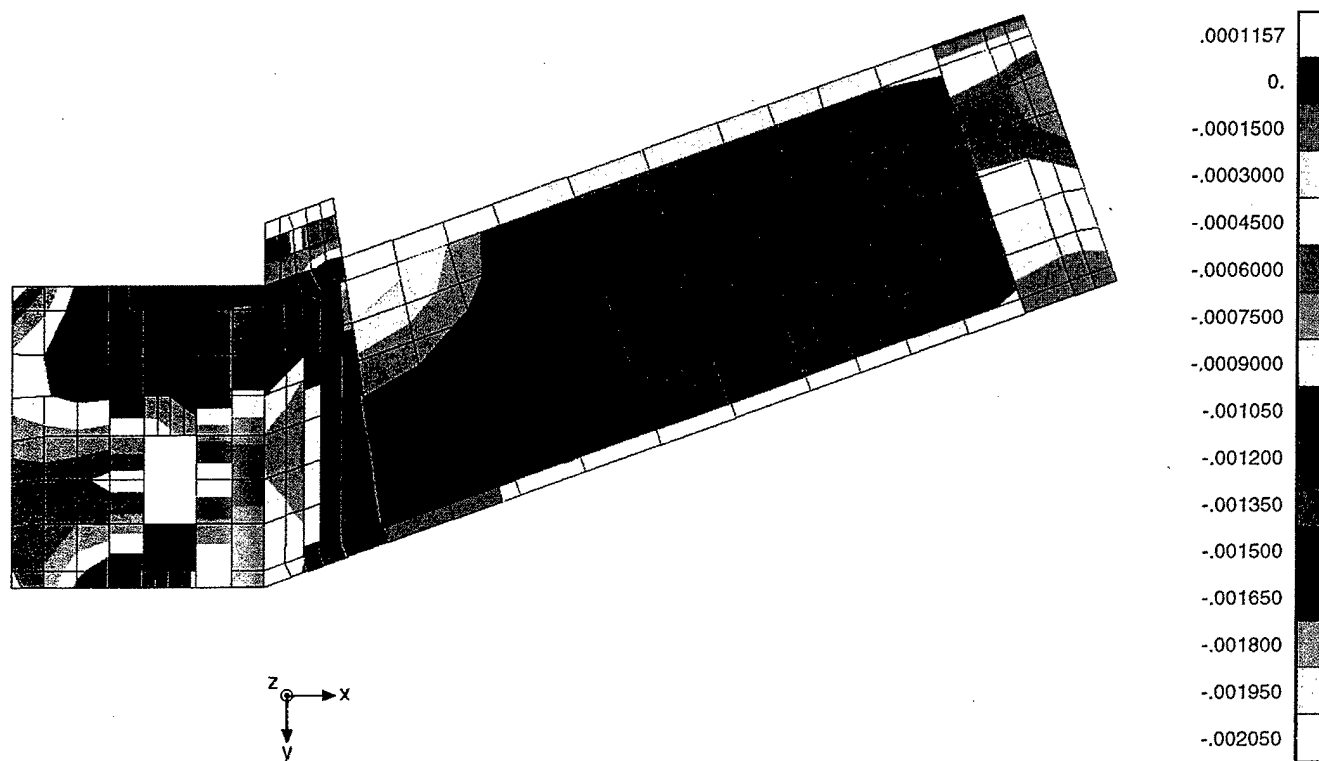

Fig. 18. Contributions of actuators to the strain distribution for Lower Aft panel.

a) *Stabilizer lower skin*

b) *Lower Aft panel*

Fig. 19. Strain in stringer direction.

factor of 1.35 was used to compensate for the fact that the tests were carried out at ambient conditions).

Six different panels were tested on a single metal test box. The panels were loaded up to a maximum of 3.0 times Limit Load with a total of 21 different loading conditions.

Several load cases (both symmetric and asymmetric) were applied to each panel. Loads were applied in discrete loads steps. After each load step the applied loads, the deformation and the strains were recorded.

5.1. Panel instrumentation

The panel instrumentation comprised Linear Variable Displacement Transducers (LVDTs), internal displacement transducers in the actuators, strain gauge rosettes and single strain gauges.

The instrumentation plan of the lower-front panel is shown in Fig. 20. The strain gauge rosettes were mainly applied in pairs, one on the outside side [Fig. 20(a)] and one on the stringer side of the panel [Fig. 20(b)]. A number of single strain gauges was applied in a similar manner.

Single strain gauges were used to obtain information with regard to the strain distribution in a stringer cross section. The location of the strain gauges on the stringer cross section is shown in cross section A–A in Fig. 20(c). The direction of the three rosette strain gauges a, b, and c are perpendicular to the stringers, under an angle of 45° and parallel with the stringers, respectively.

6. Comparison of experimental and finite element calculation results

The experimental results were compared to the finite element results which were obtained for actual loading conditions.

In the discussion of the results, the load is expressed in a non-dimensional form by *J*, the load factor. For the Design Limit Load the load factor is equal to 1, for Design Ultimate Load the load factor is equal to 1.5. The experimental results and the finite element results are divided by the load factor *J*. In this way the non-linearity of the strains with increasing load is readily visualized, and a single curve suffices to show the corresponding finite element results.

6.1. Processing and presentation of strains

The strain gauge results can be grouped in such a way that the strain distribution along a line on the test panel is shown. As an example, the results for the Lower-Front panel along two lines are presented:

— Line 1 parallel to the rear spar simulation and located in between the doubler and the first stringer near the rear spar. At this line 6 pairs of strain gauge rosettes and 1 pair of single strain gauges (inside and outside) are located.
— Line 2 along the second stringer at the front side of the panel. At this line, 3 stringer strain gauge combinations are located.
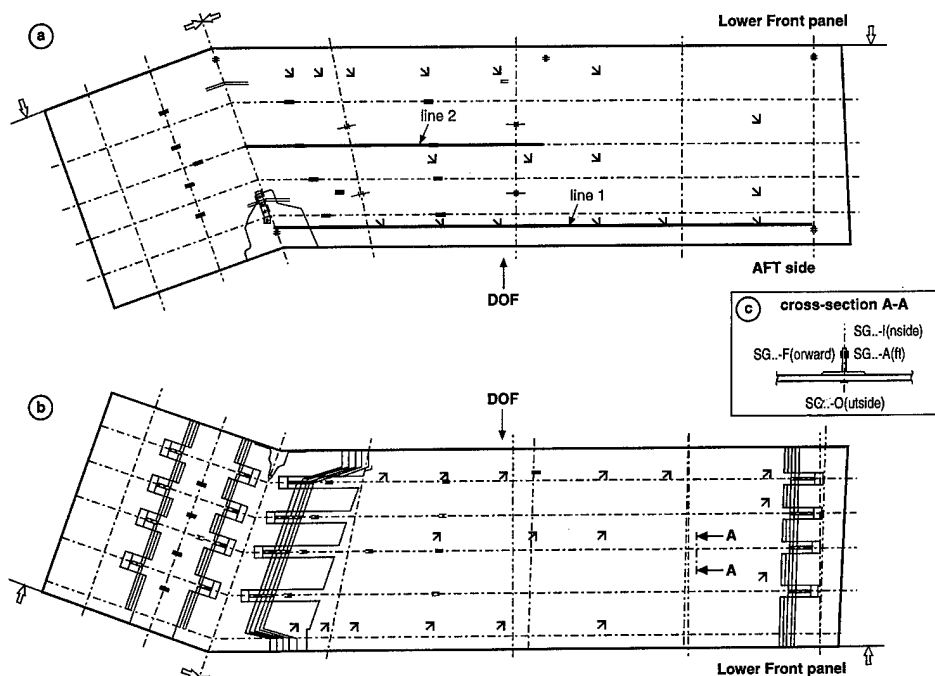

Fig. 20. Instrumentation plan of Lower Front panel.

For each line the strain gauge results are presented as a function of the distance along the line.

The strains in the shell elements are the strains as calculated for the first and last layers in the stacking sequence of an element. These layers were 0.001 mm thick dummy layers with a fibre direction parallel to the stringer direction. Strains are evaluated in the centre of each element. The curve showing the finite element results simply connects these results. It should be kept in mind that inboard of rib 2 the differences between the strains of the elements are attributable mainly to the difference in material thickness, which was a more or less stepwise increase.

The strains for a pair of rosettes are presented as average and bending strains in stringer direction ε_x, perpendicular to the stringer direction ε_y, and the corresponding shear strain ε_{xy}. The average and bending strains ε^{avg} and ε^{bend} were calculated from the strains on the inside (ε^i) and the outside (ε^o) of the test panel, using:

$$\varepsilon^{avg} = \frac{\varepsilon^i + \varepsilon^o}{2}, \quad \varepsilon^{bend} = \frac{\varepsilon^i - \varepsilon^o}{2}. \tag{1}$$
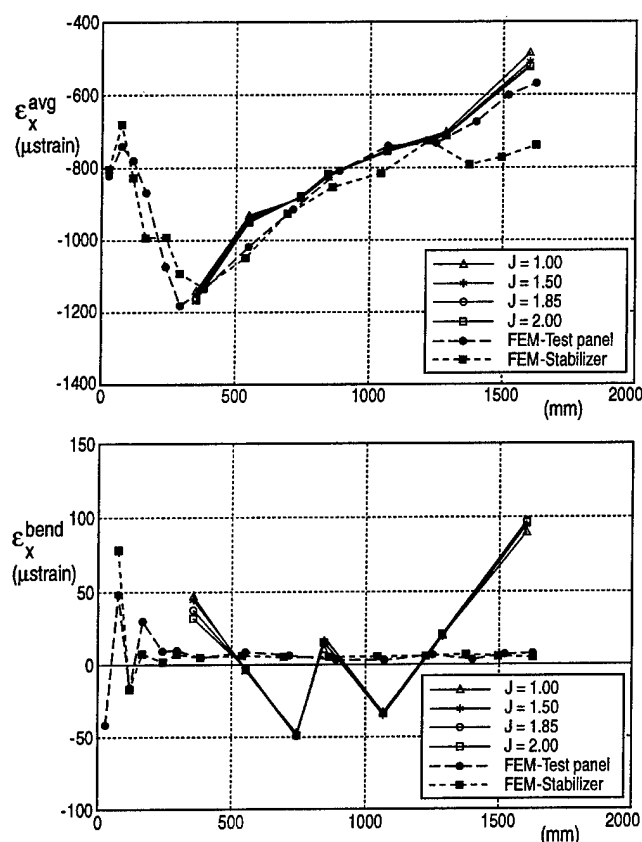
The shear strain for one rosette was first calculated from the rosette strains using

$$\varepsilon_{xy} = \varepsilon_b - \frac{\varepsilon_a + \varepsilon_c}{2} \tag{2}$$

in which ε_a, ε_b and ε_c are the strains in the three rosette strain gauges. The average and twisting shear strains for the pair of rosettes were calculated subsequently.

The stringer deformations comprised the strain at the neutral axis ε_{na}, and the curvatures with respect to the local coordinate system ϕ_y and ϕ_z. The stringer deformations were computed directly from element forces and moments of the stringers, using:

$$\varepsilon_{na} = \frac{N}{E \cdot A}, \quad \phi_z = \frac{M_1}{E \cdot I_1}, \quad \phi_y \frac{M_2}{E \cdot I_2} \tag{3}$$

in which E is the Young's modulus of the stringer material, which was computed using the stringer lay-up

a) *Scaled average strains perpendicular to the stringer direction ε_y^{avg}*
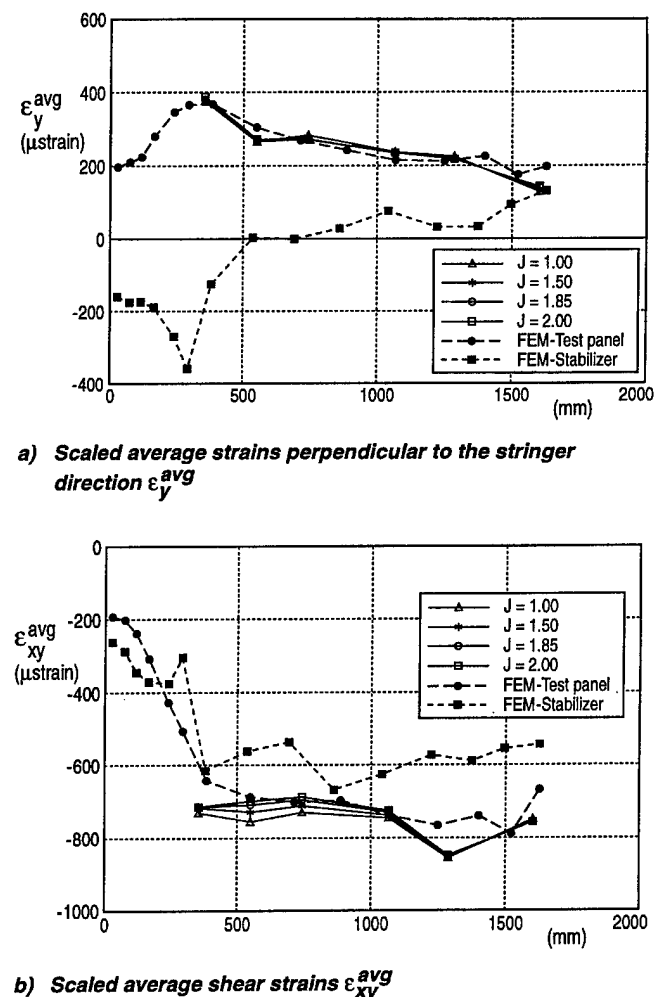

b) *Scaled average shear strains ε_{xy}^{avg}*

Fig. 22. Comparison of experimental and calculated scaled average strains.

Fig. 21. Comparison of experimental and calculated scaled average and bending strains in stringer direction ε_x^{avg} and ε_x^{bend} (J = load factor).

little correspondence with the experimental ε_x^{bend}

As can be seen, the correspondence between the results for finite element models of the composite horizontal stabilizer and the panel test set-up is quite good.

The scaled average strain perpendicular to the stringer direction ε_y^{avg} and the average shear strains ε_{xy}^{avg} are given in Fig. 22.

The experimental ε_y^{avg} and ε_{xy}^{avg} both compare quite well with the calculated strains for the finite element model of the panel test set-up.

The results for the stress component ε_y^{avg} for the finite element models of the composite horizontal stabilizer and for the panel test set-up are different. As was mentioned in Section 4.1 strains perpendicular to the stringer direction cannot be induced independently in the test panels, and were therefore not taken into
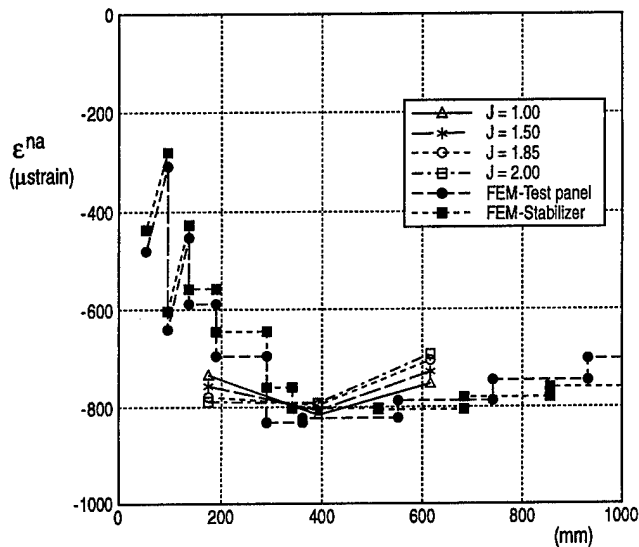

Fig. 23. Comparison of experimental and calculated scaled strain at the neutral axis of the stringer ε^{na}.

and the ply elasticity parameters. The x-axis in the stringer coordinate system is oriented along the stringer axis, the z-axis is normal to the skin surface, and the y-axis completes an orthogonal x, y, z coordinate system.

The strain ε at any location in the beam can be calculated from the stringer deformations ε_{na}, ϕ_y and ϕ_z using:

$$\varepsilon = \varepsilon_{na} - \phi_z \cdot (y - y_{na}) - \phi_y \cdot (z - z_{na}) \quad (4)$$

in which y and z indicate the position, at which the strain is calculated, and y_{na} and z_{na} indicate the position of the neutral axis of the beam. These coordinates are given in the beam element coordinate frame. For each beam element the strains are given for both nodal points. Therefore two results are given for each node, resulting in a jagged appearance of the curves.

The strains obtained with the strain gauges were also converted to stringer deformations ε_{na}, ϕ_y and ϕ_z.

6.2. Comparison of results

The experimental results are shown for a number of load factors.

The finite element results for the test panel and for the composite horizontal stabilizer are also indicated.

6.2.1. Strain comparison for skin

The scaled average and bending strains in stringer direction between the doubler and the stringer near the rear spar ε_x^{avg} and ε_x^{bend}, for the strain gauges along line 1 are shown in Fig. 21. The experimental ε_x^{avg} strains compares quite well with the calculated strains for the finite element model of the panel test set-up. The calculated ε_x^{bend} strains are negligible, however there is
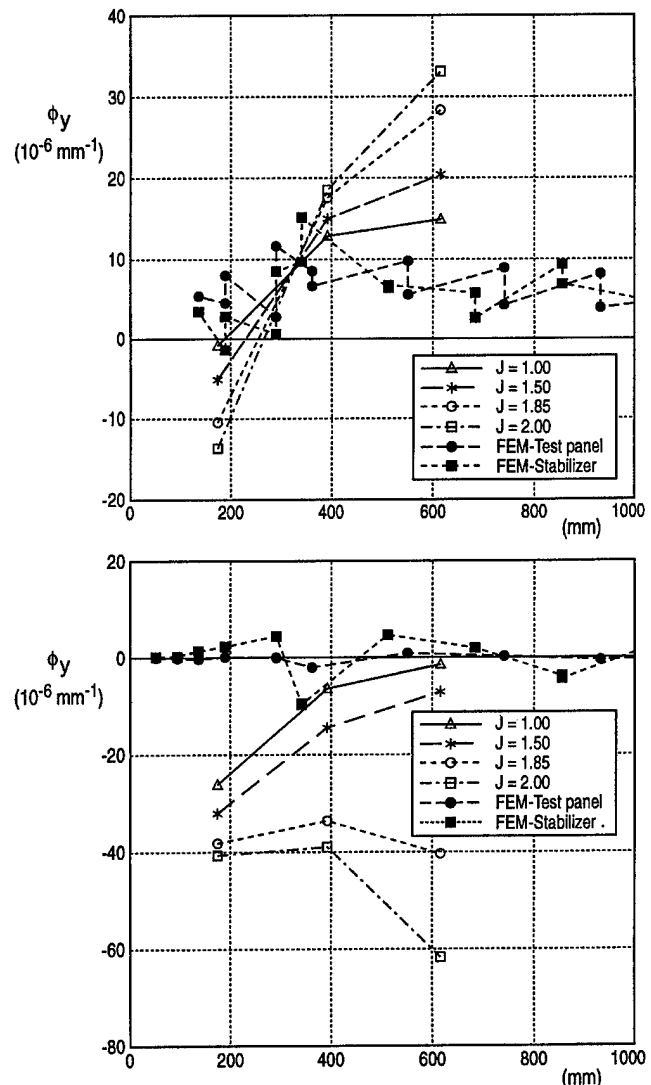

Fig. 24. Comparison of experimental and calculated scaled strain curvatures ϕ_y and ϕ_z.

account in the actuator load optimization. The results for the strain component ε_{xy}^{avg} match for some elements but are quite different in between.

6.2.2. Strain comparison for stringer

The scaled strain at the neutral axis of the stringer ε_{na} and the scaled curvatures ϕ_y and ϕ_z along the second stringer at the front side of the panel are shown in Fig. 23 and Fig. 24.

The experimental ε_{na} compare quite well with the calculated strains for the finite element model of the panel test set-up. The experimental and calculated ϕ_y and ϕ_z are rather different.

Again, the correspondence between the results for finite element models of the composite horizontal stabilizer and the panel test set-up is quite good.

6.3. Discussion

The calculated ε_x^{avg}, ε_y^{avg} and ε_{xy}^{avg}, as well as ε_{na} compare quite well overall with the experimental values.

The experimental bending and twisting behaviour of the skin and the stringers was found to be quite different from the calculated values. It should be noted that all nodes in the panel finite element model are connected to the shell elements, which model the skin, and to the beam elements, which model the stringers. This means that the deformation of the shell and beam elements of the panel is completely interdependent both in bending and extension. The magnitude of the calculated scaled bending strains perpendicular to the stringer direction ε_y^{bend} and of the calculated scaled twisting shear strain ε_{xy}^{twist} is quite small. The deformation of the skin in between two stringers, which is characterized by a quasi-symmetry condition at each

stringer, can not be described within a single 4-node element.

The calculated distribution of ε_x^{avg} and ε_{xy}^{avg} for the composite horizontal stabilizer and the panel test set-up finite element models compared quite well, the distribution of ε_y^{avg} was different for each model. For both models the magnitudes of the bending and twisting strains were limited.

7. Conclusions

Six different panels were tested on a single metal test box. The panels were loaded up to a maximum of 3.0 times Limit Load with a total of 21 different loading conditions without incurring any damage to the metal test box.

The experimental average strains and the average strains calculated for the panel test set-up compared quite well in most cases.

The experimental bending and twisting strains were different from the bending and twisting strains calculated for the panel test set-up.

The calculated distribution of ε_x^{avg} and ε_{xy}^{avg} for the composite horizontal stabilizer and the panel test set-up finite element models compared quite well, the distribution of ε_y^{avg} was different for each model. For both models the magnitudes of the bending and twisting strains were limited.

Reference

[1] Rouchon J. Certification of large airplane composite structures, recent progress and new trends in compliance philosophy. ICAS-90-1.8.1, 1990.

COMPOSITE
STRUCTURES

Single-bolt tension joint tests on pultruded GRP plate — effects of tension direction relative to pultrusion direction

G. J. Turvey*

Engineering Department, Lancaster University, Bailrigg, Lancaster LA1 4YR, UK

Abstract

The literature on single-bolt tension joints in structural grade pultruded GRP plate is reviewed and the differences between the main investigations are highlighted. Details are given of the test setup and the joint configurations used in a series 54 such tests on single-bolt joints in which the angle between the pultrusion and tension axes (the off-axis angle) and the joint geometry are varied. Ultimate strength, intial stiffness, initial bolt slip and bolt displacement at failure data are presented as functions of the joints' principal geometric ratios. The observed joint failure modes show that, for off-axis angles $\geq 30°$, bearing failure (a relatively benign failure mode) does not arise. Instead, tension mode failure predominates and cracks tend to propagate parallel to the rovings diagonally across the width of the joint. It is concluded that the rovings play a significant role in controlling the crack propagation and this has implications for joint layout and design in pultruded GRP plate. © 1998 Published by Elsevier Science Ltd. All rights reserved.

Notation

D	Bolt diameter
E	End distance
E_L	Longitudinal modulus
E_T	Transverse modulus
P	Tensile load on joint
t	Plate thickness
W	Plate width
α	Angle between the pultrusion and tension axes
ν_{LT}	Major Poisson's ratio

1. Introduction

There is growing evidence that fibre-reinforced polymer composite materials are beginning to be taken seriously as viable materials from which civil engineering structures may be fabricated. These structures generally fulfil a secondary load-bearing function, e.g. walkways and lightly loaded raised platforms in aggressive environments found in the water, sewage and chemical process industries. Sometimes, however, the structures fulfil a primary load-bearing role. Outstanding examples of the latter are the cable-stayed footbridges at Aberfeldy and Kolding in Scotland and Denmark respectively. The former bridge makes extensive use of GRP (Glass Reinforced Plastic) pultruded components and the latter consists almost entirely of such components. The bridges contrast sharply in respect of the pultruded GRP components and the methods used to connect them. The Aberfeldy footbridge is based on customised pultruded shapes with interlocking joints which are also adhesively bonded, whereas the Kolding footbridge utilises a standardised range of shapes and bolted joints. In order to prove the design concepts of both bridges their designers have had to rely on data derived from extensive testing of components and joints. Full details of these test programmes are not yet in the public domain. In-service monitoring programmes have been set up for both bridges in order to establish how well they perform with the passage of time. Of particular interest and concern is the behaviour of joints, because they are often the weakest part of the structure and also because there is a lack of data on the long-term behaviour of joints. There is, therefore, a pressing need to generate data on both their short and long-term behaviour in order to engender confidence in structures made of pultruded GRP components. Recogni-

*Corresponding author. Tel.: +44-1524-593088; Fax: +44-1524-381707; E-mail: g.turvey@lancs.ac.uk

tion of this need has provided the motivation for the single-bolt tension joint tests reported here, which contribute to the developing database on joint behaviour.

Test data on bolted joints in pultruded GRP materials have been accumulating gradually over the past few years, but remain far from adequate. It appears that Rosner and Rizkalla [1] were the first to publish data derived from single-bolt tension joint tests. They carried out a series of tests, for one bolt size (a 19 mm diameter steel bolt torqued to 32.5 Nm), on three thicknesses (9.5, 12.7 and 19.1 mm) of EXTREN™ 500 Series pultruded GRP plate* — a structural grade material. Data from this kind of test are regarded as essential to the formulation of simple procedures for the design of joints. Rosner and Rizkalla [1] also developed simple design formulae for single-bolt tension joints. The formulae utilise empirically determined coefficients, which are based on assumptions first advanced by Hart-Smith [2]. Unfortunately, the coefficients have to be determined for each plate thickness. Abd-El-Naby and Hollaway [3] have also carried out tests on single-bolt tension joints in pultruded plate material. They appear to have used customised pultruded plate material and, therefore, their tests, whilst providing information on the failure strengths and modes, do not add to the design database for structural grade material. Erki [4] too conducted tests on single-bolt joints in EXTREN™ pultruded GRP plate. The tests, which utilised a double lap configuration, were designed to quantify the effects of different bolt types, i.e. steel vs pultruded GRP bolts, on joint strength. The majority of the tests were tension joint tests, but in a few instances the joints were subjected to compression and provided the first published data on failure for this mode of loading. Recently, Cooper and Turvey [5] presented data derived from 81 tests on single-bolt tension joints in EXTREN™ 500 Series plate. These tests were conducted on 6.4 mm thick plate and, therefore, complement Rosner and Rizkalla's [1] and Erki's [4] data. Cooper and Turvey's tests [5] were noteworthy, because they quantified the effect of bolt torque on joint strength and showed that, when bearing failure occurred, the strength increased as the bolt torque increased. However, they took the view that the strength gain could not be relied upon in the long-term, due to creep and viscoelastic effects, and, therefore, they recommended that design should be based on finger-tight (defined as a torque of 3 Nm) ultimate strengths. This study also showed that when bearing was the mode of joint failure, its onset could be detected as a change in the slope of the load–extension

curve. The load at which this effect occurred they defined as the *damage* load and suggested that it could be used as a design load for the bearing failure mode. The test data were subjected to statistical analysis and failure loads were determined with prescribed confidence limits. In addition, critical E/D (end distance/bolt diameter) and W/D (plate width/bolt diameter) ratios were defined, below which the failure mode was other than in bearing. In a further investigation, Turvey and Cooper [6] carried out a series of tests on single-bolt tension joints in pultruded GRP material cut from the webs and flanges of 102x102x6.4 and 203x203x9.5 (all dimensions in mm) EXTREN™ 500 Series WF (Wide Flange) sections. The tests were carried out with the bolts in the finger-tight condition; 10 and 12 mm diameter bolts were used in the smaller and larger thickness material respectively. Again critical E/D and W/D values were established for the bearing failure mode and design load capacities were quantified with prescribed confidence limits. In both [5] and [6] stiffness data were also presented, because it could be important in some situations, especially where the structure is governed by serviceability rather than ultimate strength criteria.

In a recent investigation, Yuan et al. [7] explored the effect of hole clearance on the bearing failure of single-bolt tension joints in EXTREN™ 500 Series pultruded GRP plate of thickness 6.4 mm. They established that the joint strength reduced as the hole clearance increased. The only other single-bolt tension joint tests conducted on pultruded GRP plate material known to the author are those reported by Sotiropoulos et al. [8]. The plate material was cut from WF-section and a pultruded cellular plank with thicknesses of 6 and 4.8 mm respectively. The joints were tested in the double lap configuration in two arrangements. In the first arrangement the inner plate was pultruded GRP and the outer plates were steel and in the second the material order was reversed. Two types of mechanical fastener were used: a 12.7 mm diameter stainless steel bolt (torqued to 30 Nm) in a 13.5 mm diameter hole and a sleeved bolt. The E/D ratio was varied from 2 to 6 for two W/D ratios (4 and 6). The majority of these tests were performed with coincident tension and pultrusion axes. The remaining tests were conducted with the pultrusion axis at 90° to the tension axis. The test results reported in Ref. [8] are presented as graphs of joint efficiency. The pultruded plate material and joint strengths are not reported in the paper and this is unfortunate, especially as the efficiency data may be misinterpreted. For example, single-bolt tension joints with the pultrusion axis oriented at 90° to the tension axis are shown to have efficiencies about 10% higher than those with the pultrusion axis aligned with the tension axis. These superior efficiencies are, however, offset by the fact

*In this paper reference to the trade name of a pultruded GRP product does not imply any endorsement of it whatsoever.

that the former joint strengths are substantially lower, which is generally of over-riding importance from the design standpoint.

It is of interest to note that in the majority of the several hundred single-bolt tension joint tests, outlined above, the tension axis was aligned parallel or normal to the pultrusion axis. Only Rosner and Rizkalla [1] and Erki [4] have reported test data for any other angle between the tension and pultrusion axes. They carried out a number of tests with an angle of 45°. These tests used the thicker range of EXTREN™ plate, referred to earlier. The present paper focuses on the presentation of test data for finger-tight single-bolt tension joints in 6.4 mm thick EXTREN™ 500 Series pultruded GRP plate with three off-axis angles, $\alpha = 90°$, 45° and 30°, between the pultrusion and tension axes (see Fig. 1 for the definition of the angle, α) for a range of E/D and W/D ratios.

2. Pultruded GRP plate properties

The composite material, EXTREN™ 500 Series 6.4 mm thick flat plate, used in the single-bolt tension joint tests reported here, is made by the pultrusion process [9]. The reinforcement is in two forms, viz. E-glass rovings (uni-directional fibre bundles) and CFM (Continuous Filament Mat). The rovings provide the stiffness and strength in the longitudinal (pultrusion) direction and the CFM provides the transverse stiffness and strength, both of which are much lower (typically about one half, depending on the fibre volume percentage) than the longitudinal values. The fibre architecture of the plate material is exposed in Plate. 1, which shows a piece of EXTREN™ plate after the resin has been burned-off and the individual roving and CFM layers have been separated. An estimate of the glass fibre volume percentage in the pultruded
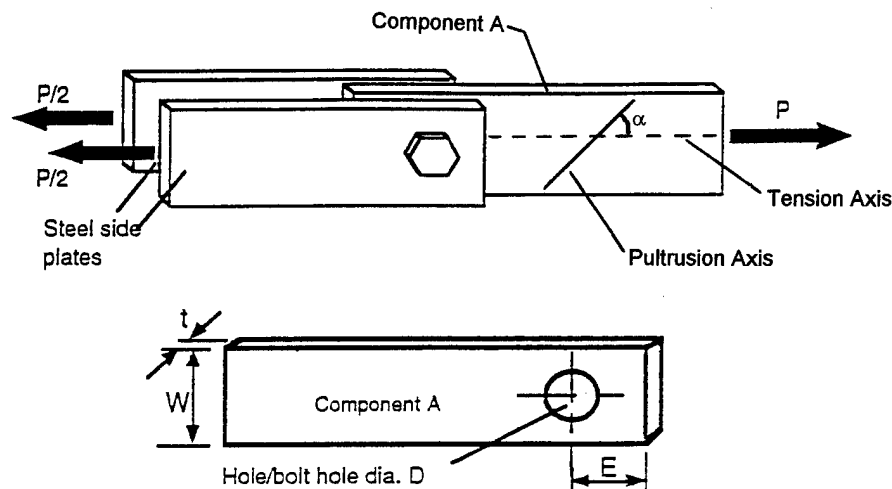

Fig. 1. Double lap single-bolt tension joint showing the basic geometric parameters and the angle, α, between the pultrusion and tension axes.
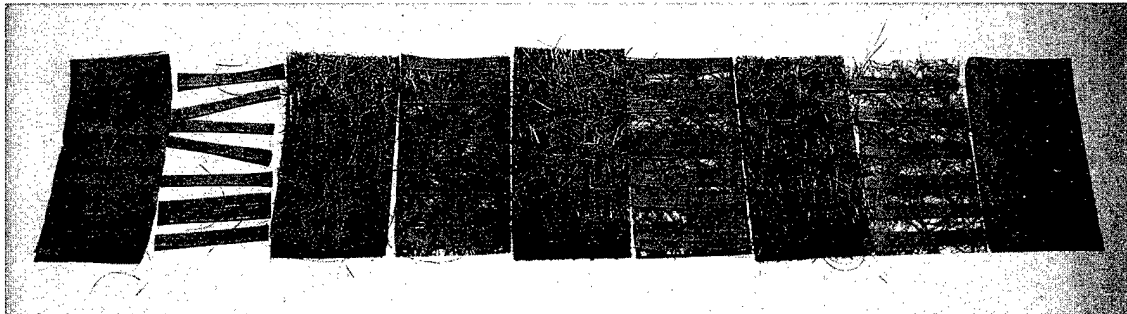

Plate 1. Exposed fibre architecture of EXTREN™ 500 Series 6.4 mm thick pultruded GRP plate after resin burn-off and separation of the roving and CFM layers. The left and right most layers are the lighter weight upper and lower surface veils.
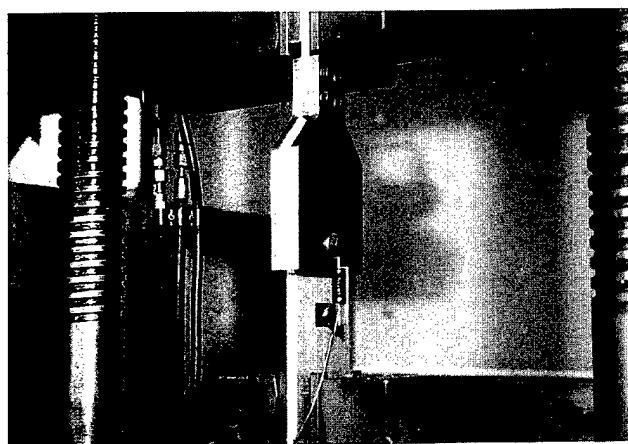
Plate 2. Single-bolt tension joint ready for test in the Amsler Universal Tesing Machine.

plate may also be obtained from the burn-off test. The test results indicate that the fibre volume percentage is between 35 and 40%. The left and rightmost layers shown in Plate 1, are the upper and lower surface veils, which are similar to the CFM but have a much lower mass per unit area. The function of the veils is to provide resin-rich surfaces, so that the plate material may be handled easily and safely. The matrix material, which surrounds and stabilises the rovings and CFM and also provides the load transfer mechanism between individual fibres, is a polyester resin; its volume percentage is typically about 55–60%. The remaining volume is occupied by an inert filler material, e.g. calcium carbonate, and is included in order to economise on the use of polyester resin.

The elastic moduli and strengths (parallel and normal to the pultrusion direction) of the EXTREN™ 500 Series plate given by the manufacturer [10] are minimum values and are reproduced in Table 1.

Table 1
Elastic moduli of EXTREN™ 500 Series 6.4 mm thick pultruded GRP plate

Longitudinal tension modulus E_L (kN/mm²)	Transverse tension modulus E_T (kN/mm²)	Major Poisson's ratio v_{LT}	Data source
12.4	6.2	0.31	MMFG design manual [9]*
15.9–17.1	8.4	0.31	Present tests on unwaisted coupons without end tabs [195 and 250x25x6.4 mm with 50 mm grip lengths]

*The values quoted are *minimum* values.

Moduli and strength values obtained from tests on tension coupons carried out in the Engineering Department's laboratories are also given in Table 1 for comparison. These values are, as expected, somewhat higher than the manufacturer's values.

3. Bolted joint test rig

It is evident from the literature on double lap single-bolt tension joint tests in pultruded GRP material that a variety of test configurations have been used. Rosner and Rizkalla [1] used outer GRP plates and a steel inner plate and, therefore, effectively conducted two nominally identical single-bolt tension tests simultaneously. Erki [4] used both inner and outer pultruded GRP plates. The majority of tests conducted by Abd-El-Naby and Hollaway [3] and all of the tests conducted by Cooper and Turvey [5] and Turvey and Cooper [6] used steel outer plates and a pultruded GRP inner plate. Sotiropoulos et al. [8] carried out tests with both types of steel/pultruded GRP plate arrangement.

The test configurations also exhibit other differences, particularly with respect to the steel plate/pultruded GRP plate contact areas and the location and number of extensometers. In one test configuration [3], in which the inner plate was pultruded GRP, additional washers were used to separate the steel and pultruded GRP plates and, therefore, reduce the contact area, whereas in others [5,6,8] steel plate/GRP plate contact existed across the full width and length of the joint. In the former configuration a confinement pressure would have existed close to the edge of the hole in the GRP plate, but beyond the outer circumference of the washers it would have been zero, whereas in the latter configuration the confinement pressure would have extended over a greater area. Which configuration is more representative of practical joints has not yet been resolved. Indeed, this may not even be relevant, because such tests are mainly used to generate basic data for the development of simple design procedures for practical joints, many of which involve multi-bolt layouts. The number and location of extensometers used by different researchers also varies. Abd-El-Naby and Hollaway [3] and Erki [4] used two extensometers, whereas Cooper and Turvey [5] and Turvey and Cooper [6] used a single extensometer. Erki [4] used the extensometers to measure extension across the joint, whereas Abd-El-Naby and Holloway [3] and Cooper and Turvey [5] and Turvey and Cooper [6] measured extensions relative to the bolt. In other tests [8] extensions were not reported.

For the work reported here the test set-up used in Refs. [5,6] was adopted. Plate 2 shows a joint ready for testing and Fig. 2 provides further details of the fixture.
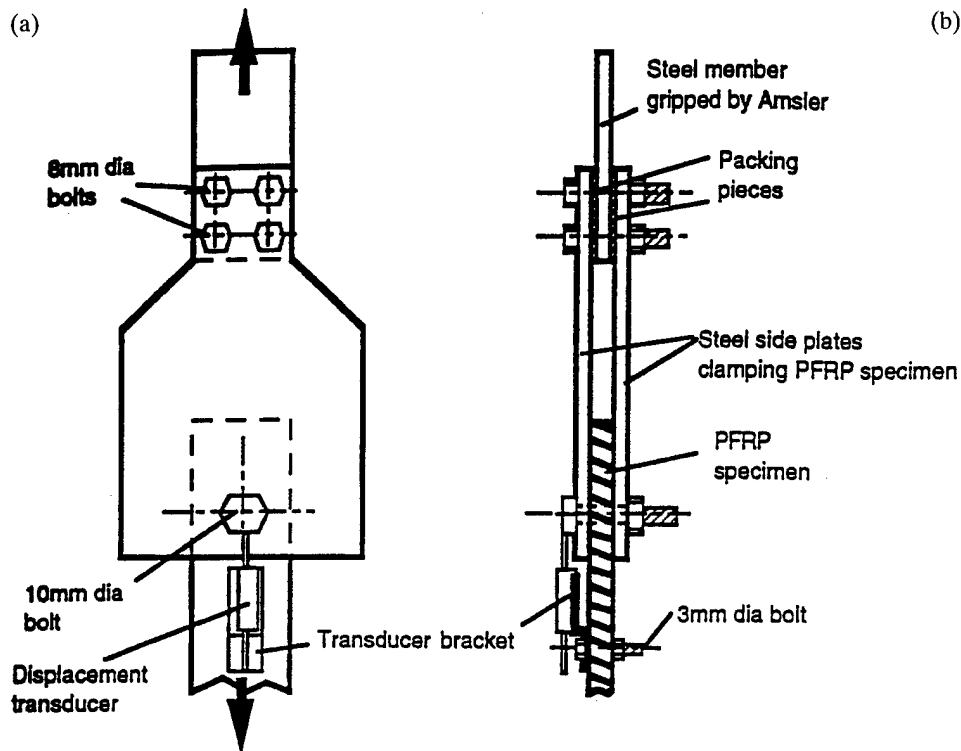
Fig. 2. Details of the single-bolt tension test fixture: (a) front elevation and (b) side elevation.

4. Bolted joint details and test procedure

As pointed out in the review of single-bolt tension joint tests, there is very little data on tests in which the pultrusion and tension axes do not coincide and such off-axis data as exists is mainly for the case in which the axes are at 90° to one another. Therefore, it was decided to undertake a series of bolted joint tests on EXTREN™ 500 Series 6.4 mm thick pultruded GRP plate in which the angle, α, between the tension and pultrusion axes was 90°, 45° and 30°. The data from these tests may then be combined with the 0° data given in [5] to provide a reasonably comprehensive data set from which to assess the effects of off-axis loading on the strength of double lap single-bolt tension joints.

It is well-known, from 0° tests conducted on 6.4 mm thick plate [5], that the joint strength and failure mode are dependent on the joint geometry and the bolt torque. The joint geometry is characterised in terms of the E/D and W/D ratios. Therefore, it was decided to carry out tests for a range of these ratios, i.e. $3 \le E/D \le 6$ and $4 \le W/D \le 10$. Furthermore, in order to make use of and extend the test data reported in [5], the present joints also used mild steel bolts 10 mm in diameter. Holes (10 mm in diameter) were drilled in the GRP test plates, using a tungsten carbide tipped drill and a timber backing plate. The bolts were

nominally tight fitting and had the smooth part of the shank in contact with the cylindrical surface of the bolt hole. The bolts were lightly torqued to 3 Nm (the finger-tight condition).

For each parameter set, i.e. each specific value of E/D, W/D and angle, α, three nominally identical single-bolt joints were tested. The tension load was applied at a rate of approx. 10 kN/min. During each test load and extensomer readings were sampled and logged automatically at half-second intervals in order to capture the complete load–deformation response of the joint. An example of the variability between the load vs extension responses of three nominally identical tension joints is shown in Fig. 3.

5. Off-axis test data and discussion

A total of 54 single-bolt joints were tested in tension, i.e. 18 joints for each of the three angles between the pultrusion and tension axes, i.e. off-axis angles, $\alpha = 30°$, 45° and 90°. The new test data details are given in parts (a)–(c) of Table 2. For the sake of completeness the data given in [5] for the angle, $\alpha = 0°$, are reproduced in part (d) of Table 2.

Examples of the failure modes in single-bolt tension joints for the angles, $\alpha = 90°$, 45° and 30° respectively are shown in Plate 3. It is of interest to note that whilst
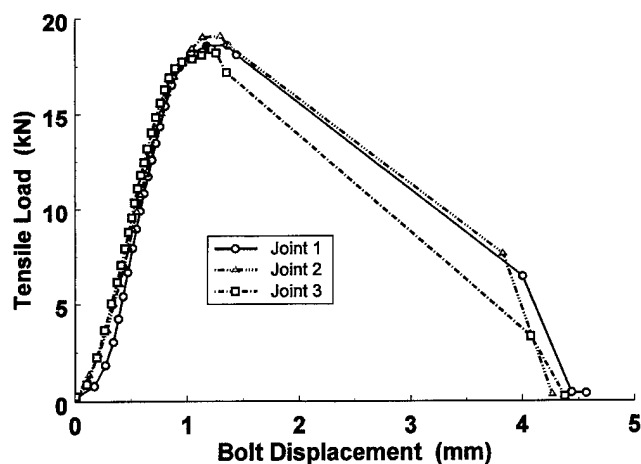
Fig. 3. Typical load vs extension response curves for three nominally identical single-bolt tension joints ($E/D = 4.5$; $W/D = 10$ and $\alpha = 90°$).

the failed specimens shown in Plate 3 are for specific values of the E/D and W/D ratios, it was observed that for each α-value the same type of failure mode occurred throughout the range of E/D and W/D values tested. Clearly, as shown in Plate 3(a), the mode of failure is a classical tension mode failure. The crack propagates from the edges of the hole, i.e. at points defined by the intersection of a diameter normal to the tension axis with the hole circumference, across the full width of the GRP plate. For these plates the strength of the joint derives primarily from the strength of the CFM and the matrix, since the rovings have negligible transverse strength. In Plates 3(b) and (c) the failure modes shown are also denoted as tension failure modes. However, the crack propagation direction is not maintained. Cracks initiate at the same locations on the hole circumference, as in the joints with $\alpha = 90°$ [see Plate 3(a)], but, generally, they only propagate across the plate width until they encounter the first set

Table 2
Single-bolt tension joint test results for 6.4 mm thick EXTREN™ 500 Series pultruded GRP plate

W/D ratio	E/D ratio	Average initial bolt slip (mm)	Average bolt displacement at failure (mm)	Average initial stiffness (kN/mm)	Average failure load (kN)	Mode of failure
(a) Off-axis angle, $\alpha = 90°$						
10	6	0.12	1.44	26.88	22.23	Tension*
10	4.5	0.08	1.25	23.17	18.90	Tension*
10	3	0.17	1.14	24.44	16.71	Tension
8	6	0.15	1.13	23.36	19.08	Tension
6	6	0.11	1.08	20.51	16.57	Tension
4	6	0.16	0.95	17.34	12.14	Tension
(b) Off-axis angle, $\alpha = 45°$						
10	6	0.24	2.03	28.98	27.08	Tension*
10	4.5	0.22	1.67	26.62	22.94	Tension*
10	3	0.18	1.17	26.56	19.82	Tension
8	6	0.16	1.61	25.91	23.86	Tension*
6	6	0.21	1.22	23.75	20.19	Tension
4	6	0.10	0.88	19.82	14.03	Tension
(c) Off-axis angle, $\alpha = 30°$						
10	6	0.21	2.10	30.58	30.93	Tension*
10	4.5	0.21	1.67	29.66	26.62	Tension*
10	3	0.18	1.08	25.53	20.85	Tension
8	6	0.17	1.66	28.07	26.67	Tension*
6	6	0.12	1.41	26.65	22.49	Tension*
4	6	0.16	0.98	20.87	15.55	Tension
(d) Off-axis angle, $\alpha = 0°$						
10	6			36.9	27.5	Bearing
10	5			41.8	28.9	Bearing
10	4			37.8	27.5	Cleavage
10	3			37.6	23.6	Shear
10	2			34.1	16.8	Shear
8	5			35.7	29.3	Bearing
6	5			32.0	25.5	Bearing
4	5			29.4	21.4	Tension
2	5			17.2	10.1	Tension

*Denotes slight evidence of bearing damage around hole.

(a)

$\theta = 90°$; E / D = 6 ; W / D = 10

(b)

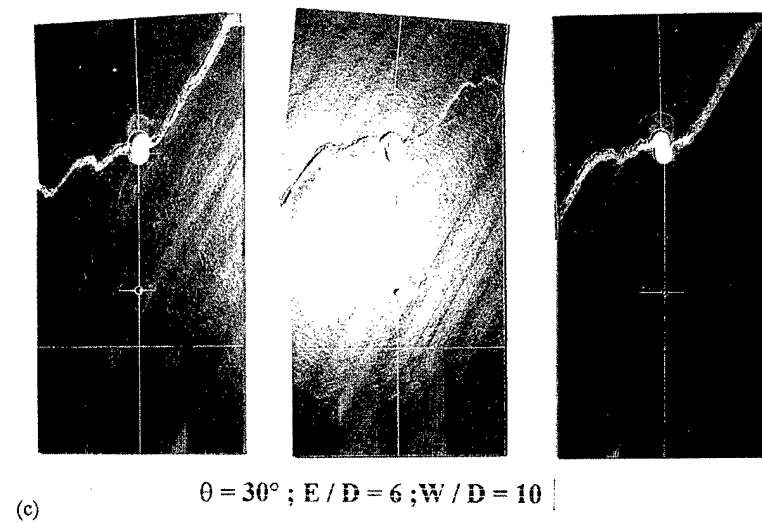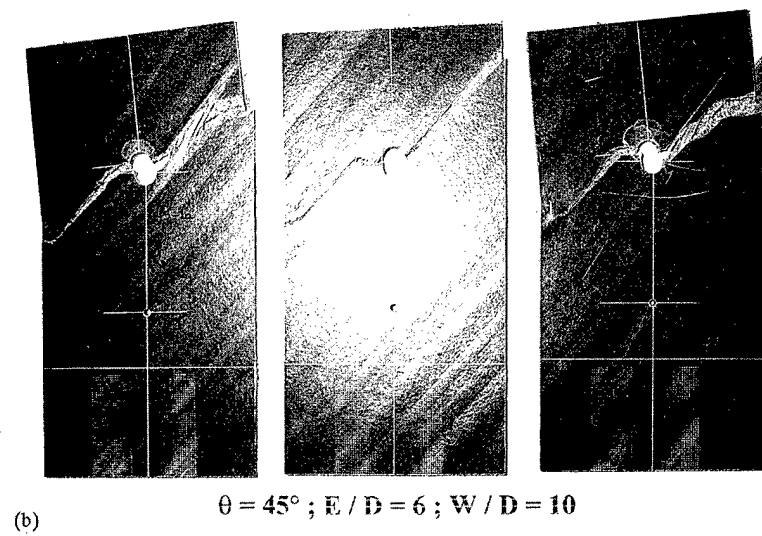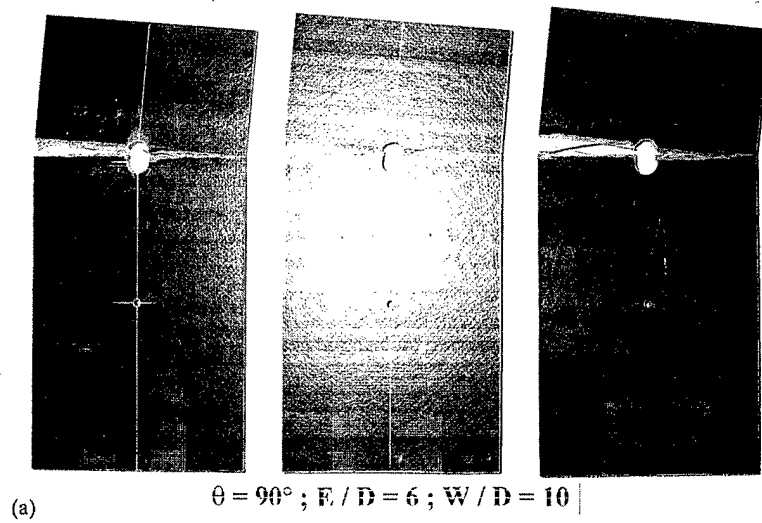$\theta = 45°$; E / D = 6 ; W / D = 10

(c)

$\theta = 30°$; E / D = 6 ;W / D = 10

Plate 3. Failure modes in single-bolt tension joints in EXTREN[TM] 500 Series pultruded GRP plate: (a)$\alpha = 90°$; (b) $\alpha = 45°$ and (c) $\alpha = 30°$.

of off-axis rovings. These provide weaker, alternative paths, along which the two cracks propagate towards the edge of the plate.

The new single-bolt tension joint data may be combined with the tension joint data for $\alpha = 0°$, given in [5] and listed in Table 2(d), to provide a more comprehensive picture of how the ultimate load capacity of the joint changes with the joint geometry and the inclination of the tension axis to the pultrusion axis, i.e. the off-axis angle, α. This may be expressed simply through plots of the joint failure load vs the E/D and W/D ratios. These plots are shown in Fig. 4(a) and Fig. 4(b) respectively. It is evident, from Fig. 4(a), that as the E/D ratio increases, the failure load of the joint also increases. The same figure also shows, for a given E/D value, that the load capacity of the joint increases as the off-axis angle, α, decreases. However, in the case of the tests for $\alpha = 0°$, the increase in load capacity does not continue to increase beyond an E/D ratio of about 5, because the mode of failure changes to bearing, whereas for the other off-axis angles there

does not appear to be such a limit on the E/D ratio. It appears that similar trends are evident in Fig. 4(b), i.e. the load capacity of the joint increases as the W/D ratio increases and, for a specific value of the ratio, the capacity increases as the α-value reduces. Again, when the W/D ratio exceeds 8 there appears to be no further increase in the load capacity of joints with $\alpha = 0°$, because the mode of failure changes to bearing.

The results presented in Table 2(a)–(c) also shed light on manufacturing tolerances which may be expected when simple tools are used to drill holes in pultruded GRP plate. In this case, a pillar drill was used with a drill tip speed in the range 800–1000 rpm. The 10 mm holes were drilled with a 10 mm diameter tungsten carbide tipped drill in order to produce a tight fit with the smooth surface of the bolt shank. However, as is evident from the measured average initial bolt slips listed in these tables, which range from 0.08–0.24 mm, there was probably a small amount of clearance present. Thus, it is not possible to produce very tight-fitting bolts in these materials with conventional drills. For the case of large E/D ratios Fig. 5(a) shows the average initial bolt slip for three off-axis angles as a function of the W/D ratio. Similar data for large W/D ratios is shown in Fig. 5(b). It appears that for $\alpha = 90°$ the bolt slip decreases as E/D and W/D increase, whereas for $\alpha = 45°$ and 30°, the reverse appears to occur.

The bolt displacements at failure, relative to a fixed point on the GRP plate (see Fig. 2), are also given in Table 2(a)–(c). These displacements range from 0.88–2.1 mm, i.e. about 5–10 times the initial bolt slip. For large E/D ratios the bolt displacement at failure as a function of the W/D ratio is shown in Fig. 6(a). It appears that the displacement increases as W/D increases, but less significantly for $\alpha = 90°$. Corresponding data for large W/D ratios is shown in Fig. 6(b). The same trends are evident, i.e. the displacement at failure increases as the E/D ratio increases, but less rapidly for $\alpha = 90°$.

The same tables also provide information on the average stiffness of the tension joints as the E/D and W/D ratios vary. Figure 7(a) shows that for large E/D ratios the average initial stiffness of the joint increases as W/D increases. The stiffness increase does not appear to be affected significantly by the value of the off-axis angle, α. On the other hand, Fig. 7(b) suggests that for large W/D ratios the average initial stiffness of the joint is largely independent of the E/D ratio. Both of the trends shown in Figs 7(a) and (b) are not unexpected, since the W/D ratio would control the tensile stiffness of the joint.

From the design standpoint what is perhaps of most concern about the off-axis tension joint data presented is that the bearing failure mode does not seem to exist even for relatively small off-axis angles, i.e. $\alpha = 30°$. For
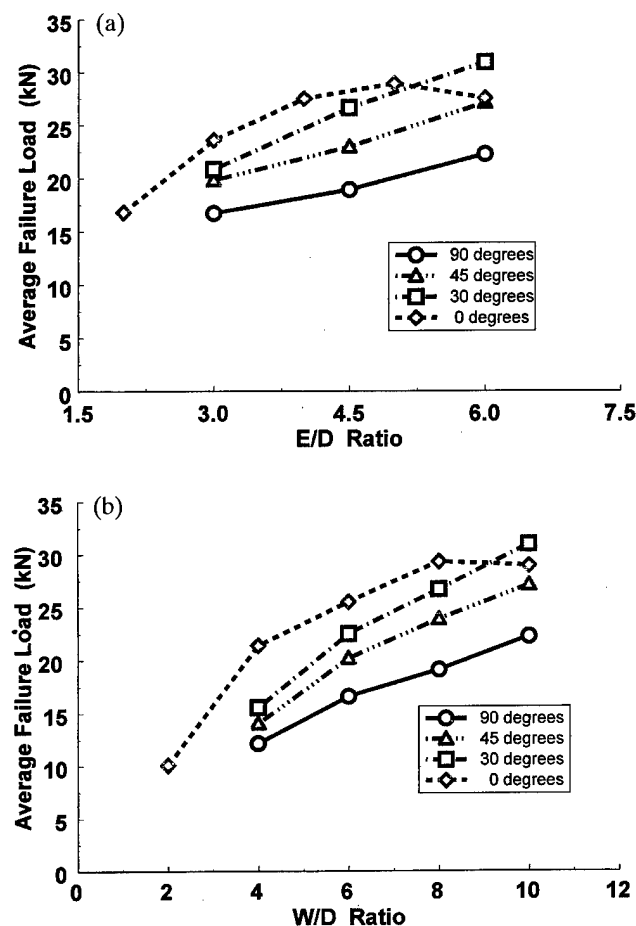

Fig. 4. Ultimate load capacity data for single-bolt joints in tension: (a) average failure load vs E/D [$W/D = 10$] and (b) average failure load vs W/D [$E/D = 6$ ($\alpha = 90°$, 45° and 30°) and $E/D = 5$ ($\alpha = 0°$)].

such joints failure occurs suddenly and the accompanying drop in load may be very substantial, i.e. the failure mode is far from benign as with bearing failure. This has serious implications for multi-bolt plated joints in which off-axis loading may arise. Another worrying feature arising from the failure mode observations is the role played by the rovings. They seem to constitute bands of weakness within the plate material along which cracks prefer to propagate. This raises the question as to whether rovings should be present (some rovings are, of course, required in order to pull the CFM reinforcement through the pultrusion die) in the material if they cause localised bands of weakness. An alternative view is that they may be regarded as crack arrestors and/or guides and this attribute may be exploited to advantage in the layout and design of the joint.

6. Concluding remarks and future developments

The literature on single-bolt tension joint tests in pultruded GRP plate material has been reviewed. The review has highlighted the fact that there appears to be no consensus as to the preferred test configuration for conducting such tests and, moreover, there appears to be no preferred arrangement for measuring the joint extension.

Despite the relatively large number of tests reported, it appears that limited data is available on single-bolt tension joints in which the pultrusion and tension axes are neither coincident with nor normal to one another. The tests reported herein provide such data, but only for one plate thickness and one bolt diameter. The test results are of interest, because they seem to imply that there is very little evidence of any bearing failure (the relatively benign failure mode) once the off-axis angle, α, exceeds 30°. The failure modes in these joints are
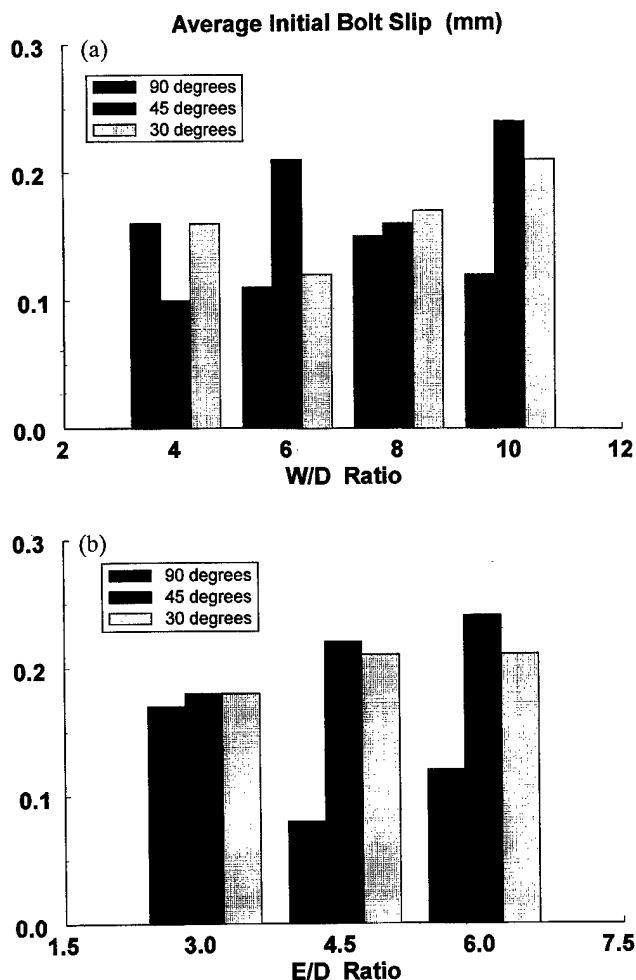

Fig. 5. Initial slip data for single-bolt joints in tension: (a) average initial bolt slip vs W/D $[E/D = 6]$ and (b) average initial bolt slip vs E/D $[W/D = 10]$.
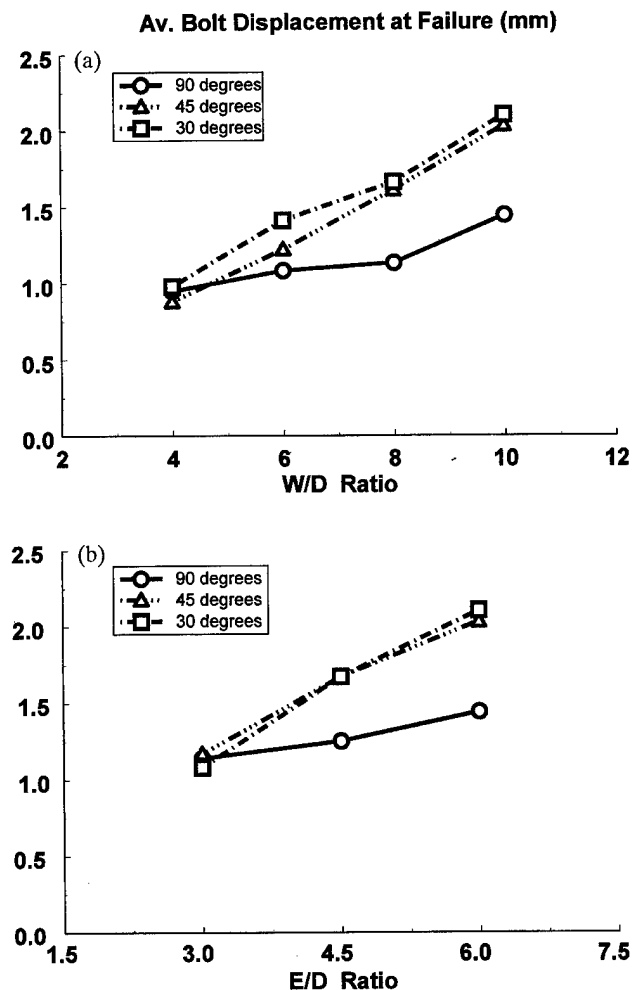
Fig. 6. Failure displacement data for single-bolt joints in tension: (a) average bolt displacement at failure vs W/D $[E/D = 6]$ and (b) average bolt displacement at failure vs E/D $[W/D = 10]$.

also of interest, because they show that cracks propagate along the rovings, which may be viewed (negatively) as zones of weakness, or alternatively (positively) as crack guides and/or arresters.

The displacement measurements made on the joints indicate that a small amount of bolt slip occurs even when the holes are nominally a tight fit. Furthermore, the bolt displacement at failure varies from 5-10 times the initial slip value.

Inital joint stiffnesses have also been determined and these do not appear to vary much with the *E/D*, but increase both with increasing *W/D* and decreasing α.

The paper has shown that there is a need to obtain much more data if the failure response of single-bolt tension joints in structural grade pultruded GRP plate is to be properly characterised. A potentially useful future exercise might be to combine the present data with that of Refs. [1] and [4] in order to establish any

plate thickness effects, since the data span a large range of plate thicknesses. Also it should be possible to develop design equations, similar to those in Ref. [1], for the present test data. This would entail determining certain empirical coefficients which could be compared with those given in Ref. [1] and would also show how these are affected by further reduction in plate thickness (the smallest plate thickness used in the joint tests reported in Ref. [1] was 9.5 mm).

At the time of writing further testing on single-bolt tension joints in 3.2 mm EXTREN™ 500 Series pultruded GRP plate is being carried out and this data should be available in due course.

Acknowledgements

Fig. 7. Stiffness data for single-bolt joints in tension: (a) average initial stiffness vs *W/D* [*E/D* = 6] and (b) average initial stiffness vs *E/D* [*W/D* = 10].

References

[1] Rosner C, Rizkalla SH. Design of bolted connections for orthotropic fibre-reinforced composite structural members. In: Neale KW, Labossiere P, editors, Advanced composite materials in bridges and structures (ACMBS-1/MCAPC-1). Montreal: Canadian Society of Civil Engineering, 1992:373–82.

[2] Hart-Smith LJ. Mechanically-fastened joints for advanced composites — phenomenological considerations and simple analyses. Proceedings of the Fourth Conference on Fibrous Composites in Structural Design, San Diego, California. New York:Plenum Press, 1980:543–74.

[3] Abd-El-Naby S.F.M., Hollaway L.. The experimental behaviour of bolted joints in pultruded glass/polyester material. Part 1: single-bolt joints. Composites 1993;24(7):531–538.

[4] Erki, MA. Investigation of bolted composite connections for military structures. Internal report, Department of Civil Engineering, Royal Military College of Canada, Kingston, Canada, January 1992.

[5] Cooper C., Turvey G.J.. Effects of joint geometry and bolt torque on the structural performance of single bolt tension joints in pultruded GRP sheet material. Composite Structures 1995;32(3/4):217–226.

[6] Turvey GJ, Cooper C. Single bolt tension joint tests on pultruded GRP WF-section web and flange material. Proceedings of the 10th International Conference on Composite Materials (ICCM-10), Whistler, British Columbia, 1995;III:621–8.

[7] Yuan RL, Liu CJ, Daly T. Study of mechanical connection for GRP laminated structures. In: El-Badry M, editor, Advanced composite materials for bridges and structures. Montreal: Canadian Society for Civil Engineering, 1996:951–8.

[8] Sotiropoulos S, GangaRao HVS, Lopez-Anido R. Evaluation of FRP composites bolted and adhesive joints. Proceedings of the 1996 Materials Engineering Conference, ASCE, New York, 1996;1:233–42.
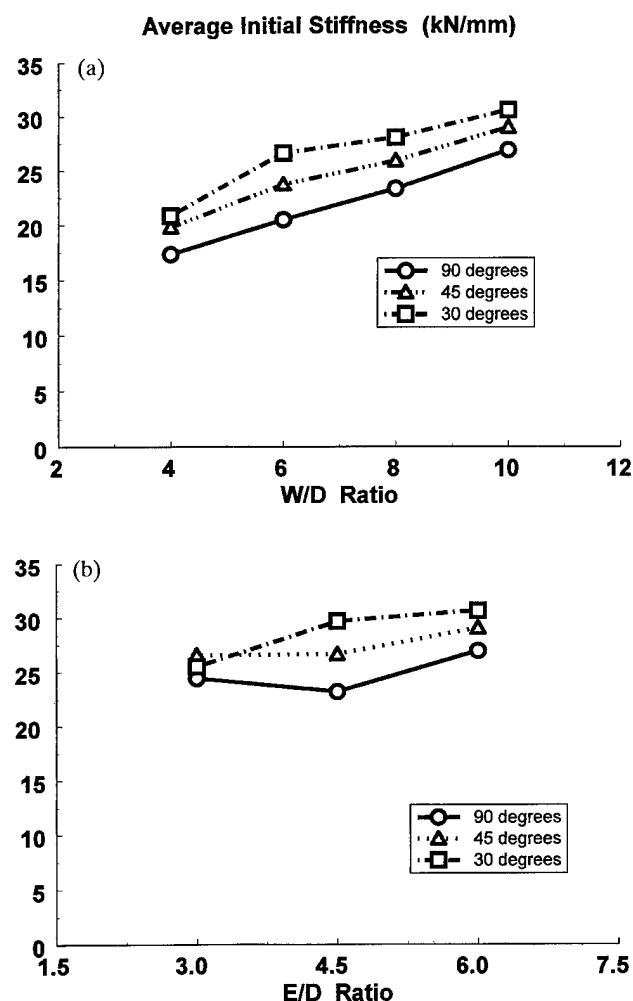
[9] Meyer RW. Handbook of pultrusion technology. New York: Chapman and Hall, 1985.

[10] Anon, EXTREN fiberglass structural shapes: design manual. Bristol, VA: Morrison Molded Fiber Glass Company, 1989.

COMPOSITE STRUCTURES

ELSEVIER

Interpretation of signals from dropweight impact tests

M. S. Found*, I. C. Howard, A. P. Paran

SIRIUS, Department of Mechanical Engineering, University of Sheffield, Mappin Street, Sheffield S1 3JD, UK

Abstract

A spring-mass model has been developed to describe the dropweight impact response of CFRP panels. The model separates the effects of the main impact impulse, high frequency oscillations and free vibrations and can be used as a reliable guide for effective digital filtering of signals from dropweight impact tests. Whilst the model at present does not account for damage, the onset of high frequencies towards the peak impact force indicate the onset of damage in the panel. The oscillations become larger and extend over a wider plateau as the perforation threshold energy is approached. © 1998 Published by Elsevier Science Ltd. All rights reserved.

1. Introduction

The problems associated with the low velocity impact response of fibre reinforced plastic structures have been the subject of many investigations for more than two decades. This is because of the high probability of such loadings occurring during the manufacture, service or maintenance of composite structures. Impact loading induces a complex interaction between structural and material behaviour. The mechanical response of laminates to impact is an essentially global response mainly by flexural distortion and locally by indentation and is dependent upon structural constraints, stiffness and geometry [1]. The damage induced provides an interaction of a range of failure mechanisms such as indentation, debonding, matrix cracking, delamination and fibre fractures which are dependent upon fibre and matrix properties, stacking sequence and geometry [2].

The term, low velocity, as applied to impact loading is often not fully understood nor clearly defined. In order to justify the analytical techniques being employed to assess the impact response of structural elements it is important to state the appropriate assumptions. It has been suggested that the impact event may be classified in terms of striker/target interactions such as pulse period, frequency, striker rigidity and target geometry [3]. Robinson and Davies [4] have defined low velocity impact in which through-thickness stress waves in the specimen do not influence the stress distribution at any time during the impact event. A transition velocity when stress waves are significant may be assessed in terms of the stress wave propagation through the thickness at the speed of sound and in terms of failure strain of the laminate. Assuming nominal failure strain of 1% for carbon/epoxy laminates indicates that stress waves become dominant at velocities of about 20 m/s. Much of our impact evaluations have been undertaken at velocities less than 5 m/s, as in the work reported here, and therefore can be considerd as being of low velocity.

While instrumented dropweight impact test facilities have been available for many years there are still only a few test standards [5,6] for evaluating the impact behaviour of FRP composites. Such standards are of limited use except for specifying standard specimen geometries and test methods. Whilst standard test methods and specimen geometries permit comparisons between the impact response of different materials extreme care should be used in trying to predict the likely response of large structures based on small laboratory specimens. Our latest work on CFRP panels indicates that the transition between different failure mechanisms changes significantly with test panel geometry and that there is a minimum size of specimen required for predicting the behaviour of large structural elements with some degree of accuracy. These and othe related issues will be reported in a future paper. We are not aware of any standards for the procesing of data from impact tests although it is

*Corresponding author.

widely known that the effects of so called noise, or ringing, are inherent in monitoring the impact event. The first stage is to try to minimize such effects by careful design of the impact rig, especially the impactor carriage, as it slides down the guide rods. Next, the amplitude of ringing may be reduced by lowering the impact velocity since the amplitude is proportional to velocity. Finally, if the problem still persists filtering of the test data should be undertaken.

The filtering of impact test data is a contentious issue and is the main thrust of this paper. It is essential to save the original unfiltered data such that the effects of filtering can be readily compared. Therefore, digital filtering techniques are preferred to analogue methods since the latter increase the risk of masking or losing data. Guidelines for analysing data from impact tests including filtering can be found in the works of Cheresh and McMichael [7] and Cain [8], who developed a low-pass filter. However, the adequate filtering of impact test data can only reliably be achieved through an understanding and separation of signal frequencies and thus differentiate between real events and noise. We were concerned that the impact response of CFRP panels of similar diameter and lay-up and clamped to the same pressure produced quite different force–time histories for 3-ply laminates compared with 9-ply laminates. Typical force–time histories for these laminates are shown in Fig. 1 for impact tests undertaken at incident kinetic energies of 0.471 and 1.323 J which represent approx. 20 and 10% of the respective perforation threshold energies and did not induce any damage. The data was filtered in a similar manner with a cut-off frequency of 3.5 kHz but we needed to know if the high frequency oscillations in the 3-ply laminates were real or associated with the filtering process. We therefore proceeded to develop a greater understanding of the physical parameters that control the response of panels to dropweight impact tests through modelling of the impact event using a spring-mass model, details of which are presented later in this paper. Similar spring-mass models have also been used by Cain [8], Lifshitz et al. [9] and Shiva-kumar et al. [10] in an attempt to identify how the observed vibrational responses can be related to separate dynamic effects.

The overall aim of our programme of work on impact behaviour of FRP composites is to study the effect of static indentation, and single and repeated impacts on plain and stiffened panels and hence to attempt to predict the damage tolerance of real structures. This paper reports our findings on the interpretation of signals from dropweight impact tests conducted on carbon fibre reinforced plain panels and fomulates a spring-mass model in order to assess appropriate levels of filtering of the test data.

2. Experimental test facility

An instrumented dropweight rig, briefly described in Ref. [11], has been developed enabling impact tests and static indentation tests to be conducted on circularly clamped panels under similar test constraints. The test rig has recently been modified to permit clamping of large panels [12] and also to accommodate stiffened sections [13]. The impact rig is equipped with four transducers namely, an accelerometer, a strain-gauged load cell, a displacement transducer and opto-electronic triggering and timing sensors. The transducers are located as shown schematically in Fig. 2.

The accelerometer is a miniature piezoelectric transducer model 2255A-025, supplied by Endevco, which is connected via signal conditioner model 4416B to the data acquisition system. Four electrical resistance strain gauges are mounted on the shank of the indentor nose, two longitudinally and two circumferentially, and connected in a wheatstone bridge arrangement and the signal conditioned using strain module MB38-02 supplied bye Keithley Instruments. An infrared LED/phototransmitter reflective transducer, comprising a spectrally matched GaAs infrared emitter (type SE 3455) and a silicon phototransistor (type SD 5443) supplied by Honeywell Optoelectronics is used to determine the displacement of the panel during impact. The transducer is located beneath the test panel at a position 25 mm offset from the point of load application in order to prevent the signal from being affected by any damage produced on the backface. The transducer is calibrated from static load tests performed under identical clamping conditions using an LVDT to measure the deflection at the centre of the panel.

The instrumented indentor is released from a predetermined height by an electromagnetic switch. The data acquisition system is triggered when an aluminium flag, attached to the indentor assembly, passes the first opto-interrupter, an infrared emitting LED and phototransistor (type 307-913) supplied by RS Components. The indentor velocity immediately before the impact event is determined by measuring the time taken for the flag, of 15.5 mm depth, to cross the line of sight of the second opto-interrupter. The sensors are also used to determine the rebound velocity when energy is returned to the indentor after the impact event.

The four transducers are connected to a Keithley Instruments DAS 1401 data acquisition board which is installed in an IBM PC/AT compatible desktop computer as shown schematically in Fig. 3. The board is a multi-layer construction with integral ground plane to minimize noise and crosstalk. The system has a maximum sampling rate of 100 kHz and allows the monitoring of up to eight channels of bipolar data. For

monitoring of the four transducers four channels are employed and the data sampled at a rate of 25 kHz. With more advanced, and expensive, equipment it is possible to sample all channels at a higher single rate. The system is triggered via the reference or zero channel whilst the accelerometer, load cell and displacement transducer are connected to channels 1–3

respectively and the timer operates via channel 4. The data acquisition system is completed with Easyest LX software from Keithley Asyst enabling storage, manipulation and filtering of the data. Three types of digital filter are available, namely low pass, high pass and band pass. In addition, a transition width must be specified to determine the region where the filter's
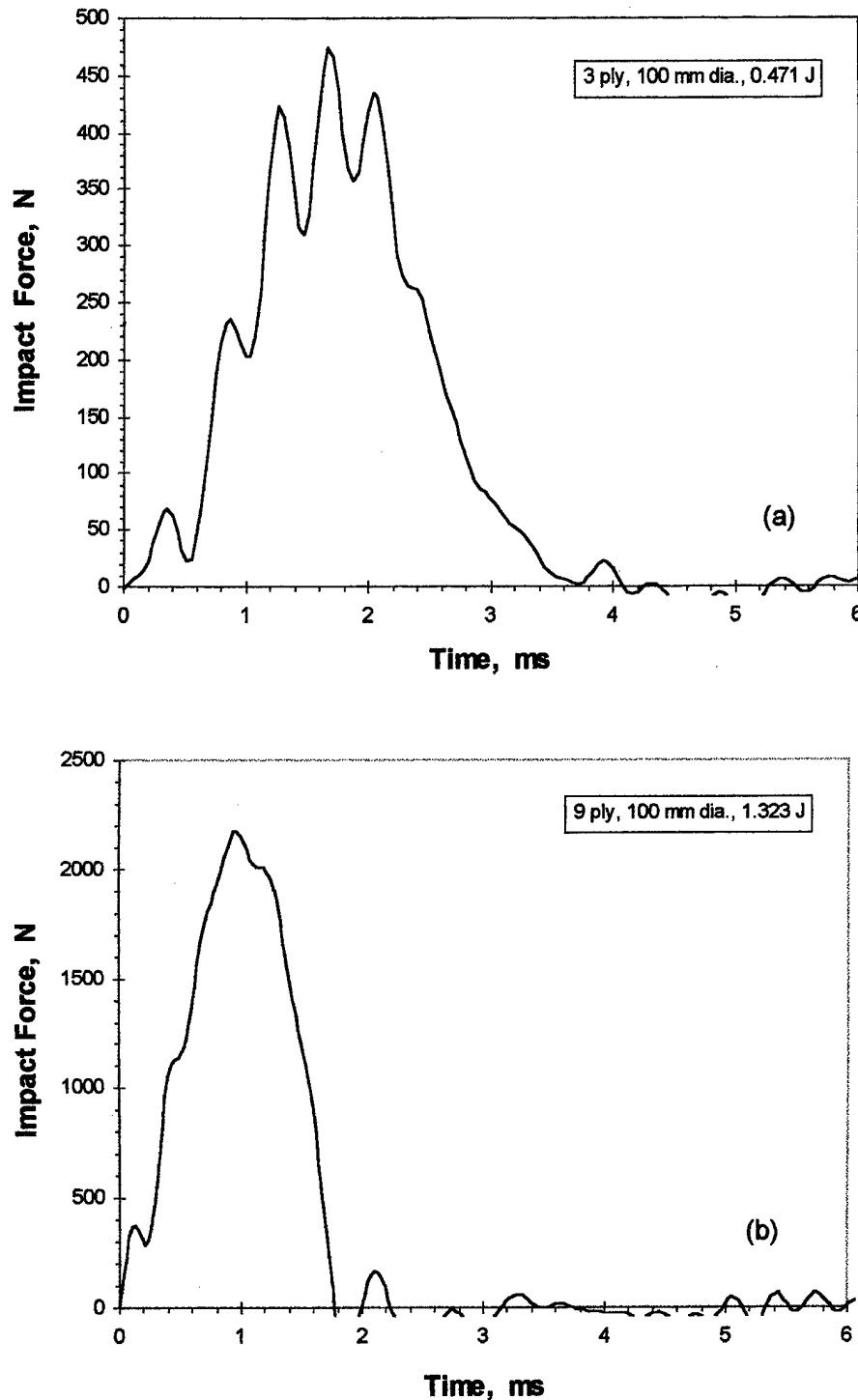
Fig. 1. Typical force–time signals for (a) thin (3-ply) and (b) thick (9-ply) laminates with no damage.

passband response drops from one to zero. This varies from a maximum of 0.5 times to a minimum of 0.05 times the acquisition rate with the cut-off frequency used at the centre point for the transition. Invalid results are obtained for a transition width too large for the specified cut-off frequency.

3. Mechanical model

Whilst it is usual to filter data recorded from impact tests extreme care is required in order to ensure that significant events are not removed by filtering and thus preventing erroneous interpretation of the impact event. The use of models enables interpretation of the signals prior to filtering and to assess the separate responses of the indentor, rig constraint and test panel during and after the impact event. A linear mechanical model was constructed of a dynamic system comprising the dropweight and the test panel using masses, springs and dampers as shown in Fig. 4. The elements m_1, m_2. k_1 and c_1 represent the dropweight and the elements k_2 and c_2 represent the stiffness of the indentor nose. The surface indentation stiffness of the panel is represented by the elements k_3 and c_3 and the panel is represented by its equivalent mass m_4 and the stiffness elements k_4 and c_4.

The differential equations describing this system are:
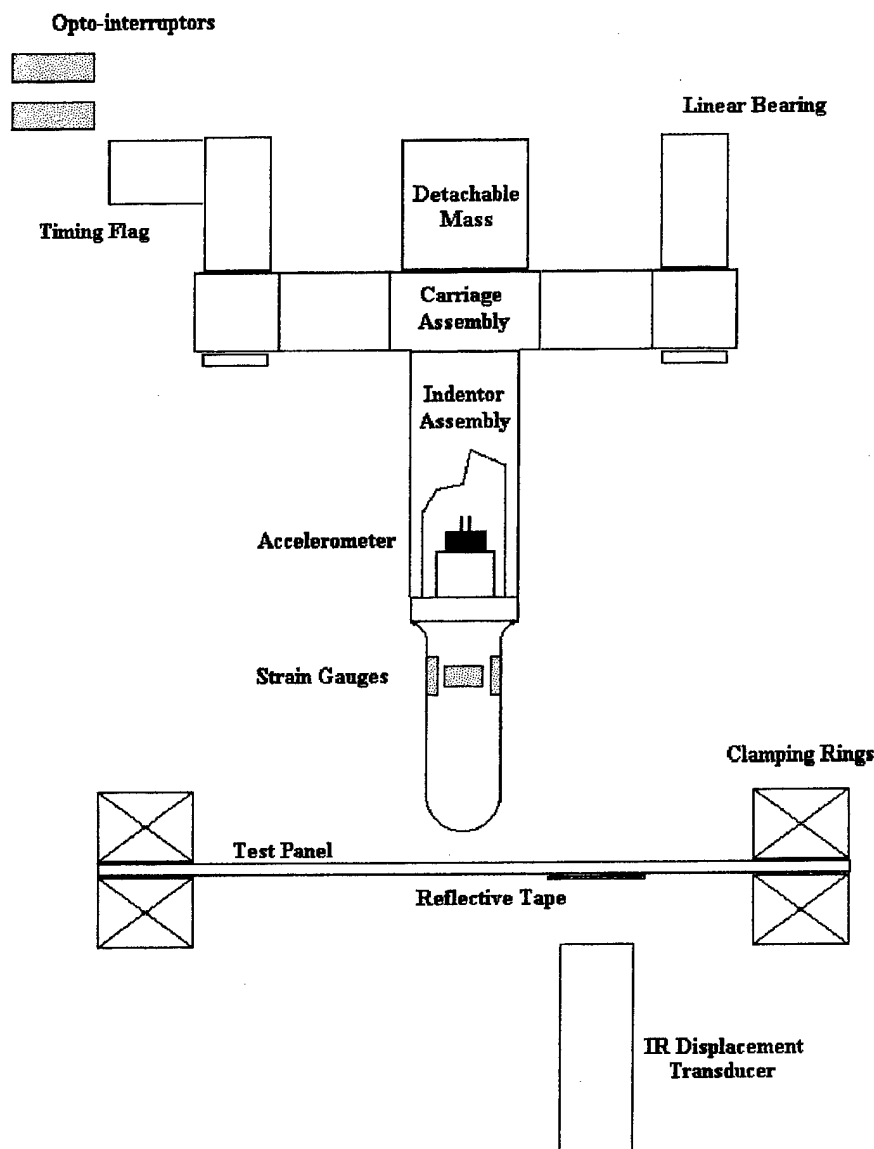
Fig. 2. Schematic arrangement of indentor assembly showing location of strain gauges, accelerometer, added masses and other details.

$$m_1\ddot{y}_1 = -c_1(\dot{y}_1 - \dot{y}_2) - k_1(y_1 - y_2) \qquad (1)$$

$$m_2\ddot{y}_2 = -c_2(\dot{y}_2 - \dot{y}_3) - k_2(y_2 - y_3)$$

$$+ c_1(\dot{y}_1 - \dot{y}_2) + k_1(y_1 - y_2) \qquad (2)$$

$$m_4\ddot{y}_4 = -c_4\dot{y}_4 - k_4 y_4 + c_3(\dot{y}_3 - \dot{y}_4) + k_3(y_3 - y_4) \qquad (3)$$
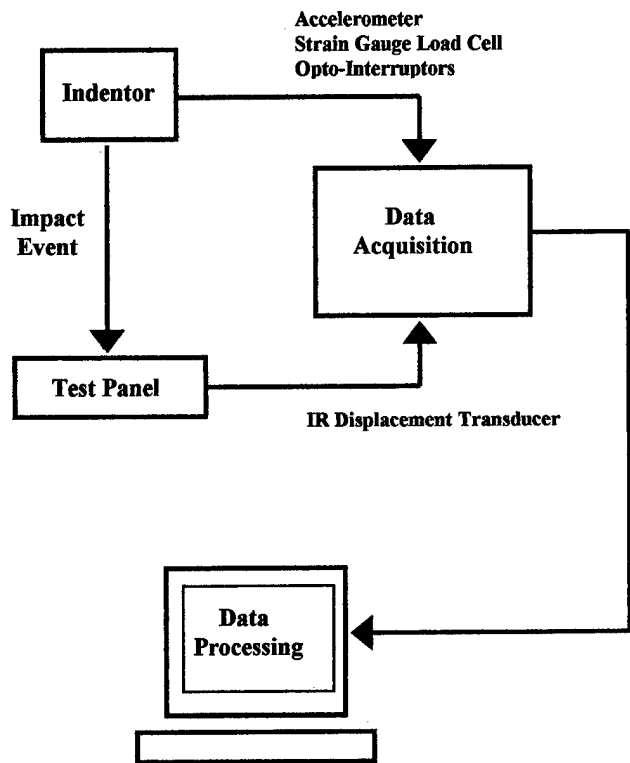
Fig. 3. Schematic diagram of data acquisition system.
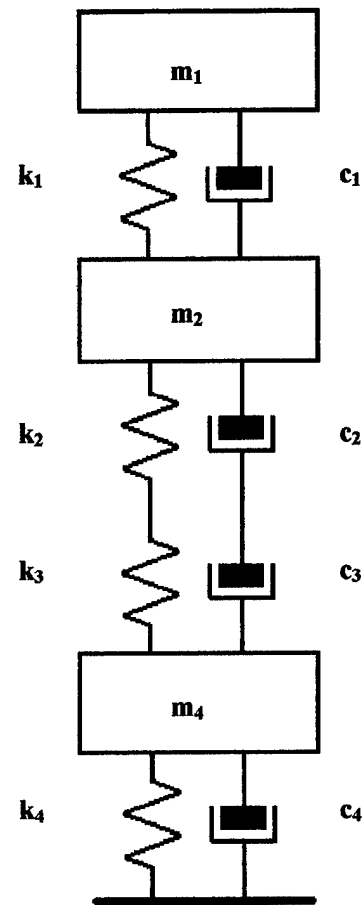
Fig. 4. Model of impact event.
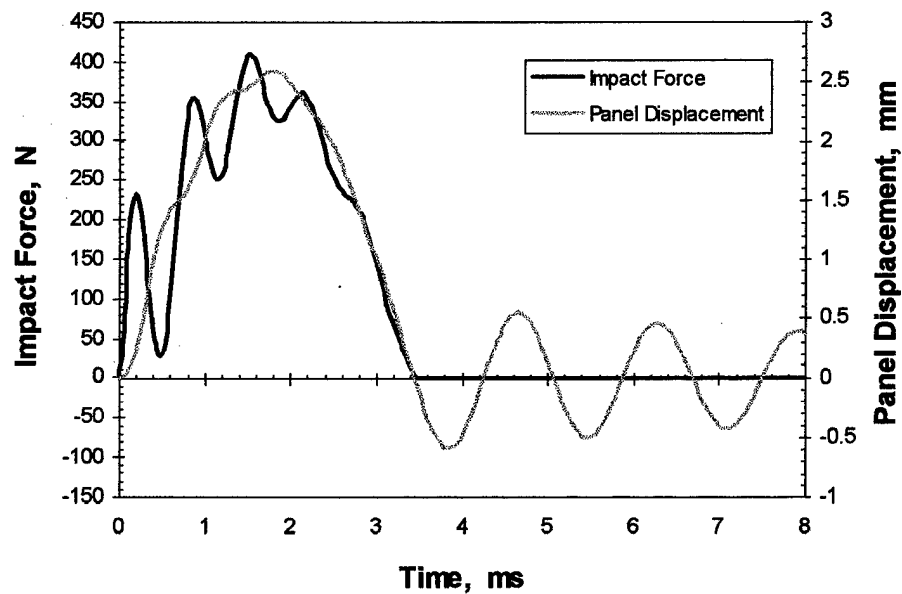
Fig. 5. Impact force and panel displacement as calculated from the numerical model for a 3-ply panel.

These equations are subject to the following constraints:

$$c_3(\dot{y}_3 - \dot{y}_4) + k_3(y_3 - y_4) = c_2(\dot{y}_2 - \dot{y}_3) + k_2(y_2 - y_3) \qquad (4)$$

$$k_2 = 0 \quad \text{and} \quad c_2 = 0 \quad \text{if} \quad (y_2 - y_3) < 0$$

$$k_3 = 0 \quad \text{and} \quad c_3 = 0 \quad \text{if} \quad (\dot{y}_3 - \dot{y}_4) < 0$$

The spring and damper constants for the panel (k_4, c_4) and its surface (k_3, c_3) are evaluated from static indentation tests. The model does not take into

account any damage occurring in the panel and this issue will be addressed in a future paper.

4. Assessment of data filtering

A series of dropweight impact tests were undertaken on thin CFRP laminates clamped between two annular rings of 100 mm internal diameter. The tests were conducted from a height of 0.5 m whilst the mass was varied to produce a range of incident kinetic energies. The material was a five-harness satin weave carbon-fibre fabric impregnated with an epoxy resin type 914C-713-40 supplied by Hexcel Composites. The
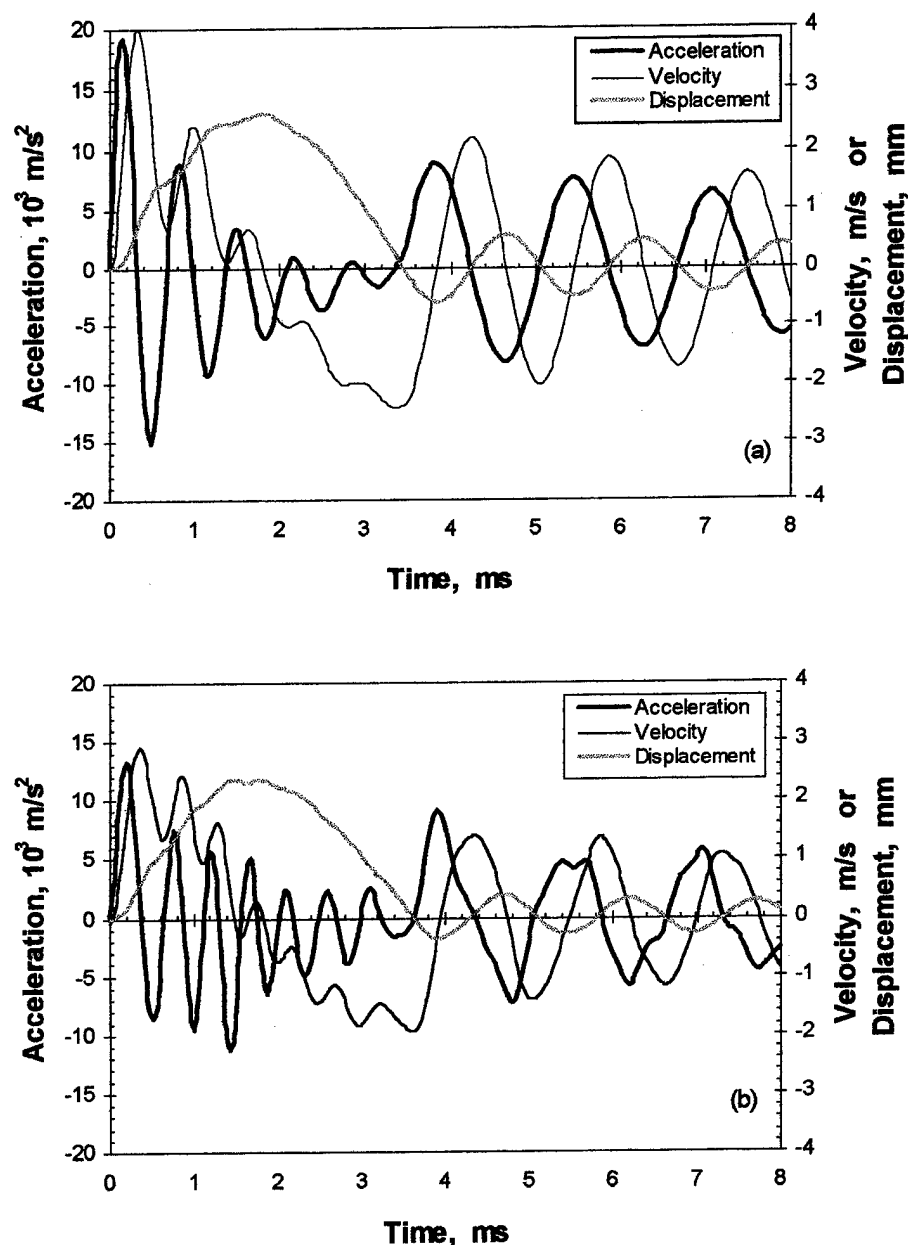
Fig. 6. Plots of panel acceleration, velocity and displacement for (a) the numerical model and (b) the experimental data.

panels were laid up as 3-ply (0/90, ±45, 0/90) laminates and autoclave moulded by Hurel-Dubois UK to a thickness of 0,96 mm at a nominal 58% fibre volume fraction.

When using four transducers the maximum sampling rate is 25 kHz and the Nyquist rule [14] dictates that the maximum bandwidth if the signals in the data is half this value, i.e. 12.5 kHz. Theoretically any digital filtering must be done at a cut-off frequency at or below this value. However, in practice it is recommended that the cut-off frequency must be 10–15% of the bandwidth of the data in order to avoid problems. To determine the optimum cut-off frequency for digital filtering of the data eqns (1)–(3) were numerically solved and the results compared with the experimental data filtered at different values of cut-off frequency.

Figure 5 shows the impact force–time and displacement–time histories for a 3-ply panel subjected to a kinetic energy of 0.471 J as determined from numerical solving of the mechanical model. In this preliminary modelling exercise panel stiffness only has been considered with no allowance for membrane bending

Fig. 7. Components of the numerical model.

of these thin laminates. In addition, the masses m_1 and m_2 have been lumped together since their accelerations were shown to be almost identical. It indicates that the peaks and valleys observed in the impact force history correspond with changes in the slope or inflection points in the displacement history of the panel. This suggests that there is an important interaction between the indentor and the panel during the impact event which is controlled by the contact stiffness that is present between the two bodies and by the global stiffness of the panel. The displacement history also shows that there is energy transferred to the panel during the impact event that excites transverse vibrations in the panel which persist well after the impact event.

The acceleration, velocity and displacement histories of the 3-ply panel are presented in Fig. 6 for the same incident kinetic energy of 0.471 J. The numerical solution illustrated in Fig. 6(a) shows that the acceleration of the panel is, as expected, completely different from that of the indentor implying that the panel experiences entirely different dynamic forces during the impact event. The numerical solution is compared with experimental data by twice differentiating the panel displacement history in order to obtain the velocity and acceleration histories of the panel. The appropriate level of filtering was achieved by matching the displacement signal from the model to the experimental data. The best results were obtained when using the low pass filter with a cut-off frequency of 3.5 kHz, which is 28% of the bandwidth of the signals, as shown in Fig. 6(b). The transition width of the filter's passband was approx. 1 kHz, i.e. from 3 to 4 kHz. This suggests that the predicted behaviour of the panel gives reasonable agreement with the panel response observed from the test, the main difference being an overestimation of the magnitude of the velocity and acceleration at the start of the impact event. This is probably due to the non-linear stiffening response of the actual panel which has been represented by a linear model.

5. Discussion

The model can be shown to comprise three basic components as illustrated in Fig. 7. The main impact impulse indicates the behaviour and shape of the displacement–time profile and is controlled by the mass of the indentor M_i, the contact stiffness and the global panel stiffness. The contact interface is represented by two springs in series such that the stiffness of the nose of the indentor is much greater than the stiffness of the laminate. K_c is the equivalent contact stiffness and K_p is the equivalent panel stiffness. Superimposed on the main impulse are high frequency oscillations controlled by the panel mass M_p and
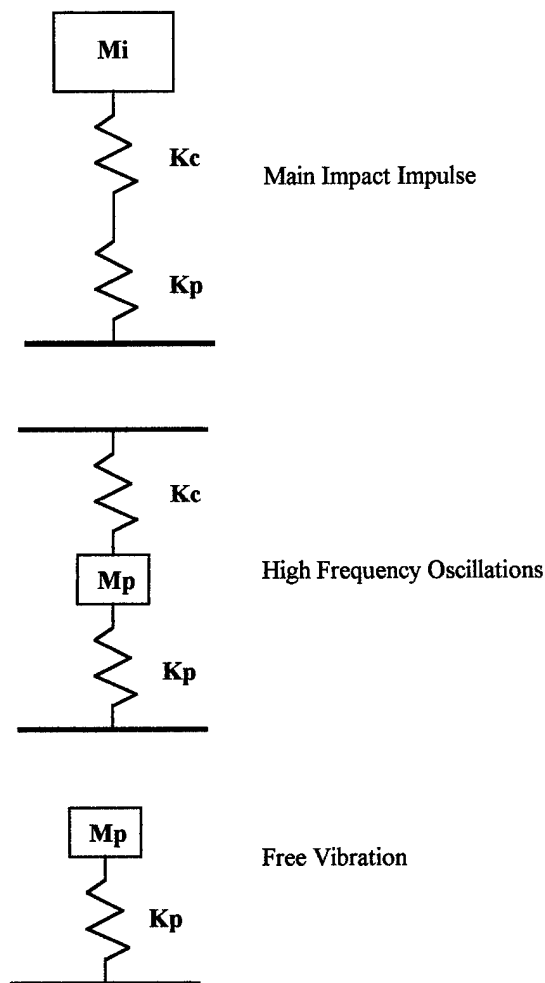
constrained by K_c and K_p. After impact, the panel responds to free vibration according to its mass and stiffness. Each of these components can be readily observed in Figs 5 and 6.

Figure 8 compares force–time histories for an undamaged 3-ply laminate subjected to an incident energy of 0.384 J for unfiltered data and data filtered

using the low pass filter and a cut-off frequency of 3.5 kHz. There are very few high frequency oscillations in the unfiltered data and the filtered data closely represents the expected response. At the start of the impact event there are a few high frequency oscillations. These initial dynamic effects are thought to be associated with the low mass of the panel and induce a
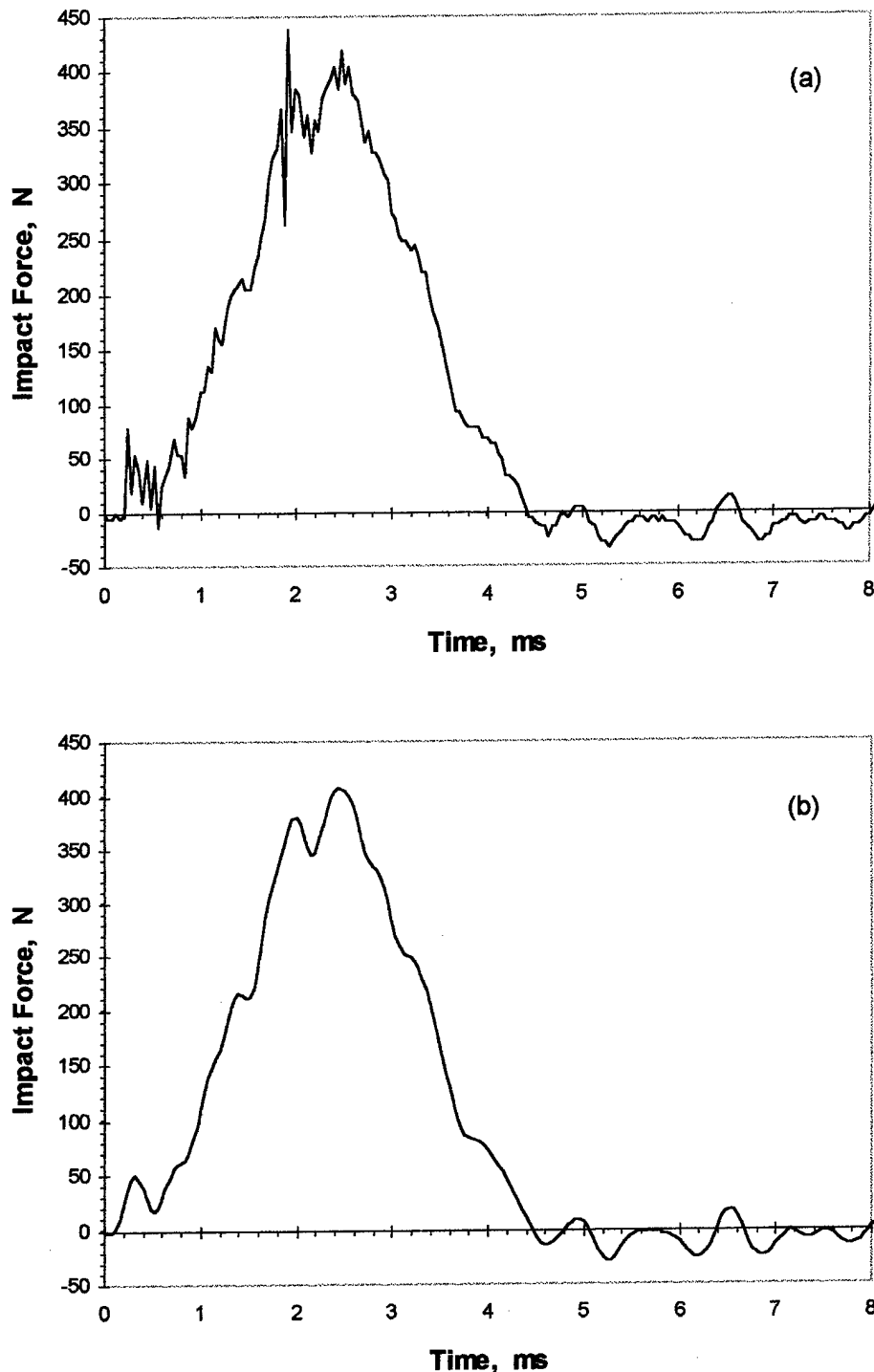
Fig. 8. Force–time plots for an impact energy of 0.384 J for (a) unfiltered data and (b) filtered data.

small spring-back of the panel. A similar, but more noticeable, response is observed from the numerical solution of the model [see Figs 5 and 6(a)]. The influence of the impact force during the initial stages of the impact event and the effect of oscillations throughout it are discussed in detail by Cheresh and McMichael [7]. However, it should be noted that the initial or inertial load identified by them is more likely to be associated with plates of much higher mass and stiffness than our thin panels.

Increasing the impact energy to induce damage causes large high frequency oscillations as shown in Fig. 9(a) for the unfiltered response of a 3-ply laminate subjected to an energy of 1.080 J. This incident kinetic
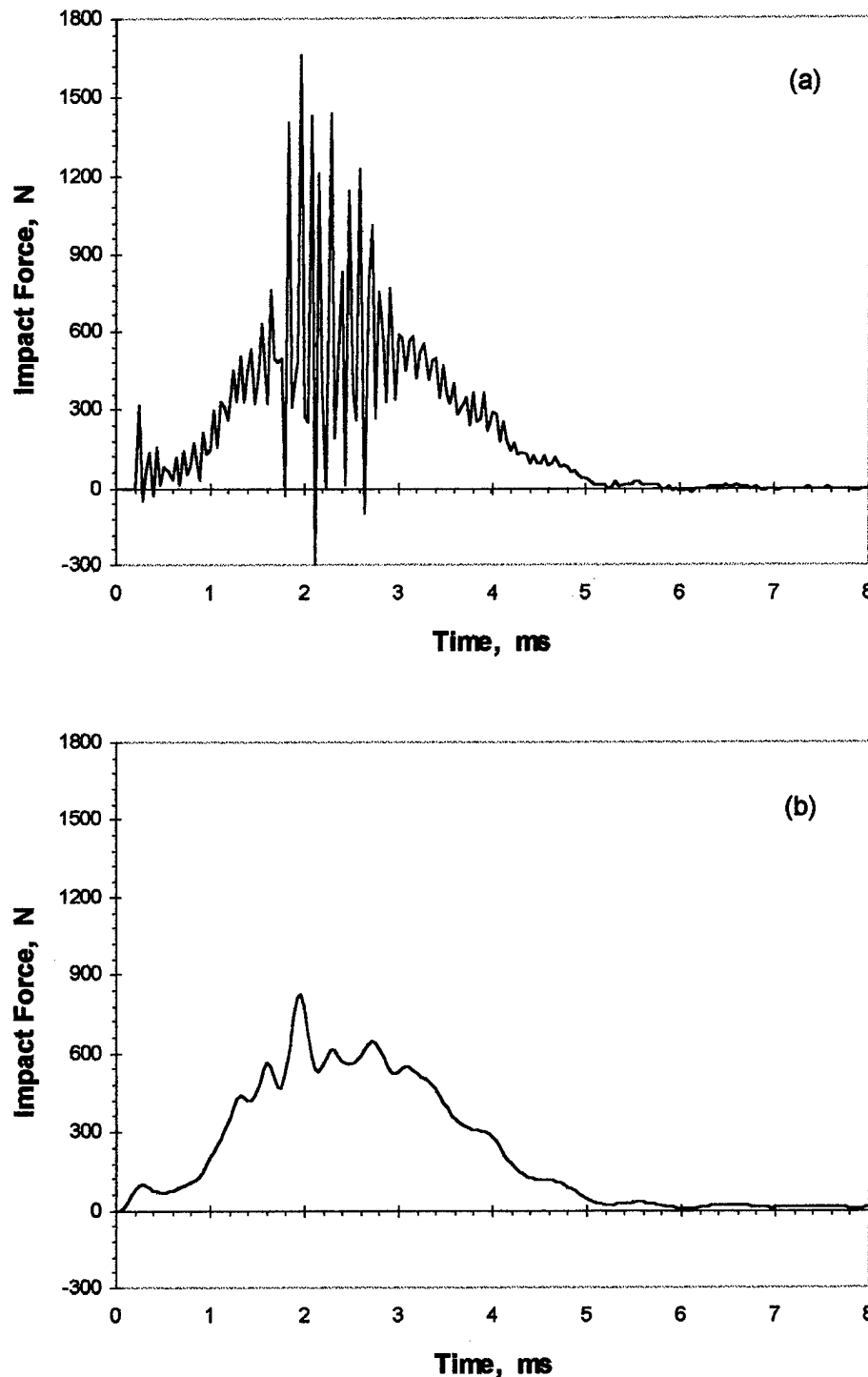
Fig. 9. Force–time plots for an impact energy of 1.080 J for (a) unfiltered data and (b) filtered data.
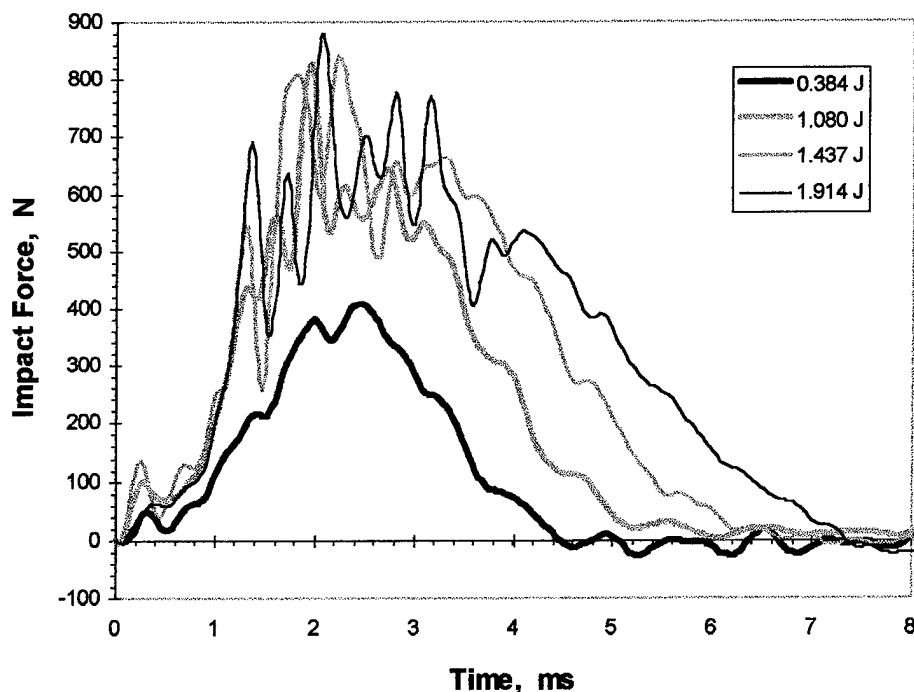
Fig. 10. Force–time plots of impacts at increasing levels of incident kinetic energy.

energy produced a projected delamination area of approx. 40 mm² and a total backface crack length of about 8 mm [12]. With filtering of the data via the low pass filter at a cut-off frequency of 3.5 kHz the average peaks of the high frequency oscillations are observed to be superimposed on the main impulse as shown in Fig. 9(b). The effect of increasing impact energy on the force–time history for 3-ply laminates is shown in Fig. 10. The data has again been filtered via the low pass filter at a cut-off frequency of 3.5 kHz. The profiles show that the high frequency oscillations commence at shorter times as increasing impact energies produce more damage. As the perforation threshold energy is approached the oscillations become larger, with greater variations, and extend over a wider plateau. Whilst our model at present does not account for any damage during impact it still allows us to make an initial assessment of the filtering of the data with some confidence. Although we have employed the same level of filtering for all the tests reported here, Cain [8] has stated that there is unlikely to be a universal filter suitable for all impact tests. Therefore, the use of models for determining the level of filtering of impact test data appears to be justified for the immediate future. Clearly, an international standard for processing of impact test data would be most welcome, especially by newcomers to this field of study.

Most spring-mass models predict force and displacement histories in the form of a half sinewave, especially

those with one degree-of-freedom. Models with two degrees-of-freedom, without damping, often superimpose inertial effects on the main impact impulse, especially for plates of high mass and stiffness as identified by Shivakumar et al. [10]. Our model, with three degrees-of-freedom, and damping, is able to give a reasonable prediction of the impact response of thin CFRP panels with circular clamping. We are presently trying to improve its effectiveness by introduction of non-linear elements at the local contact interface and global panel stiffness. We will then introduce a damage parameter into the model and try to refine the detail of this model via a more complex and sophisticated finite element model.

6. Conclusions

A spring-mass lumped-parameter mechanical model has been developed which can adequately describe the dropweight impact response of thin CFRP panels with circular clamping if there is little or no damage induced in the panel by the impact. The model is able to identify the separate influences of the main impact impulse, high frequency oscillations and free vibrations. Furthermore, it is able to distinguish the difference in response in thin and thick laminates. The use of the model allows for effective digital filtering of signals from dropweight impact tests. For all the tests reported here filtering was via a low pass filter with a cut-off

frequency of 3.5 kHz and a transition width of approx. 1 kHz.

The model also enables interpretation of high frequency components in the accelerometer signal. At the start of the impact event they are associated with the low mass of the panel whilst approaching the peak force they indicate the creation of damage in the panel during impact. Furthermore, the onset of the latter type of high frequencies appears to indicate the onset of damage in the panel. As the perforation threshold energy is approached these oscillations become larger and extend over a wider plateau.

Acknowledgements

References

[1] Lagace PA, Ryan KF, Graves MJ. Effect of damage on the impact response of composite laminates. AIAA Paper 91-1079-C, 1991:1137–43.

[2] Dorey G. Impact damage in composites — development, consequences and prevention. 6th International Conference Materials, London. Oxford: Elsevier Applied Science, 1987;3:3.1–3.26.

[3] Sierakowski RL, Newaz GM. Analytical methodology. In: Damage tolerance in advanced composites, ch.2. Technomic Publishing Co, 1995.

[4] Robinson P., Davies G.A.O. Impactor mass and specimen geometry effects in low velocity impact of laminated composites. Int J Impact Engng 1992;12(2):189–207.

[5] Curtis PT. Crag test methods for the measurement of the engineering properties of fibre reinforced plastics. Technical report 88012, Royal Aerospace Establishment, February 1988.

[6] Anon. Standard test for toughened resin composites. NASA reference publication 1092, 1982.

[7] Cheresh M.C., McMichael S. Instrumented impact test data interpretation. ASTM STP 1987;936:9–23.

[8] Cain PJ. Digital filtering of impact data. ibid 81–102.

[9] Lifshitz J.M., Gov F., Gandelsman M. Instrumented low-velocity impact of CFRP beams. Int J Impact Engng 1995;16(2):201–215.

[10] Shivakumar K.N., Elher W., Illg W. Prediction of impact force and duration due to low-velocity impact on circular composite laminates. Trans ASME J Appl Mech 1985;52:674–680.

[11] Kumar M, Found MS, Howard IC. A dropweight instrumented impact test to compare the effect of single and multiple impacts on CFRP. In: Found MS, editor, Proceedings of the 2nd International Seminar on Experimental Techniques and Design in Composite Materials. Sheffield: Sheffield Academic Press, 1995:84–101.

[12] Found M.S., Howard I.C., Paran A.P. Size effects in thin CFRP panels subjected to impact. Comp Struct 1997;38:599–607.

[13] Found MS, Howard IC, Paran AP. Impact behaviour of stiffened CFRP sections. Comp Struct (in press).

[14] Stearns SD, Hush DR. Digital signal analysis, 2nd edn. Englewood Cliffs: Prentice Hall, 1990.

Failure mechanisms on composite specimens subjected to compression after impact

M. de Freitas*, L. Reis

Departamento de Engenharia Mecânica, Instituto Superior Técnico, Av. Rovisco Pais, 1096 Lisboa Codex, Portugal

Abstract

Composite panels are widely used in aeronautic and aerospace structures due to their high strength/weight ratio. The stiffness and the strength in the thickness direction of laminated composite panels is poor since no fibres are present in that direction and out-of-plane impact loading is considered potentially dangerous, mainly because the damage may be left undetected. Impact loading in composite panels leads to damage with matrix cracking, inter-laminar failure and eventually fibre breakage for higher impact energies. Even when no visible impact damage is observed at the surface on the point of impact, matrix cracking and inter-laminar failure can occur, and the carrying load of the composite laminates is considerably reduced. The greatest reduction in loading is observed in compression due to laminae buckling in the delaminated areas. The objective of this study is to determine the mechanisms of the damage growth of impacted composite laminates when subjected to compression after impact loading. For this purpose a series of impact and compression after impact tests were carried out on composite laminates made of carbon fibre reinforced epoxy resin matrix. An instrumented drop-weight-testing machine and modified compression after impact testing equipment were used together with a C-scan ultrasonic device for the damage identification. Four stacking sequences of two different epoxy resins in carbon fibres representative of four different elastic behaviours and with a different number of interfaces were used. Results showed that the delaminated area due to impact loading depends on the number of interfaces between plies. Two buckling failure mechanisms were identified during compression after impact, which are influenced more by the delamination area than by the stacking sequence. © 1998 Elsevier Science Ltd. All rights reserved.

1. Introduction

Impact performance is a particularly important consideration in the design of components made from laminated composite materials. In aircraft applications the components have to survive low energy impacts from dropped tools and rough handling during maintenance, intermediate energy impacts from runway stones and bird strikes, and for military aircraft high-energy weapon attack. Low energy impact is considered potentially dangerous mainly because the damage might be left undetected. The low energy impact of CFRP laminates creates damage which may involve indentation, matrix cracking, fibre matrix debonding, delamination, inter-laminar failure and eventually fibre breakage for higher impact energies. This is due to the stiffness and the strength in the thickness direction of laminated composite panels, which is poor since no fibres are present in that direction. In many situations [1–3], the level of impact at which visible damage is formed is much higher than

the level at which substantial loss of residual properties occurs. Even when no sign of impact damage is observed at the surface of impact (energies below Barely Visible Impact Damage, BVID), matrix cracking and inter-laminar failure can occur. The delaminations at low energies cause little effect on the tensile strength but significantly reduce the compressive strength. Visible damage occurs if an impact is above a threshold impact energy, which depends on the laminate stiffness [4,5]. The greatest reduction in after-impact loading is observed in compression due to laminae buckling in the delaminated areas and therefore compression after impact tests has been proposed in order to quantify the compressive reduction

Table 1
Elastic properties of laminae

Material	E_1 (GPa)	E_2 (GPa)	G_{12} (GPa)	G_{13} (GPa)	G_{23} (GPa)	v_{12}
IM7/977-2	160.0	9.0	6.9	3.8	4.3	0.20
T800/5245C	161.0	8.9	5.9	2.2	3.7	0.20

*Corresponding author.

Table 2
Elastic properties of laminates

Material	Stacking	E_x (GPa)	E_y (GPa)	G_{xy} (GPa)	G_{xz} (GPa)	G_{yz} (GPa)	v_{xy}
IM7/977-2	B	62.1	62.1	24.2	4.0	4.0	0.28
	C	61.9	61.9	24.1	2.7	2.7	0.28
	D	63.8	41.7	31.5	2.8	2.0	0.49
	E	83.0	37.6	23.8	4.8	4.7	0.46
T800/5245C	B	61.2	61.2	23.5	2.1	2.1	0.3
	C	62.8	62.8	24.5	2.0	2.0	0.28
	D	60.8	39.7	30.0	2.4	3.3	0.52
	E	82.3	37.6	23.6	1.9	2.7	0.46

strength. Considerable research [6–9] has, therefore, been devoted to analysing the impact properties and post-impact compression behaviour with a view to improving impact damage tolerance, but detailed experimental examinations of CAI tests have not been extensively performed [10].

The objective of the present study is to describe the actual experimental techniques that are used on low and intermediate energy impact testing on laminated composite materials, the non-destructive techniques used to determine the damaged areas through the thickness and the delamination growth occurring during compression on delaminated specimens. For this purpose two different materials, carbon fibres in epoxy resin and four different stacking sequences were used. A wide range of impact energies have been

applied to specimens according to the proposed standards (Boeing, Airbus Industries) testing using an instrumented drop weight testing machine. Modified compression after impact testing equipment, similar to that proposed on the referenced standards, was used for the determination of the residual strength of the specimens. This allowed a better understanding of the buckling behaviour of the specimen associated with the delamination areas.

2. Materials and specimens

Composite panels were made of unidirectional prepregs of carbon fibres IM7 on an epoxy resin 977-2 from Fiberite Co., with a nominal thickness of 0.135 mm for 60% of volume fibre (V_f), and carbon fibres T800 on an epoxy resin 5245C from CYTEC Co., with a nominal thickness of 0.190 mm for 60% V_f.

Four stacking sequences with 24 plies were used, for both composite materials:

Lay-up B: $[-45_3/0_3/+45_3/90_3]_s$
Lay-up C: $[-45/0/+45/90/-45_2/0_2/+45_2/90_2]_s$
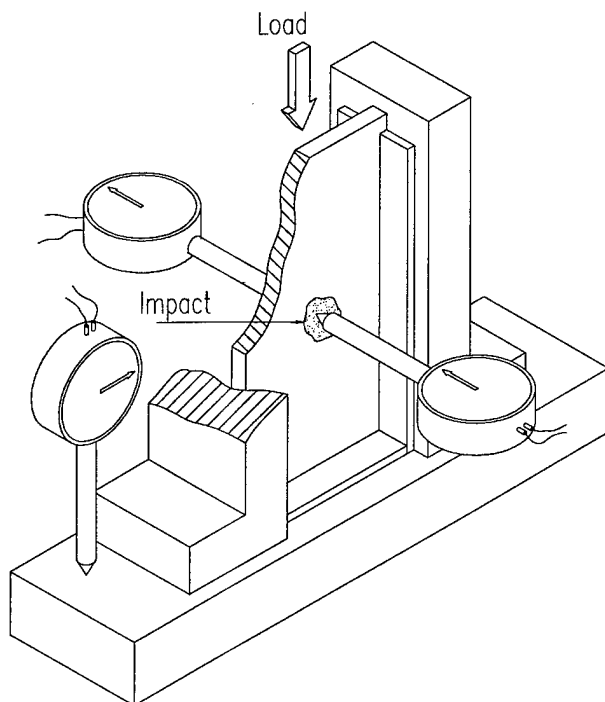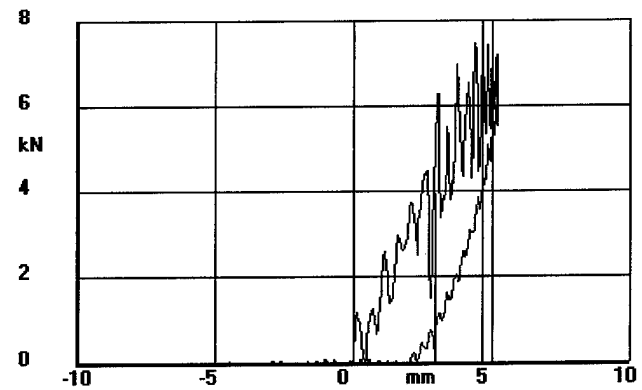
a)
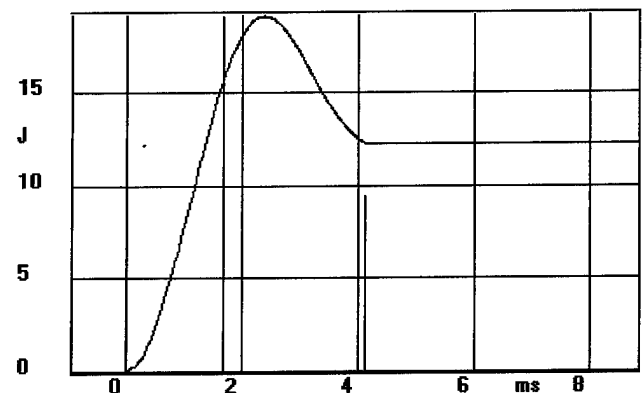
b)

Fig. 2. Impact test graphs: (a) force versus deflection; (b) energy versus time.

Fig. 1. Instrumented compression after impact (CAI) testing fixture

Lay-up D: $[-45_4/+45_4/0_3/90]_S$
Lay-up E: $[-45_3/+45_3/0_5/90]_S$

The elastic properties of the individual laminae and global properties for each panel are listed in Tables 1 and 2, respectively, and were obtained by identification of the material properties using experimental vibration data associated with optimisation techniques [11]. Directions 1 and 2 are respectively the longitudinal and transverse directions of each laminae and x and y are respectively the 0° and 90° directions of the laminate. Lay-ups B and C correspond to a quasi-isotropic stacking sequence and consequently identical laminate properties are obtained for both x and y directions, but a more damage tolerant stacking sequence is expected for lay-up C since it has an increased number of interfaces [12]. In lay-ups D and E, different global elastic properties are obtained for each direction due to the different number of layers in the 0° and 90° directions. The advantage of using a lower number of interfaces is related with numerical modelisation, which will not be presented here.

Specimens with dimensions of 150×100 mm were cut from the panels, according to the AITM 1.0010

(Airbus Industries Testing Method). For each lay-up, some specimens were cut with the 0° direction aligned with the 100-mm width (lay-ups B, C, D and E) and other specimens were cut with the 0° direction aligned with the 150-mm length (lay-ups B*, C*, D* and E*).

3. Experimental procedure

3.1. Impact testing

An instrumented falling weight impact machine was used where the different nominal impact energies were obtained through discrete masses of 2–10 kg and a variable height up to 2 m.

The instrumentation associated with the impact machine measures the force and time during impact. Force is measured discretely in time, through a force transducer just above the impactor indentor. The system also provides for the measurement of the velocity at the moment of impact, by measuring the time it takes a flag of known width to traverse a point. The velocity during impact is calculated by integrating acceleration over time, where the acceleration is given by the force felt by the drop mass, divided by its mass.

a)   b)

1- interface -45°/+45°
2- interface +45°/0°
3- interface 0°/90°
4- interface 90°/0°
5- interface 0°/+45°
6- interface +45°/-45°
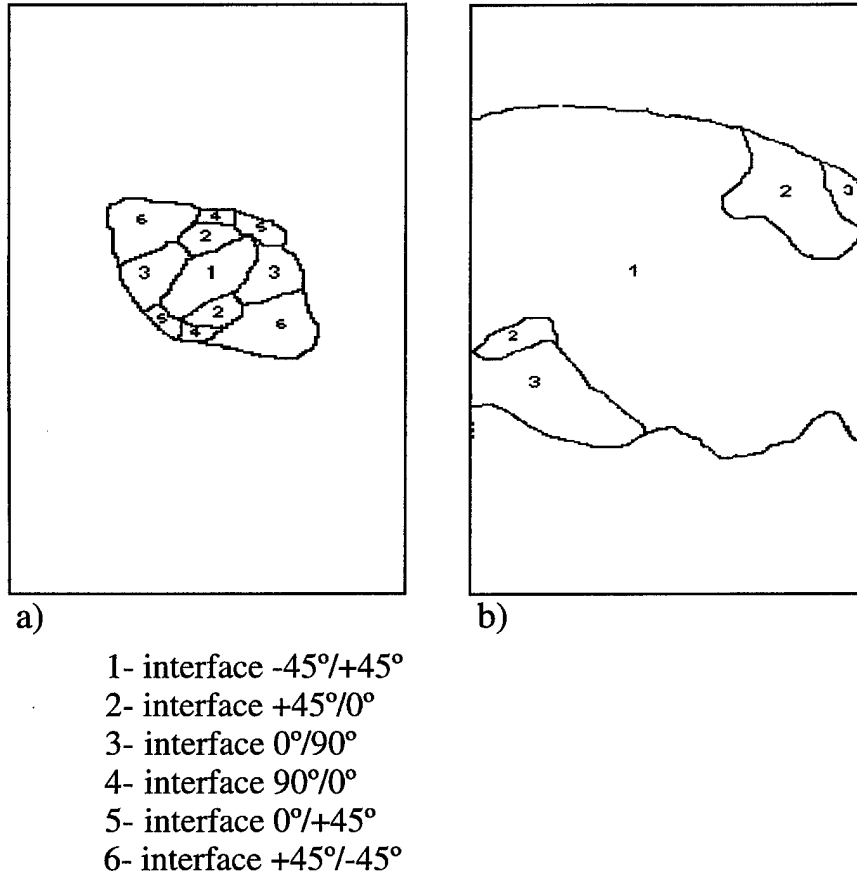
Fig. 3. Delamination pattern for specimen D*11, T800/5245C: (a) after impact; (b) after CAI.

The calculated velocity is then used to derive the displacement of the impactor during impact (and consequently the deflection of the specimen) using further integration. The energy is calculated by integrating force over distance. With this measurement and calculation procedure, not only the actual impact energy but also the absorbed energy by the specimen were calculated through the energy/time curve.

The impactor used was a hemi-spherical one made of steel with a diameter of 16 mm. The specimens were clamped in a standard impact testing fixture with an open window of 125 × 75 mm, according to Airbus Industries Test Method (AITM 1.0010). After impact the permanent indentation depth of the specimens was measured. Through the non-destructive methods the delaminated area was identified and measured.

3.2. Delamination area

For the delamination pattern visualisation A, B and C-scan NDI ultrasonic technology with a pulse-echo and an immersion scanning method, Physical Acoustics, was used, with the following C-scan data:

scan frequency: 5 MHz

scan speed (X-axis): 30 mm/s
index axis: Y-axis
scan interval index: 0.05 mm

There are two kinds of data processing in pulse-echo C-scanning: echo level view amplitude (.AMP) and time of flight (.TOF) view. The latter data can be converted into a delamination depth view through the transverse sound velocity in CFRP laminates. Therefore, the identification of delamination interfaces is easily identified and the measurement of the respective area was carried out with image processing equipment. For the purpose of this study the delamination area was considered as the projection on the specimen plane of the area delaminated considering all the delaminated interfaces, which obviously has a lower value if the delamination area was considered as the sum of all the delaminated areas.

3.3. Compression after impact

Compression after impact tests of the specimens were carried out on a universal testing machine, in displacement control with a velocity of 0.5 mm/min using the testing fixture described in the Airbus testing

a)   b)

1- interface -45°/+45°
2- interface +45°/0°
3- interface 0°/90°
4- interface 90°/0°
5- interface 0°/+45°
6- interface +45°/-45°
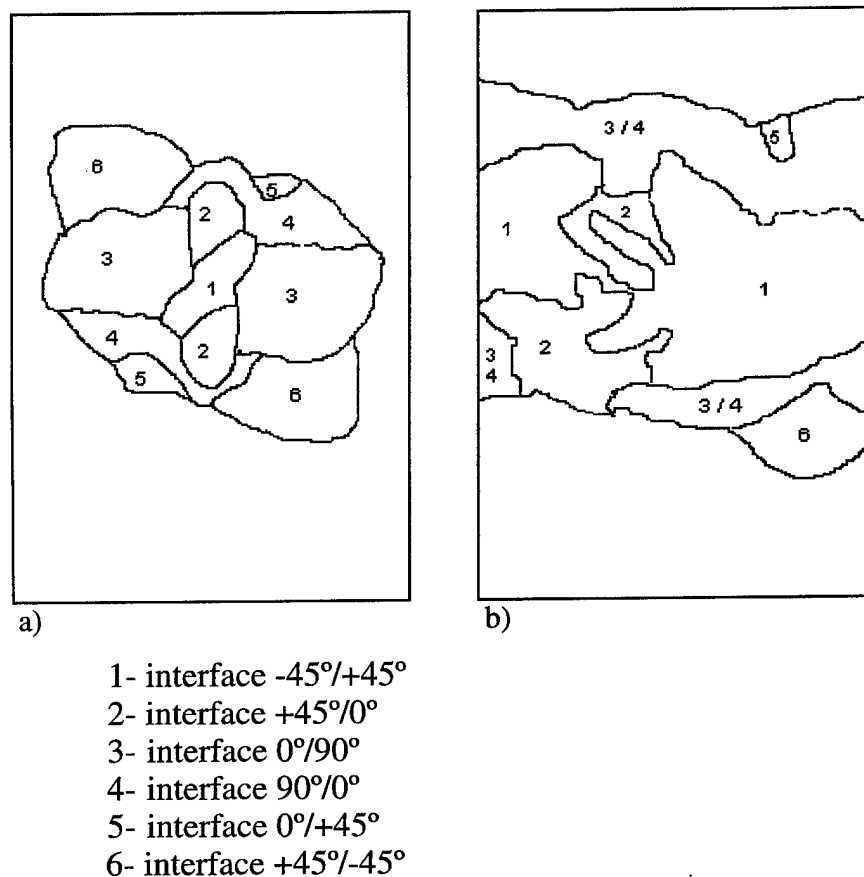
Fig. 4. Delamination pattern for specimen D*13, T800/5245C: (a) after impact; (b) after CAI.

procedure (AITM 1.0010). In this fixture and to prevent global buckling during compression, the specimens are clamped at both ends and simply supported at the side edges. In order to establish the buckling behaviour of the delaminated area during testing, up to final failure, two LVDTs were attached to the specimen: one at the centre of the impact zone and the second one at the opposite side. A third LVDT was used to monitor the vertical displacement of the specimen during the test, in order to obtain, with the load cell data, the load/displacement curves. A schematic view of the instrumented compression after impact (CAI) testing fixture, with a specimen mounted

and the three LVDTs in testing position, is shown in Fig. 1.

4. Results and discussion

A wide range of impact energies around the Barely Visible Impact Damage energy level (determined as the energy that causes a permanent indentation of 0.3 mm) were selected as a mean for creating a wide range of delaminated areas. In the present paper the analysis of damage growth will be analysed, therefore, only limited data will be presented. Further analysis

1- interface -45°/+45°
2- interface +45°/0°
3- interface 0°/90°
4- interface 90°/0°
5- interface 0°/+45°
6- interface +45°/-45°
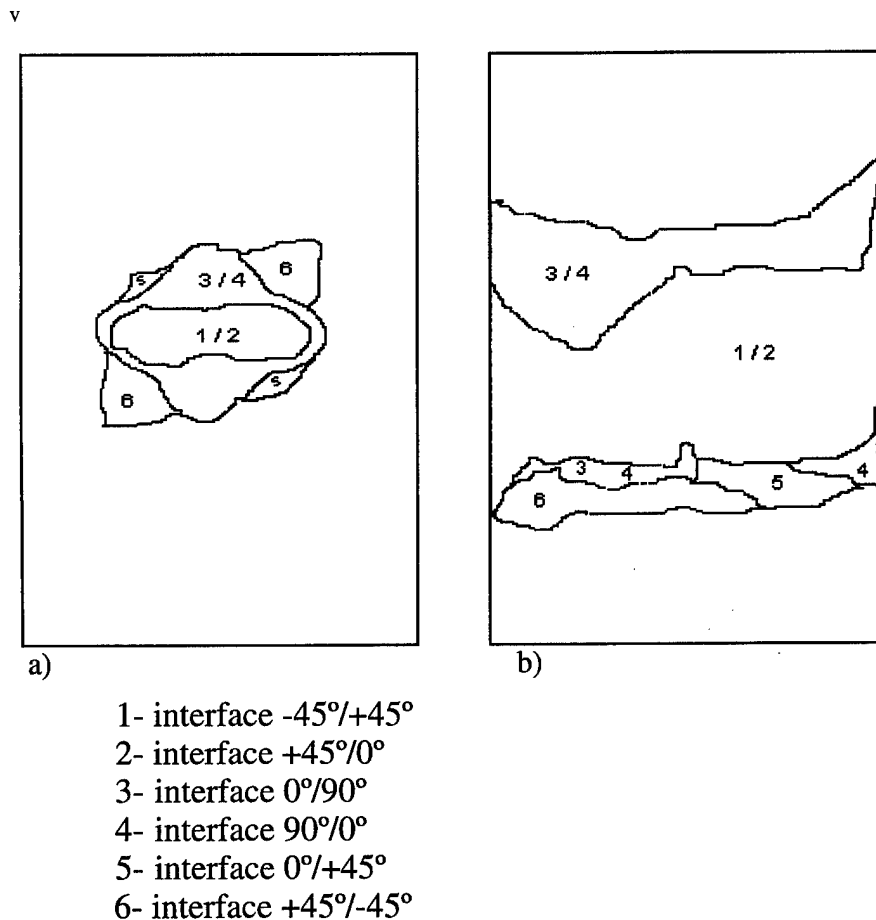
Fig. 5. Delamination pattern for specimen E8, T800/5245C: (a) after impact; (b) after CAI.

Table 3
Test results for three specimens

Impact test							CAI test		
Specim	E_{imp} (J)	E_{abs} (J)	δ_{max} (mm)	F_{max} (kN)	Delam. (mm^2)	Ind. (mm)	F_{max} (kN)	Back displ.	Front displ.
D*11	4.0	2.8	1.92	3.47	1332	0.15	110.25	+	−
D*13	13.2	9.3	4.05	5.69	5295	0.29	68.60	+	+
E 8	6.2	4.9	2.48	4.01	2105	0.25	61.25	+	−

such as delamination area as a function of impact energy and compressive residual strength can be found in Ref. [12]. A typical example of the graphs obtained during impact tests on the drop-weight testing machine is presented in Fig. 2(a) and (b), respectively, for the load/deflection and energy/time data. With the energy/time data, it is possible to monitor not only the energy required for the test, initially defined simply by the product of the weight and the drop height, but also the actual energy absorbed by the specimen by integrating the force over the distance during the time of contact between the indentor and the specimen.

The delamination patterns were then measured through the C-scan method. Three typical examples of converted TOF views of the delamination viewed from the impact side for the material T800/5245C are presented for lay-up D* in Figs 3 and 4 for low and BVID energy levels, respectively, and in Fig. 5 for lay-up E and low energy level ((a) after impact and (b)
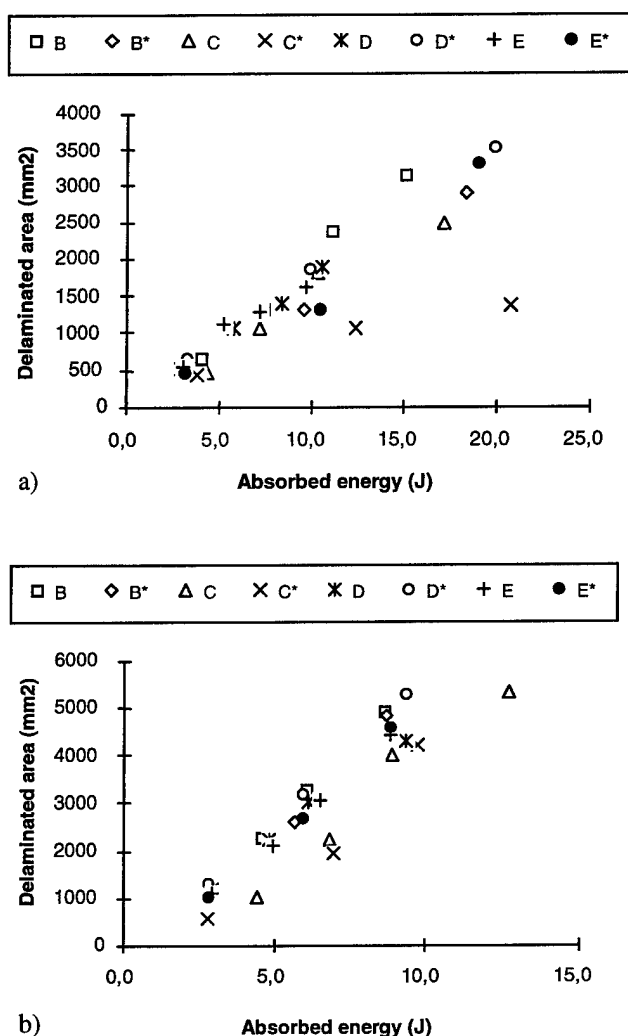
a)

after compression after impact). The results of impact for each specimen of the previous figures are given in Table 3, where E_{imp} and E_{abs} are the impact and absorbed energy, F_{max} and δ_{max} are the maximum force and maximum deflection, and Del. and Ind. are the delaminated area and permanent depth indentation, respectively. Table 3 also presents the compression after impact tests results where F_{max} is the residual strength of the specimen and back and front displ. are the positive (+) and negative (−) out-of-plane displacements. From the knowledge of both the stacking sequence and the delamination pattern for each specimen, it is possible to identify the interfaces of the delamination in order to clearly observe the damage growth. The delamination patterns of the figures clearly show that the damaged area is smaller for the upper plies (impact side) than the damaged area for the lower plies, i.e. the delamination takes the form of a cone-like shape with the delamination identified for each interface between the plies. It is easily observed that the ply direction influences the delamination shape. The delamination is obviously between two plies and the shape of the delaminated area for each interface between two plies is more pronounced in the ply orientation, which is at a larger distance from the impact zone. For example, on the specimen impacted at BVID energy level of lay-up D*1 $[-45_4/+45_4/0_3/90]_s$ where the 0° direction is aligned with the 150-mm length (presented in Fig. 4), the delamination on interface no. 1 has the +45° orientation, on interface no. 2 the 0° orientation is observed, and so on, in a total of six delamination planes corresponding to the same number of interfaces. For lay-up E, presented in Fig. 5, which has a lay-up shifted 90°, it is easily observed that the delamination interfaces also have a shifted orientation. An increased number of interfaces will, therefore, decrease the projected delaminated area, which was observed on the specimens of lay-ups C and C* when compared with the other stacking sequences, as shown in Fig. 6(a) and (b), respectively, for materials IM7/977-2 and T800/5245C.

Laminae buckling and the instrumented CAI testing fixture, which helped to identify the different mechanisms, always obtained the failure of the specimens due to CAI. In Fig. 7(a) and (b), the compressive load is plotted as a function of both out-of-plane displacements measured by the LVDT attached to the impact side (front displacement) and on the opposite side (back displacement) and represent the most dominating buckling failure mechanism observed. In Fig. 7(a) both displacements have the same direction, the direction of the impact deflection (considered here as positive displacement), while in Fig. 7(b) the displacements have opposite directions, the back side displacement has the same direction as the deflection during impact but the front displacement has an

b)

Fig. 6. Delamination area after impact: (a) material IM7/977-2; (b) T800/5245C.

opposite direction (negative displacement). This behaviour is related to the permanent indentation depth obtained during impact, which leads to a misalignment of the specimen, and therefore depends on the impact energy and the delaminated area. In Fig. 8(a) and (b), both the maximum out-of-plane displacements (front side and back side) are plotted as a function of the absorbed energy for all the specimens and stacking sequences for T800/5245C and IM7/977-2 materials, respectively. Despite the strong scatter of the data it is clear from Fig. 8(a) that the specimens of lower impact energies have a buckling failure similar to Fig. 7(b), while the specimens with higher impact

energies have a buckling failure behaviour similar to that observed in Fig. 7(a). A similar behaviour is shown in Fig. 8(b) representing the results for the specimens of IM7/977-2. Since these latter specimens are thinner than the previous ones (nominal thickness of 3.24 mm for IM7/977-2 and 4.56 mm for T800/5245C) and present much smaller delaminated areas than the former ones for the same absorbed energy, due to a higher toughness of the epoxy resin, it seems that the thickness has no influence for these specimens.

The specimen with the lay-up D* (Fig. 4) was impacted with an energy level very close to BVID energy level. A total of 35.3% of the specimen was
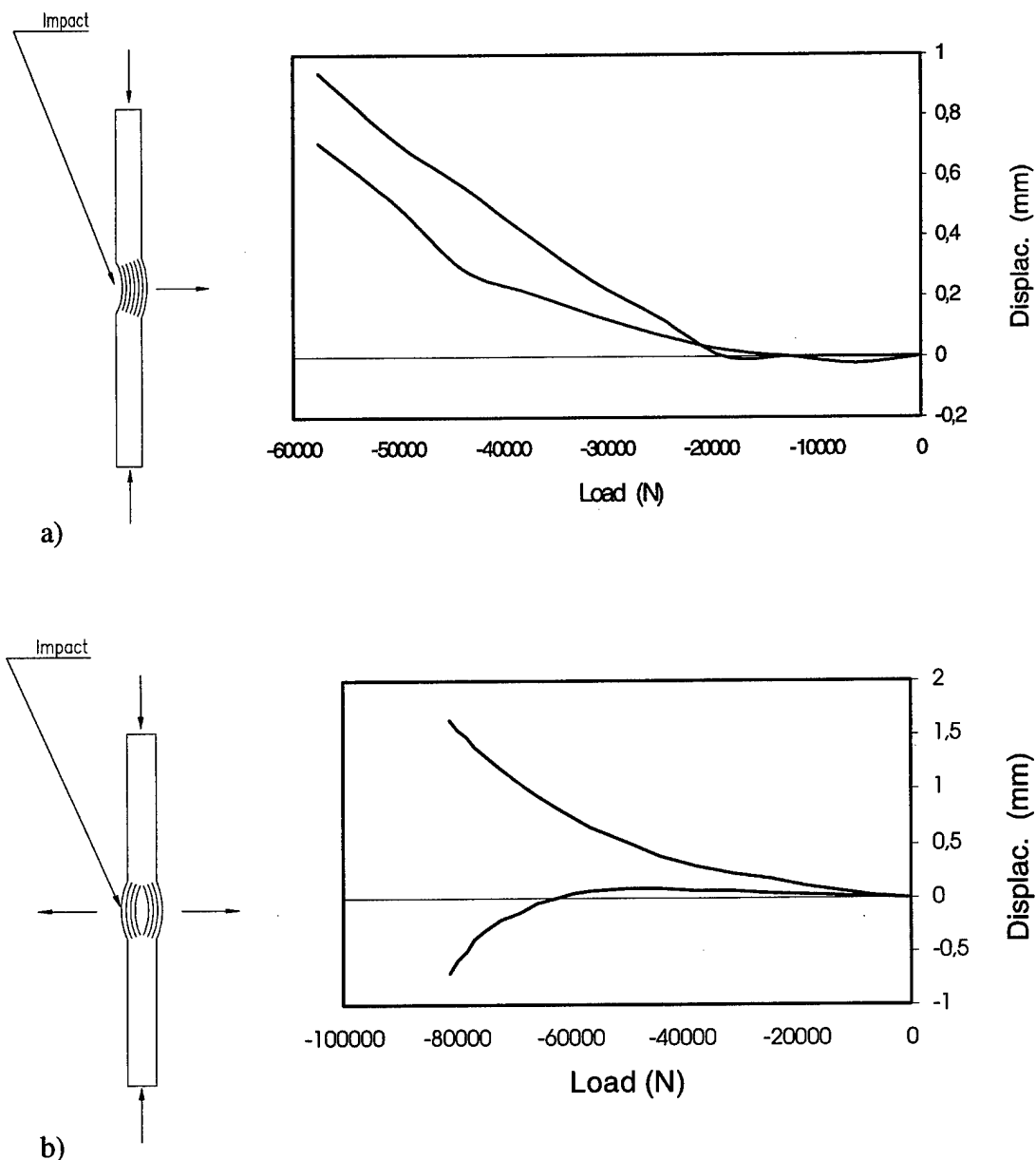
Fig. 7. Relation between compressive load and out-of-plane displacement in typical CAI tests: (a) positive front and back displacements; (b) negative front and positive back displacements.

delaminated. As shown in Fig. 4(a), interfaces 3, 4, 5 and 6 present very large delamination areas which are very close to the lateral surface of the specimen, therefore, no residual strength is expected for the damage growth in the width direction; only vertical damage growth will be resisting. On the opposite side, for the specimen with lay-up D* (Fig. 3) with a damaged area obtained for a lower energy level, only 8.9% of the total specimen area is delaminated. Interfaces 3 and 6 are the larger ones but are far from the lateral surface of the specimen. Therefore, when performing compression after impact testing the delamination will grow in both directions, lateral and vertical, and will contribute to the residual strength.

In order to identify the layers where the damage growth during CAI was observed, a C-scan was carried out on the specimens after compression after impact tests using the same ultrasonic procedure. The TOF

images of the specimens are presented in Figs 3(b), 4(b) and 5(b). The delamination interfaces were already identified after impact and therefore the delamination growth is easily detected by the comparison of the two C-scan images. The delamination growth in the width direction is observed for all delaminated interfaces for all the specimens and stacking sequences. But while for larger delaminated areas (Fig. 4) the damage growth is very small in this direction, for the other specimens it is very large. Regarding the damage growth in the vertical direction, one can identify that for the larger delamination areas of the specimen of Fig. 4 the damage growth is observed mainly on interfaces 3/4, 5 and 6. For lower delaminated areas the damage growth is similar for all the interfaces 1 to 6. This means that such a large damage growth for interface 1 is only possible for a laminae buckling failure with a negative out-of-plane displacement, which confirms the models and measurements presented earlier. Therefore, small delaminated areas have essentially a damage growth in both directions (width and length) and only a three-dimensional model can analyse this damage growth behaviour. For larger delamination areas, near the lateral borders of the specimen, the error incurred by analysing the damage growth with a bi-dimensional model is acceptable.

5. Conclusions

Low energy impact and compression after impact tests were carried out on laminate composite panels of two materials with four different stacking sequences and the following conclusions can be drawn:

- the delaminated area due to impact loading is a function of the absorbed energy and relatively independent of the stacking sequences used in this study, but is highly dependent on the number of interfaces;
- unstable damage growth was obtained by compression after impact due to a buckling mechanism in the delaminated area and two main buckling failure mechanisms were identified;
- the residual strength is influenced by the delaminated area which is a function of the impact energy but is also dependent on the distance between the delaminated area and the lateral borders of the specimens; this conclusion means that available bi-dimensional models for the calculation of delamination growth due to buckling can not be applied on specimens with a small percentage of delaminated area where a three-dimensional analysis is needed.
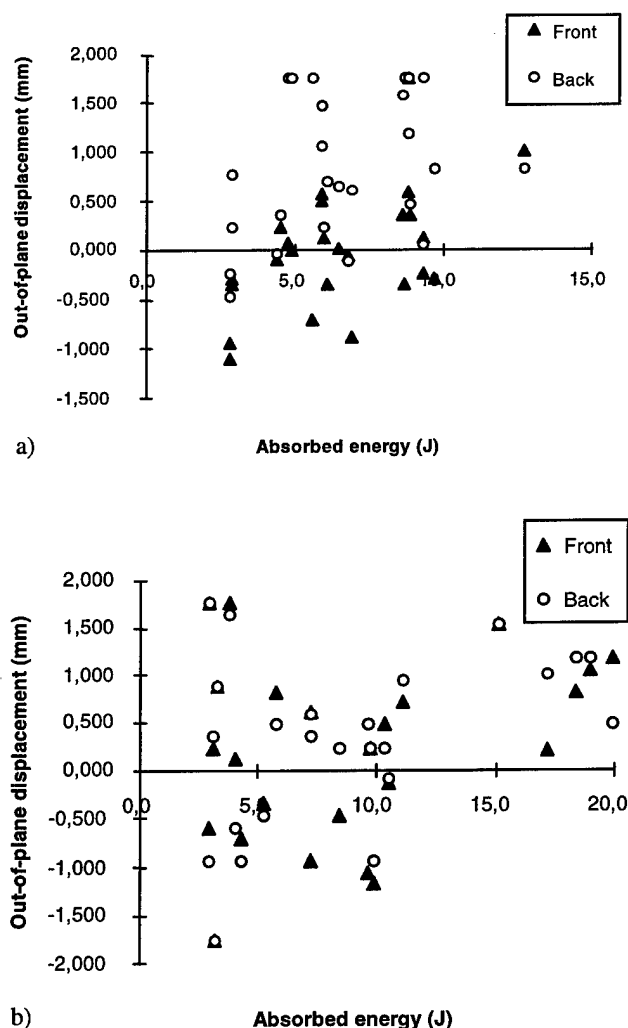
Fig. 8. Maximum out-of-plane displacements in CAI tests for all specimens as a function of absorbed energy: (a) T800/5245C; (b) IM7/977-2.

Acknowledgements

References

[1] Sjoblom PO, Hartness JT, Cordell TM. On low-velocity impact testing of composite materials. J of Composite Materials 1988;22:30–52.

[2] Wu HT, Springer GS. Measurements of matrix cracking and delamination caused by impact on composite plates. J of Composite Materials 1988;22:518–532.

[3] Delfone D, Poursartip A, Coxon BR, Dost EF. Non-penetrating impact behavior of CFRP at low and intermediate velocities. In: Martin RH, editor. Composites materials: fatigue and fracture, vol. 5, ASTM STP 1230. American Society for Testing and Materials, Philadelphia, 1995:333–50.

[4] Found MS, Howard IC. Single and multiple impact behaviour of a CFRP laminate. Composite Structures 1995;32:159–163.

[5] Liu S, Kutlu Z, Chang FK. Matrix cracking and delamination in laminated polymeric composites resulting from transversely concentrated loadings. In: Proceedings of the 1st International Conferences on Deformation and Fracture of Composites, Manchester, England, 25–27 March, 1991, pp. 30/1–30/7.

[6] Madan RC. Influence of low-velocity impact on composite structures. In: O'Brien TK, editor. Composites materials: fatigue and fracture, vol. 3, ASTM STP 1110. American Society for Testing and Materials, Philadelphia, 1991, pp. 457–75.

[7] Dost EF, Ilcewicz LB, Coxon BR. Effects of stacking sequence on impact damage resistance and residual strength for quasi-isotropic laminates. In: O'Brien TK, editors. Composites materials: fatigue and fracture, vol. 3, ASTM STP 1110. American Society for Testing and Materials, Philadelphia, 1991, pp. 476–500.

[8] Kinsey A, Saunders DEJ, Soutis C. Post-impact compressive behaviour of low temperature curing woven CFRP laminates. Composites 1995;26:661–667.

[9] Soutis C, Curtis PT. Prediction of the post-impact compressive strength of CFRP laminated composites. Composite Science and Technology 1995;56:677–684.

[10] Ishikawa T, Sugimoto S, Matsushima M, Hayashi Y. Some experimental findings in Compression-After-Impact (CAI) tests of CF/PEEK (APC-2) and conventional CF/EPOXY flat plates. Composites Science and Technology 1995;55:349–363.

[11] Araújo AL, Soares CMM, Freitas MJM. Characterization of material parameters of composite plate specimens using optimisation and experimental vibrational data. Composites: Part B 1996;27B:185–191.

[12] Reis L, de Freitas M. Damage growth analysis of low velocity impacted composite panels. In: Proceedings of the 9th International Conference on Composites Structures, Paisley, Scotland, 1997.

ELSEVIER

The use of experimentally-determined impact force as a damage measure in impact damage resistance and tolerance of composite structures

G. Zhou*

Department of Aeronautical and Automotive Engineering and Transport Studies, Loughborough University, Loughborough, Leicestershire LE11 3TU, UK

Abstract

An instrumented drop-weight impact rig, ultrasonic C-scan and CAI test rig form a basic experimental system needed for the quantitative investigation of impact damage resistance and damage tolerance assessment. It is shown that it is essential to have an impact rig designed with certain traits along with other selected impact conditions so that dominant damage mechanisms occurring during impact can be identified with the threshold forces of recorded impact force–time curves. The so-determined impact force data are used to study impact damage resistance. It is demonstrated that the ratio of measured threshold impact forces is a useful alternative to residual compressive strength usually used for damage tolerance assessment. This provides a fast and cheap technique without resort to complex and expensive CAI tests. © 1998 Elsevier Science Ltd. All rights reserved.

1. Introduction

Fibre-reinforced laminated composite structures may encounter impact loading either accidentally in their designed life or in an anticipated hostile service environment. A sufficient intensity of such a loading causes damage which affects not only structural response during loading but also reduces structural strength in subsequent static loading. Some well-cited cases are tool-dropping during assembly of aircraft components, runway stones during takeoff or landing of aircraft and use for light vehicles, to name just a few.

Before an evaluation of damage resistance and tolerance of composite structures can be properly carried out, the nature and principal characteristics of impact damage has to be clearly understood. A phenomenon of impact damage is generally very complex as is usually reflected in three aspects. First, impact damage appears in multiple forms of damage mechanisms such as matrix cracking, delamination and fibre breakage; this can occur at different stages of loading and is also likely to be due to different stress components so that these mechanisms may interact among themselves with one or two being dominant. Second, no single estab-

lished non-destructive testing technique exists for detecting and quantifying these damage mechanisms. Finally, the nature and extent of these damage mechanisms are affected, to different degrees, by some of a large number of parameters such as noseshape and mass of impactor, impact velocity, types of fibre and matrix, interfacial treatment, fibre volume fraction, layup, laminate geometry, boundary condition and even pre-stress. This is particularly so when impact velocity is low (1–10 m s^{-1}) with a non-deformable impactor and is further compounded by the lack of a widely acceptable test standard. Because of this complexity (also discussed in [1]) and a lack of clear understanding of the consequence of impact damage, the current allowable strain is limited to 0.3–0.4% so that their full weight-saving potential has not yet been fully realised. Obviously, an improvement in the allowable strain up to 0.6% would make composite structures more cost-effective thereby facilitating further exploitation of their potential. Therefore, the minimisation of this detrimental effect is crucial in cost-effective design and applications of composite structures. To this end, it is of vital importance to have a thorough understanding of impact response, damage and the static performance of damaged composite structures.

This paper demonstrates the development of a simple experimental scheme for assessing the effect of

*Tel.: 00 44 1509 223 434; Fax: 00 44 1509 223 946.

impact damage using impact force data measured at low impact velocities. Its overall objective is threefold. First, the major design considerations for an instrumented drop-weight impact rig are discussed and the characteristics of recorded impact responses from several fibre-reinforced composite plates are examined. Second, dominant damage mechanisms are confirmed by using ultrasonic C-scan and cross-sectioning and their characteristics are described. Finally, the damage measures for impact damage resistance and tolerance assessment of damaged composite structures are discussed.

2. Impact testing procedures and examination of impact damage

Due to the lack of an experimental standard, a wide variety of instrumented impact testing techniques such as swinging pendulum, drop-weight and rail-supported gun have been used [2–4] for low-velocity transverse impact, with an even greater variety of damage interro-

gation techniques [3–5]. The advantages of using an instrumented drop-weight impact rig are: (1) the initiation and development of damage occurring in laminates during impact may be identified from a recorded impact force–time history curve, as an instrumented impactor usually made of mild steel behaves very much like a rigid body compared to a composite laminate; (2) a greater number of impact parameters can be examined; and (3) it allows a very wide range of incident kinetic energies (IKEs) to be achieved by adjusting either drop height or impactor mass individually or both simultaneously.

2.1. Design considerations of drop-weight impact rig and test procedures

There are a large number of tailor-made impact rigs such as the one illustrated in Fig. 1, in addition to commercial versions (i.e. Dynatup, Rosand and CEAST Fractovis Mk series). Two crucial factors in the design of instrumented drop-weight impact rigs are
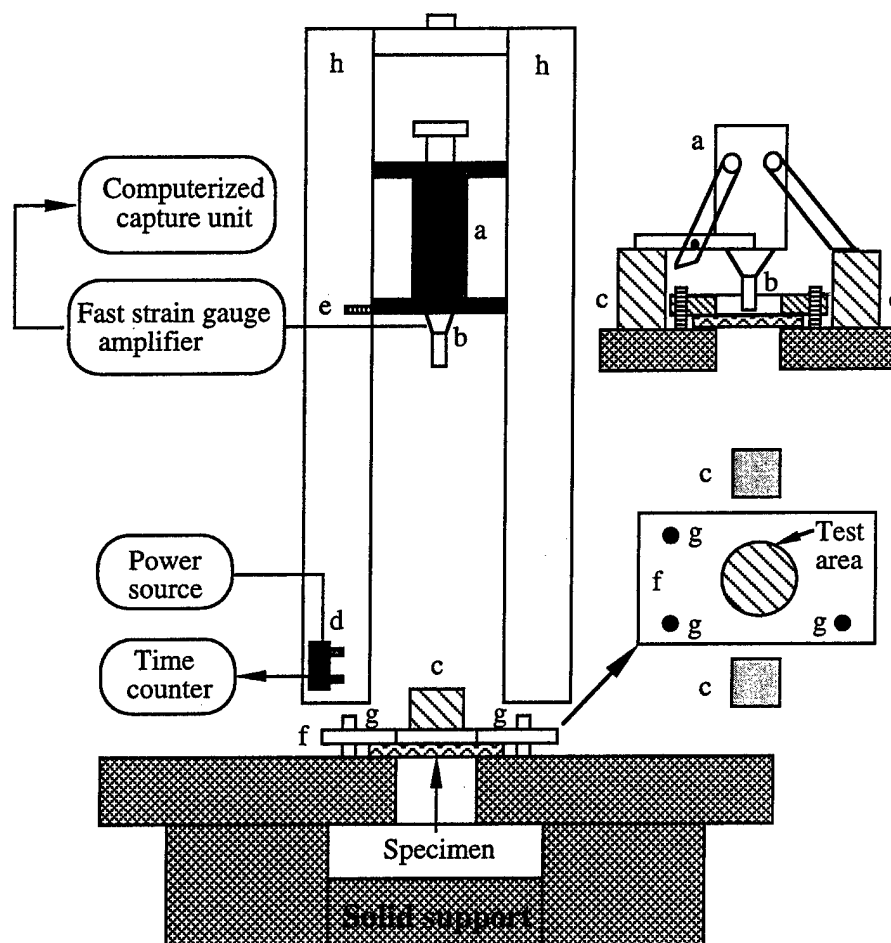
Fig. 1. Experimental set-up for drop-weight impact test: (a) impactor; (b) strain-gauged load cell; (c) rebound catch block; (d) photodiodes; (e) flag; (f) clamping device; (g) locking pin; (h) drop guide (detached from drop tower).

drop guide and instrumented impactor. A close obser-
vation of these rigs reveals that two design principles
for a drop-weight guiding have been used as shown in
Fig. 2, namely, double column-guide (i.e. Dynatup) and
double channel-guide, each could provide slightly
different impact responses even under similar impact
conditions. In the present impactor rig, the drop guide
through a pair of beams of channel section (see Fig.
2(b)) is used so that the impactor falls near freely
within two beams. Because the impactor is not in
intimate contact with the guiding beams, friction
during falling is minimised with additional plastic pads
engraved on the sides of the impactor. A built-in
rebound catch mechanism (see the top right inset in
Fig. 1) is usually needed for a heavy impactor, and its
design and practical implementation is quite involved.
A so-called instrumented impactor is in fact an
assembly of many components bolted together, namely,
a nose shaft (or tup), an instrumented shaft (with or
without an interior housing for instrumentation such as
a strain-gauged load cell or an accelerometer) and the
rest of the components as illustrated in Fig. 3. Its

design fixtures in addition to a drop guide and the
geometric characteristics of a target laminate have a
great influence over the characteristics of the impact
response, especially the amount of oscillation. In
general, the instrumented part should be as close as
possible to the nose of the impactor so that the
recorded impact response contains minimal distortion.
A nose shaft, however, should have sufficient length to
allow the deflection and even penetration of the target
laminate. Extensive experimentation in the early stage
of the present impactor design indicates that it is quite
desirable for a nose shaft and an instrumented shaft to
be machined out of one piece of solid material rather
than bolted together from two separate pieces. In the
latter case, the presence of an interface between a nose
shaft and an instrumented shaft is believed to be one
of the major design sources for significant oscillation in
impact response.

Target plates are made of woven roving E-glass/
polyester and S-glass/phenolic laminate systems.
Low-velocity (2–8 m s^{-1}) impact tests with IKEs
ranging from 15 to 3000 J were conducted using the
instrumented drop-weight test rig with a flat-ended
impactor, providing a force–time history. The details of
the experimental set-up, test procedures and the major
results are reported in [6–8]. A typical impact force–
time history curve is shown in Fig. 4.

Filtering of data is another important factor as the
amount of filtering affects the shape of the impact
force–time history curve so that the use of such a curve
for identifying dominant damage mechanisms becomes
extremely difficult. Nevertheless, filtering is often
carried out to reduce or eliminate high-frequency noise
or ringing so as to improve the readability of the data.
Although noise could mask the true mechanical
response, it is usually present because of the funda-
mental nature of impact dynamics. The complexity of
data filtering is discussed elsewhere [9]. It should be
recognised that experimental data could be distorted
by filtering unless the source of noise and its effect on
the data are well understood. Considerable caution
should be exercised should data filtering become neces-
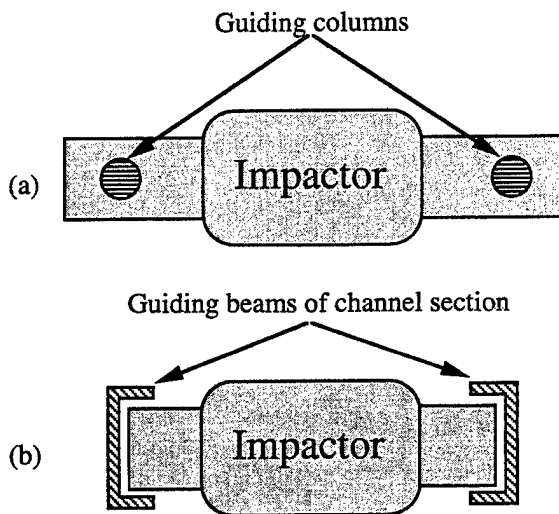
Fig. 2. Simplified illustrations of two different drop-weight guiding
principles for an instrumented impact test rig.
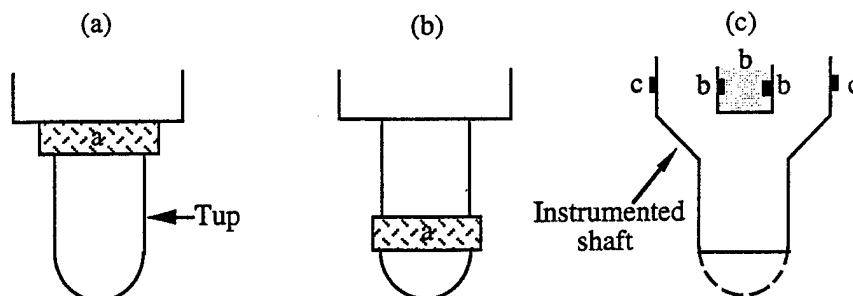
Fig. 3. Different designs of instrumented impactor: (a) accelerometer or force sensor and its housing; (b) interior strain-gauge instrumented load
cell (with housing); (c) exterior strain-gauge instrumented load cell.

sary, in particular if the characteristics of the filtered impact response curves are used for identifying damage mechanisms. In the present investigation, no data filtering was carried out.

2.2. Characteristics of impact damage mechanisms

The impact response of the composite plates is dominated by the aforementioned impact parameters. When an appreciable amount of damage occurs, the
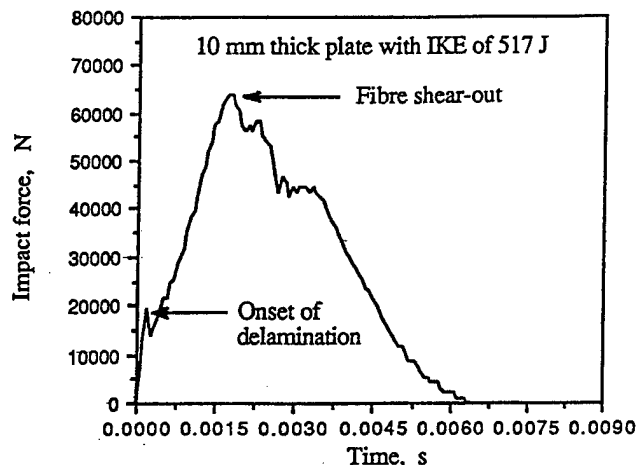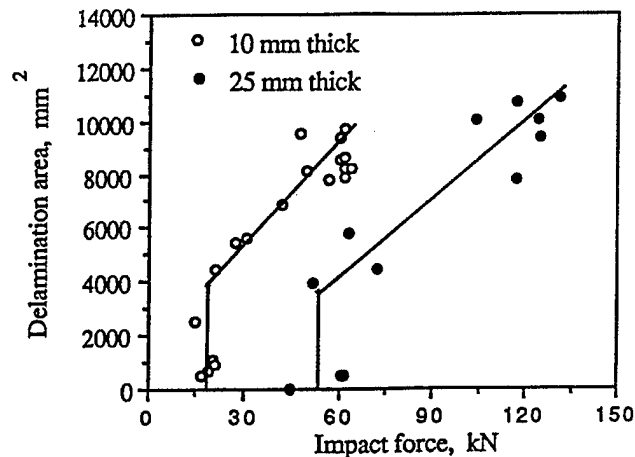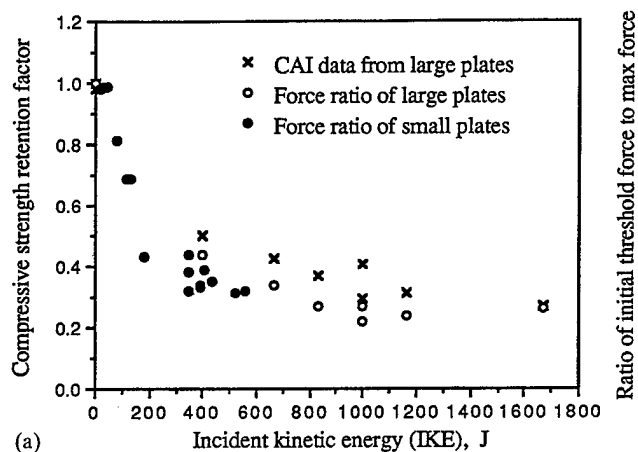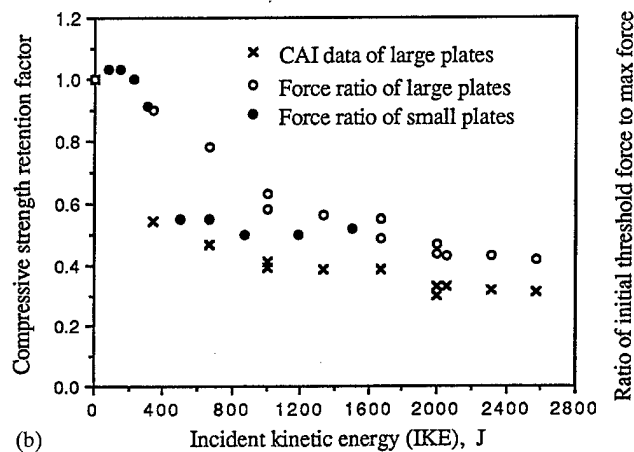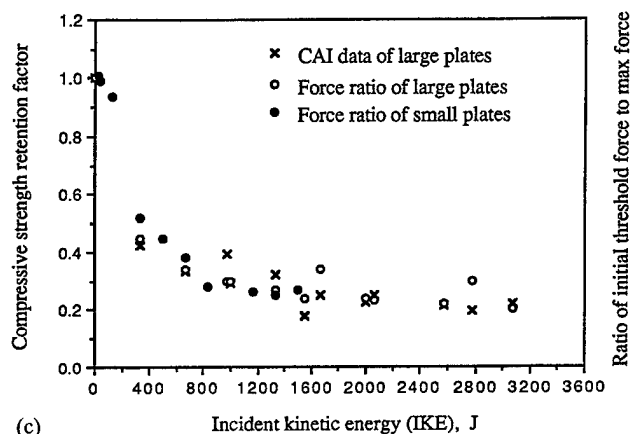

Fig. 4. Impact force–time history curve for small E-glass/polyester laminate plate (thickness 10 mm; diameter 100 mm).

Fig. 5. Delamination area as a function of impact force for small E-glass/polyester laminate plates.
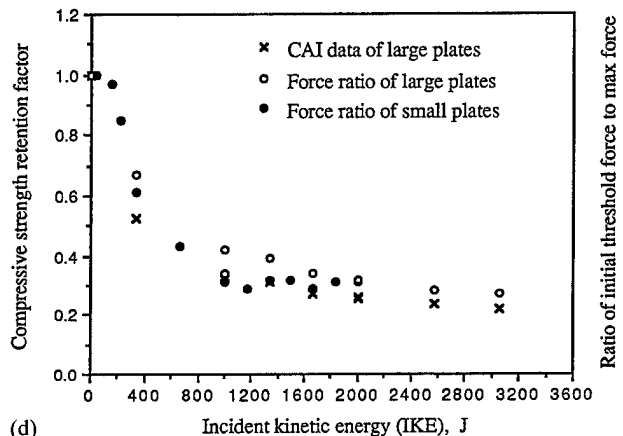
Fig. 6. Comparison of strength retention factor with force ratio in terms of IKE for E-glass/polyester laminate plates of thickness 10 mm (a) and 25 mm (b), and S-glass/phenolic plates of thickness 14 mm (c) and 19 mm (d).

impact response becomes very complex as it is altered by the initiation and subsequent development of damage, as seen in Fig. 4. Many techniques of have been developed to detect, display and quantify impact damage. They include both non-destructive and destructive methods such as ultrasonic scanning (C-scan), X-ray radiography, thermal deplying and cross-sectioning [3–5]. A distinctive advantage of non-destructive over destructive techniques is that impacted specimens could be used for the testing of residual properties after damage examination. In the present investigation, all the impacted specimens were C-scanned and a few selected specimens were cross-sectioned.

An ultrasonic C-scan is so far the most powerful non-destructive tool for detecting and quantifying impact damage, mainly delamination. With through-transmission mode, this technique provides a projected contour of the damage area. Although through-the-thickness distribution of damage in thick laminates is important, particularly in terms of impact energy absorption, the size of the largest delamination is still most critical in assessing residual compressive strength. The use of this technique for thick woven roving fabric
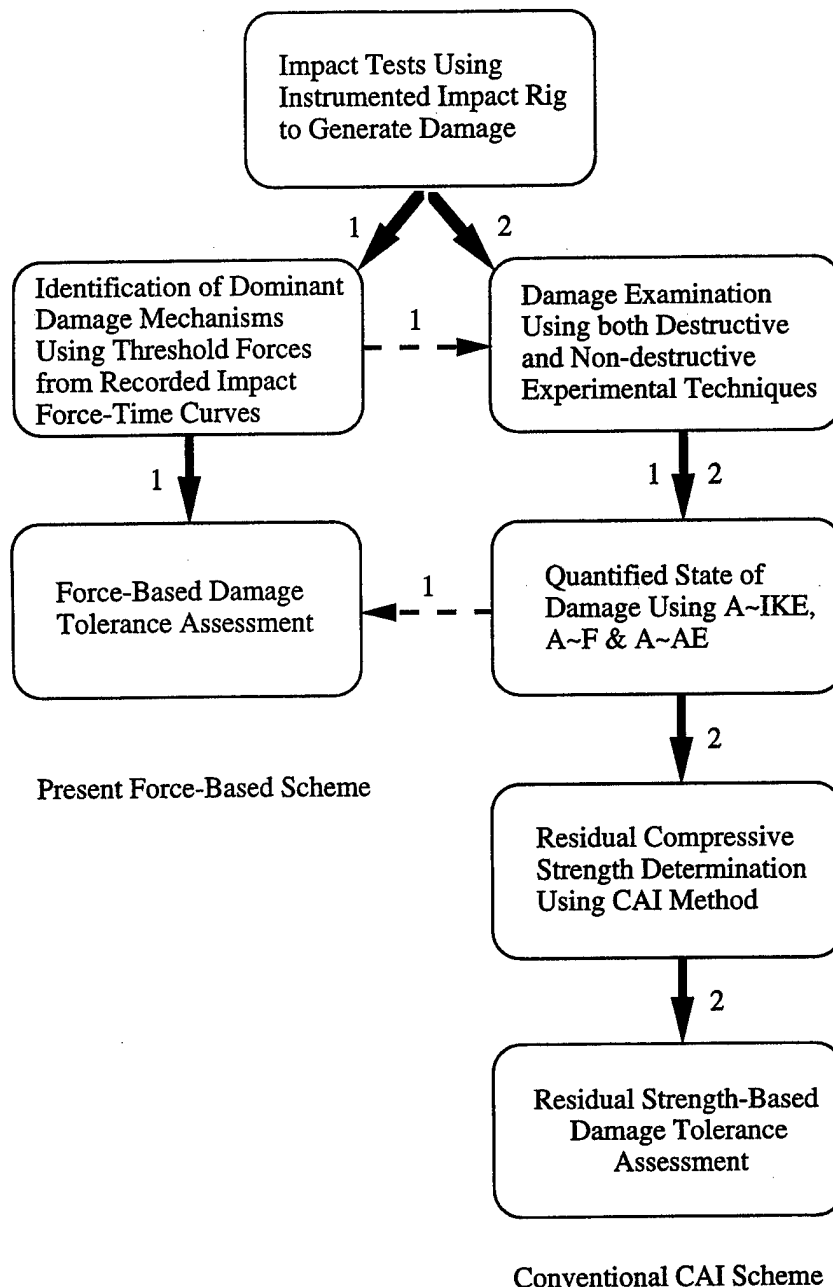
Fig. 7. Conventional and proposed schemes for assessing impact damage resistance and damage tolerance.

composites presents quite a challenge because fibre waviness caused by fibre crossovers, compounded by impact damage, results in a considerable loss of acoustic energy. A widely used destructive technique is cross-sectioning in conjunction with an optical microscope. The impacted specimen is usually cut across the impact contact area with the cross-section on one of the parts being polished for microscopic examination. This technique is useful for qualitative confirmation of the nature, extent and through-the-thickness distribution of damage. Using the above techniques along with visible observation, matrix cracking, surface ply microbuckling, delamination and fibre shear-out were found in impacted specimens with the latter two being dominant.

Matrix cracking is usually of a tensile nature and is generally localised in the impact contact area and its immediate vicinity and extends to the distal surface. For polyester and phenolic matrices with light colours, discolouring on their surfaces makes matrix cracking easily identifiable. For these thick laminates, its effect on impact response is found, after extensive diagnostic testing, to be negligible before delamination occurs. Fibre shear-out in the present impacted composite plate provides a measure of the load-bearing capability of the structure, so its effect on the impact response is clearly marked with a sharp drop-off on the impact force–time history curve, as shown in Fig. 4.

Delamination usually associated with some matrix cracking describes the planar separation of plies or fibre–matrix interface within a laminate, generated in a complex state of stress, as stiffness mismatch between fibres and surrounding matrix is maximum at the fibre–matrix interface. It is not only material damage but also structural damage. As the delaminated region separates the laminate into two parts (assuming a single delamination), the flexural rigidity of the delaminated plate suffers a significant reduction. Because it is invisible from either side of the laminate and is responsible for a significant reduction of compressive strength, delamination has been at the centre of extensive investigation. The cause of delamination in composite structure during impact is complex involving, among others, composite systems, geometry and stress components, so that a fair amount of confusion of both conceptual and interpretative nature exists. Two points are particularly worth mentioning. First, although delamination occurs between two plies of different fibre orientation, the implication that a unidirectional (UD) laminate suffers less or no delamination is questionable as UD beams fail in the same manner as beams of other layups. Second, two "types" of delamination seem to exist and should be distinguished. One is defined as material delamination and has a relatively large population distributed in the volume of a frustum-shaped region through the thickness with an average size comparable to ply thickness and is often linked to matrix tensile cracks or fibre–matrix debonds. For this type of delamination, the interlaminar shear (ILS) stress does not seem to play a dominant role. The published results as reviewed in [3,5] and in [10,11] from UD prepreg-based composite systems show that an associated overall delamination area is due to the overlapping of multiple "peanut-shaped" delaminations at different interfaces and with similar sizes developed along the respective local fibre directions. The other, called structural delamination, of relatively few has a size of several laminate thicknesses spreading usually way outside the frustum-shaped region and occurs around the midplane of the laminate. The generation of structural delamination not only is dominated by ILS stress which reaches the maximum at the midplane and releases a large amount of elastic strain energy but also still carries a danger of further propagation in subsequent static compression. It is this structural delamination which is particularly detrimental to the stability of delaminated composite structures in compression. Most efforts for quantifying impact damage have been focused on delamination using an ultrasonic C-scan so that the delamination area has been employed to describe its extent.

3. Damage measures in impact damage resistance and damage tolerance assessment

Impact damage resistance (IDR) generally defines a range of measures describing not only the maximum load a composite structure can sustain without suffering appreciable damage but also the ultimate load at which the load-bearing capability of a composite structure is reached. In essence, it describes a relation between impact condition and state of damage. Therefore, with the progressive nature of damage as discussed above, IDR for the present laminates should comprise two separate elements, namely, resistance to the onset of delamination and its subsequent propagation and resistance to fibre shear-out. Although with this description a choice for damage measure could be made between IKE and absorbed energy (AE), impact force is obviously most convenient as has also been shown in [12–14]. It is not only capable of identifying the initiation of dominant damage mechanisms as demonstrated in Fig. 4 but is also related to the growth of the delamination area as shown in Fig. 5. Its additional advantages are that it allows direct comparison between impact and static forces for examining loading rate effect and examination of local and global responses for stress and energy absorption analyses. The use of IKE or AE, on the contrary, does not allow an examination of relative

individual contributions of impact velocity and impactor mass.

Impact damage tolerance, on the contrary, assesses the ability of damaged composite structures to retain residual compressive strength in terms of a damage measure which is ideally the same as that used in IDR. The determination of residual compressive strength is, however, not an easy task due mainly to three factors [15]. First, different anti-buckling support strategies have been used so that whatever residual strength one obtains is likely to be support-specific. Second, local impact damage in the contact area is usually accompanied by a varying amount of change in fibre curvature which could act as a misalignment introduced in the compression test. Finally, there exist multiple failure mechanisms such as kink-band shear, delamination opening and global buckling, partly associated with loading types and composite systems. Unlike in IDR, two damage measures such as delamination area and surface indent have been used for damage tolerance assessment in addition to IKE and impact force [16–18]. The use of IKE preferred by industry could result in different delamination areas associated with different combinations of large mass/low velocity and small mass/high velocity as mentioned previously. This perhaps partially explains the need to use the area of structural delamination. The use of a circular delamination area seems to be adequate provided that delamination per se and its propagation determines residual compressive strength. Otherwise, an irregular shape of delamination area deviating significantly away from a circle may yield different residual compressive strengths when tested in different directions. The use of surface indent is for the convenience of inspection engineers as surface indent has not been proved to bear any substantial relation to either IKE or delamination area. Recently, AE has been suggested [19] as a more relevant damage measure, as the more energy the impacted structure absorbs, the lower the residual compressive strength should be. However, the use of AE may involve a lot more data reduction and interpretation.

Against this background, the use of impact forces not only for IDR but also as an alternative to residual compressive strength is proposed here for assessing directly damage tolerance provided that delamination is of an ILS stress-driven structural nature and is responsible, along with local impact damage, for a reduction of compressive strength. The idea is to use the ratio of a threshold impact force corresponding to the onset of delamination to a maximum impact force in a group of tests plotted against impact force or IKE as shown in Fig. 6(a–d) with the data of residual compressive strengths included for direct comparison. It can be seen from these figures that their correlations with respective strength retention factors are good for 10-mm-thick E-glass/polyester and 14- and 19-mm-thick S-glass/phenolic plates, although, for the former, a slight underestimation is visible at relatively low IKEs. For 25-mm-thick E-glass/polyester plates, an overestimation of about 30–40% seems to be consistent over the whole energy spectrum. This discrepancy is believed to be due to the contribution of non-trivial localised matrix cracking which cannot be accounted for in the present technique. Nevertheless, this alternative is independent of plate geometry and has significant practical implications such that damage tolerance could be assessed by using not only the characteristics of impact response curves without resort to expensive CAI tests but also the impact response characteristics of small plates. This could lead to considerable savings of both time and experimentation cost as illustrated schematically in Fig. 7, although further verification on different laminate systems is necessary.

Although the present method for assessing the effect of damage on impact response and subsequent structural behaviour is quite general, it has an inherent limitation. This technique does not apply to any laminate systems whose initial damage induced by impact loading also leads to final failure. Obviously, for such laminate systems, the assessment of damage tolerance is irrelevant anyway.

4. Concluding remarks

An experimental system including an instrumented drop-weight impact rig, ultrasonic C-scan and CAI test rig is generally essential to the quantitative investigation of impact damage resistance and damage tolerance assessment. An experimentally-determined impact force is a well-proven damage measure for impact resistance. More importantly, it is demonstrated that the ratio of threshold impact forces is a useful alternative to residual compressive strength used for damage tolerance assessment. This provides a rapid and inexpensive technique without resort to complex and expensive CAI tests.

References

[1] Sierakowski R. Towards a damage tolerance philosophy for composite materials. Proc 9th ICCM 1993;6:15–21.

[2] Cantwell WJ, Morton J. The impact resistance of composite materials — a review. Composites 1991;22(5):347–362.

[3] Abrate S. Impact on laminated composite materials. Applied Mechanics Review 1991;44(4):155–190.

[4] Zhou G. Low-velocity impact mechanics and damage in laminated composite structures — a critical review. In preparation.

[5] Hull D, Shi YB. Damage mechanism characterization in composite damage tolerance investigations. Composite Structures 1993;23:99–120.

[6] Zhou G, Davies GAO. Impact response of thick glass fibre reinforced polyester laminates. Int J Impact Engineering 1995;16(3):357–374.

[7] Zhou G. Damage mechanisms in composite laminates impacted by a flat-ended impactor. Composites Science and Technology 1995;54(3):267–273.

[8] Zhou G. Prediction of impact damage thresholds in glass fibre reinforced laminates. Composite Structures 1995;31:185–193.

[9] Cains PJ. Digital filtering of impact data. ASTM STP 1987;936: 81–102.

[10] Lesser AJ, Filippov AG. Mechanisms governing the damage resistance of laminated composites subjected to low-velocity impacts. International Journal of Damage Mechanics 1994;3: 408–432.

[11] Davies GAO, Zhang X. Impact damage prediction in carbon composite structures. International Journal of Impact Engineering 1995;16(1):149–170.

[12] Sjoblom P. Simple design approach against low-velocity impact damage. In: Proceedings of the 32nd International SAMPE Symposium. 1987:529–539.

[13] Lagace PA, Williamson JE, Tsang PHW, Wolf E, Thomas S. The use of force as a (impact) damage resistance parameter. In: Proceedings of the 7th Technical Conference for Composites. Pennsylvania State University, 1992:991–1000.

[14] Jackson WC, Poe CC Jr. The use of impact force as a scale parameter for the impact response of composite laminates. Journal of Composites Technology and Research 1993;15(4): 282–289.

[15] Zhou G. Compressive behaviour of large undamaged and damaged thick laminated panels. Composite Structures 1997;38(1–4):589–597.

[16] Zhou G, Davies GAO. Damage tolerance of thick glass fibre reinforced laminate structures subjected to low-velocity impact. Proc ASME-WAM 1994;MD-51:237–262.

[17] Zhou G. Effect of impact damage on residual compressive strength of GFRP laminates. Composite Structures 1996;35(2): 171–181.

[18] Davies GAO, Hitchings D, Zhou G. Impact damage and residual strengths of woven fabric glass/polyester laminates. Composites (Part A) 1996;27(12):1147–1156.

[19] Pintado P, Vogler TJ, Morton J. Impact damage tolerance of thick graphite–epoxy composite systems. Proc ICCM-8 1991;30-F:1–12.

THIRD INTERNATIONAL CONFERENCE ON COMPOSITE SCIENCE AND TECHNOLOGY

11-13 January 2000, Durban, South Africa

Simultaneously with ICCST/3, SACAM 2000: International Conference on Applied Mechanics will be held at The Holiday Inn, Durban, South Africa.

INTRODUCTION
Following the highly successfully ICCST/1 and ICCST/2 held in Durban in 1996 and 1998, ICCST/3 will be held at a beachfront hotel in Durban from 11 to 13 January 2000. Prospective authors are invited to submit abstracts on all aspects of composites in accordance with the deadlines given below.

The conference will cover a wide range of subjects within the basic themes of:
Materials   *   Structures   *   Manufacturing   *   Computer Simulation   *   Modelling   *   Testing

CALL FOR PAPERS
Prospective authors should submit a 300-word abstract to the conference organisers preferably by e-mail. Abstracts can also be submitted by fax or by post. Abstracts should clearly state the objectives, results and conclusions of the work undertaken and emphasise the novel aspects of the work. It should contain the mailing address, fax number and e-mail of the corresponding author. All abstracts will be reviewed by an international technical committee.

CONFERENCE PROCEEDINGS
Papers presented will be published in the conference proceedings which will be available at the Conference. For this purpose a six-page camera-ready manuscript of the paper should be submitted to the organisers. A number of selected papers will appear in a special issue of *Composite Structures* (edited by I H Marshall).

IMPORTANT DATES
Deadline for Abstracts: 31 May 1999
Notification of acceptance: 31 June 1999
Submission of six-page camera-ready manuscripts: 15 October 1999

CONFERENCE ORGANISERS
S Adali, E Morozov and V E Verijenko - University of Natal, South Africa

SACAM 2000: INTERNATIONAL CONFERENCE ON APPLIED MECHANICS
ICCST/3 attendees have a unique opportunity to participate in and submit papers to *SACAM 2000: International Conference on Applied Mechanics* that will be running at the same time and venue as ICCST/3.

REGISTRATION FEE: $320 (Post-graduate students: $140).
The fee covers the Conference Proceedings of ICCST/3, welcome reception and the conference banquet. The registration also entitles the delegates to present papers at SACAM 2000 and attend the keynote lectures and sessions of SACAM 2000.

CORRESPONDENCE ADDRESS
·Professor S Adali/Professor E Morozov/Professor V E Verijenko, Department of Mechanical Engineering, University of Natal, Durban 4041, South Africa
Telephone: +27 31 260 3203 (SA)/+27 31 260 3200 (EM)/+27 31 260 1063 (VEV)
Fax: +27 31 260 3217
E-mail: adali@eng.und.ac.za/morozov@eng.und.ac.za/verijenk@eng.und.ac.za
Website: http://www.und.ac.za/und/mech/conference.html

Composite Structures — Instructions to Authors

Submission of Papers

Authors are requested to submit their original manuscript and figures with three copies to the Editor: Prof. I. H. Marshall, 36 Gogoside Road, Largs, Ayrshire, Scotland KA30 9LX, UK or to any member of the Editorial Board.

All papers should be written in English and will be independently refereed.

Submission of a paper implies that it has not been published previously, that it is not under consideration for publication elsewhere, and that if accepted it will not be published elsewhere in the same form, in English or in any other language, without the written consent of the publisher. All papers should be written in English. All papers will be independently refereed.

Types of Contributions

Research papers; review articles; case studies; technical notes; book reviews; reports of conferences and meetings; letters to the Editor.

Manuscript Preparation

General: Manuscripts must be typewritten, double-spaced with wide margins on one side of white paper. Good quality printouts with a font size of 12 or 10 pt are required. The corresponding author should be identified (include a Fax number and E-mail address). Full postal addresses must be given for all co-authors. Authors should consult a recent issue of the journal for style if possible. An electronic copy of the paper should accompany the final version. The Editors reserve the right to adjust style to certain standards of uniformity. Authors should retain a copy of their manuscript since we cannot accept responsibility for damage or loss of papers. Original manuscripts are discarded one month after publication unless the Publisher is asked to return original material after use.

Paper Length: Generally, the size of the manuscript should not exceed 6000 words or about 12 printed pages.

Abstracts: The Abstract should be of about 100–150 words, reporting concisely on the purpose and results of the paper.

Text: Follow this order when typing manuscripts: Title, Authors, Affiliations, Abstract, Keywords, Main text, Acknowledgements, Appendix, References, Vitae, Figure Captions and then Tables. Do not import the Figures or Tables into your text. The corresponding author should be identified with an asterisk and footnote. All other footnotes (except for table footnotes) should be identified with superscript Arabic numbers.

Symbols: The SI system should be used for all scientific and laboratory data; if, in certain instances, it is necessary to quote other units, these should be added in parentheses. Temperatures should be given in degrees Celsius. The unit billion' (10^9 in America, 10^{12} in Europe) is ambiguous and should not be used.

References: All publications cited in the text should be presented in a list of references following the text of the manuscript. In the text refer to references by a number in square brackets on the line (e.g. Since Sonti[1]), and the full reference should be given in a numerical list at the end of the paper.
References should be given in the following form:
1. Sonti SS, Davalos JF, Zipfel MG, Gang Rao HVS. A review of wood cross tie performance. Forest Products Journal 1995;45(9):55–58.
2. Hetenyi M. Beams on elastic foundation. Ann Arbor, MI: University of Michigan Press, 1946.
3. Adali S. Lay-up optimization of laminated plates under buckling loads. In: Turvey GJ, Marshall IH, editors. Buckling and postbuckling of composite plates. London: Chapman and Hall, 1995. p. 329–365.
4. Adali S, Verijenko VE, Galileev SM, Matrosov AV. Method of initial function in three-dimensional analysis of laminated composite structures. In: Composites Modelling and Processing Science, Proceedings of the 9th International Conference on Composite Materials (ICCM/9), Madrid, 12–16 July 1993. p. 23–30.

Illustrations: All illustrations should be provided in camera-ready form, suitable for reproduction (which may include reduction) without retouching. Photographs, charts and diagrams are all to be referred to as 'Figure(s)' and should be numbered consecutively in the order to which they are referred. They should accompany the manuscript, but should not be included within the text. All illustrations should be clearly marked on the back with the figure number and the author's name. All figures are to have a caption. Captions should be supplied on a separate sheet.
Line drawings: Good quality printouts on white paper produced in black ink are required. All lettering, graph lines and points on graphs should be sufficiently large and bold to permit reproduction when the diagram has been reduced to a size suitable for inclusion in the journal. Dye-line prints or photocopies are not suitable for reproduction. Do not use any type of shading on computer-generated illustrations.
Photographs: Original photographs must be supplied as they are to be reproduced (e.g. black and white or colour). If necessary, a scale should be marked on the photograph. Please note that photocopies of photographs are not acceptable.
Colour: Where colour figures are required, the author will be charged accordingly. Further details of cost are available from Author Services, at Elsevier Science.

Tables: Tables should be numbered consecutively and given a suitable caption and each table typed on a separate sheet. Footnotes to tables should be typed below the table and should be referred to by superscript lowercase letters. No vertical rules should be used. Tables should not duplicate results presented elsewhere in the manuscript, (e.g. in graphs).

Electronic Submission

Authors should submit an electronic copy of their paper with the final version of the manuscript. The electronic copy should match the hardcopy exactly. Always keep a backup copy of the electronic file for reference and safety. Full details of electronic submission and formats can be obtained from Author Services at Elsevier Science.

Proofs

Proofs will be sent to the author (first named author if no corresponding author is identified of multi-authored papers) and should be returned within 48 hours of receipt. Corrections should be restricted to typesetting errors; any others may be charged to the author. Any queries should be answered in full. Please note that authors are urged to check their proofs carefully before return, since the inclusion of late corrections cannot be guaranteed. Proofs are to be returned to the Log-in Department, Elsevier Science, The Boulevard, Landford Lane, Kidlington, Oxford OX5 1GB, UK.

Offprints

Twenty-five offprints will be supplied free of charge. Additional offprints and copies of the issue can be ordered at a specially reduced rate using the order form sent to the corresponding author after the manuscript has been accepted. Orders for reprints will incur a 50% surcharge.

Copyright

All authors must sign the 'Transfer of Copyright' agreement before the article can be published. This transfer agreement enables Elsevier Science Ltd to protect the copyrighted material for the authors, but does not relinquish the author's proprietary rights. The copyright transfer covers the exclusive rights to reproduce and distribute the article, including reprints, photographic reproductions, microfilm or any other reproductions of similar nature and translations. Includes the right to adapt the article for use in conjunction with computer systems and programs, including reproduction or publication in machine-readable form and incorporation in retrieval systems. Authors are responsible for obtaining from the copyright holder permission to reproduce any figures for which copyright exists.

Author Services

For queries relating to the general submission of manuscripts (including electronic text and artwork) and the status of accepted manuscripts, please contact Author Services, Log-in Department, Elsevier Science, The Boulevard, Langford Lane, Kidlington, Oxford OX5 1GB, UK. E-mail: *authors@elsevier.co.uk*, Fax: +44 (0) 1865 843905, Tel: +44 (0) 1865 843900.

CONTENTS

Volume 42 Number 4 1998

Special Issue: International Workshop on Experimental Techniques in the Analysis of Composite Structures